Abstract

Microwave resonators fabricated from superconducting thin films are playing a critical role with recent advances in superconducting quantum computing technology and photon detectors. There has been an intensive worldwide effort to study the sources of loss that limit the quality factors of these resonators. In this thesis, I have focused on the measurements of the microwave response of vortices in Al and Re superconducting thin film resonators cooled in magnetic fields comparable to or less than that of the Earth. Previous work on vortex dynamics at microwave frequencies has involved large magnetic fields, orders of magnitude larger than the Earth's field. Al and Re are common materials used in superconducting resonant circuits for qubits and detectors. Despite the similarities of Al and Re superconductors, the microwave vortex response is strikingly different in the two materials from my resonator measurements. I present a quantitative model for the dissipation and reactance contributed by the vortices in terms of the elastic pinning forces and the viscous damping from the vortex cores. The differences in the vortex response in Al and Re were due to the vortex pinning strength in the two films.

The critical role played by pinning in determining the microwave response motivated us to try to modify the pinning in our Al films by nanostructuring the film surface. A single narrow slot along the centerline of a resonator was used to increase the pinning in the resonator traces and resulted in a reduction of the loss from vortices by over an order of magnitude. Such patterned pinning techniques could be used on resonators in systems with insufficient shielding or pulsed control fields to reduce the loss from unwanted trapped vortices.

Finally, we explored the possibility for using measurements of the power dependence of the resonators to determine if trapped vortices are present.

Microwave Properties of Vortices in Superconducting Resonators

BY

Chunhua Song

B.S. Nanjing University Nanjing, 1999

M.S. Nanjing University Nanjing, 2004

DISSERTATION

Submitted in partial fulfillment of the requirements for the

degree of Doctor of Philosophy in Physics

in the Graduate School of Syracuse University

December 2011

UMI Number: 3495121

UMI®

Dissertation Publishing

ProQuest®

Contents

List of Figures

List of Tables

Acknowledgments

Chapter 1

Introduction

Superconductors can be used to make resonant circuits with high quality factors. Such superconducting microwave thin film resonators have shown significant promise in the field of quantum computing [1], and therefore, have drawn a lot of attention. In many recent low-temperature experiments, such resonators have been coupled to quantum coherent superconducting devices, or qubits [1], for explorations of quantum electro-dynamics (QED) with circuits [2, 3]. Furthermore, high-quality factor resonators have enabled the development of Microwave Kinetic Inductance Detectors, highly sensitive photon detectors for astrophysical measurements [4, 5]. The superconducting mi-crowave thin film resonators also has applications in the multiplexed readout of single electron transistors (SET) [6], normal metal-insulator-superconductor (NIS) tunnel junction detectors [7] and superconducting quantum interference devices (SQUID) [8]. Recently, superconducting resonators have been used to host arbitrary photon states generated by coupling to qubits [3, 9, 10].

The performance of a superconducting resonator is typically characterized by the quality factor. The resonator quality factor can be influenced by multiple sources of loss, such as the coupling to external circuitry, dielectric loss in the substrate, surface loss in native oxides, and nonequilibrium quasiparticles [11–15]. In order to improve the performance of superconducting resonators, there have been many recent efforts to

study these various loss mechanisms and develop improved superconducting materials and circuit designs. Another potential source of loss in thin-film superconducting resonators is loss due to vortices trapped in the superconducting traces, which can result in substantial reductions in the quality factor of SC superconducting resonators. The presence of even a few vortices can substantially reduce the resonator quality factor [16]. Thus, understanding this dissipation mechanism is important for the design of microwave superconducting circuits.

The microwave dynamics of vortices in superconductors has caused a lot of interest. Gittleman and Rosenblum [17, 18] gave the first treatment of the high-frequency response of vortices in terms of the viscous damping from the vortex motion and the elastic response of the vortex interactions with pinning defects in the superconductor. Similar measurements were also performed on Al thin films in Ref. [19]. Several decades later, various groups studied vortices at microwave frequencies in YBCO films, with particular relevance to high-T_c thin-film microwave devices [20–23]. Recently there have also been investigations of microwave vortex dynamics in MgB_2 [24–26] and Nb films [27]. Previous work on the microwave response of vortices in superconductors has primarily involved large magnetic fields, at least several orders of magnitude larger than the Earth's field. On the other hand, superconducting resonant circuits for qubits and detectors are typically operated in relatively small magnetic fields, of the order of 100 μT or less and are fabricated from low-T_c thin films that are often type-I superconductors in the bulk.

In this thesis, I will present measurements of the microwave response of vortices in Al and Re superconducting thin film resonators [16]. Al and Re are common materials used in superconducting resonant circuits for qubits and detectors. Despite the similarities of Al and Re superconductors, the microwave vortex response is strikingly different in the two materials from our resonator measurements. Related measurements that motivated my work were performed in Ref. [28]. The differences in the vortex response in Al and Re were due to the vortex pinning strength in the

two films [16]. This motivated us to try to modify the pinning in our Al films by nanostructuring the film surface. A single narrow slot along the centerline of an Al coplanar waveguide resonator is used to increase the pinning in the resonator traces and reduce the loss from vortices by over an order of magnitude. Finally, I will explore the possibility for using measurements of the power dependence of the resonators to determine if trapped vortices are present.

This thesis is organized as follows: Chapter 2 first introduces some basic properties of superconductors, such as the Meissner effect, and characteristic parameters, such as the mean free path l, coherence length ξ, and penetration depth λ. I discuss the relevant concepts for describing vortex dynamics, including the flux-flow resistivity, Lorentz force on vortices and how to introduce vortices into a superconductor. At the end, there is a brief survey that describes the previous work on vortices at microwave frequencies.

Chapter 3 introduces basic concepts of microwave circuit design and measurement. I present several types of transmission lines and the basic concept of a network analyzer, S matrix, to help understanding a microwave circuit. I discuss the design of distributed microwave resonators from transmission lines and compare them with lumped element circuits. This chapter also contains a brief survey of loss mechanisms in superconducting resonators.

Chapter 4 is a detailed description of our experimental setup, resonator design and fabrication. I discuss a variety of measurement techniques, such as the approach for cooling a resonator in a magnetic field and probing the temperature and power dependence of superconducting resonator to investigate the microwave response of our superconducting thin film resonators. I explain the reasons to choose a layout of several multiplexed quarter wavelength resonators by capacitive-coupling to a common feedline, then I list our design parameters, such as the resonator center frequency f_0, coupling quality factor Q_c. Numerical simulations with the microwave modeling package SONNET were used in the resonator design process. Lithography, etching,

dicing and packaging are described in detail in this chapter. In addition, a fitting routine to analyze our resonator data is presented.

Chapter 5 is about the characterizatoin of superconducting parameters from resonator measurements. The value of residual resistivity ratio (RRR) and T_c of the superconducting material can be used to evaluate the quality of the superconducting film. Techniques for measuring RRR and T_c is described in this chapter. I present measurements of the temperature dependence for Al quarter wavelength CPW resonators. The Mattis-Bardeen theory of the complex ac conductivity of a superconductor is introduced to fit our temperature dependence data, thus allowing us to extract the kinetic inductance fraction for the resonators.

Chapter 6 contains measurements of the microwave response of the Al and Re resonators due to a small number of vortices. I describe field-cooled measurements for trapping vortices in Al and Re resonators and a model for fitting the microwave response of the vortices. In addition, I discuss the threshold cooling fields for trapping vortices by taking measurements on different width resonators. Finally, vortex distribution in the resonator trance is presented.

In chapter 7, a technique is demonstrated to reduce the loss due to vortices. Sometimes background fields or pulsed control fields are present in experiments with superconducting resonators. Thus, the ability to reduce the loss from trapped vortices would be helpful. A narrow slot etched into the resonator surface provides a straightforward method for pinning enhancement without otherwise affecting the resonator. Resonators patterned with such a slot exhibited over an order of magnitude reduction in the excess loss due to vortices compared with identical resonators from the same film with no slot.

Chapter 8 is a summary of some ongoing and future projects related to vortices in microwave resonators. This chapter shows that there is a dramatic difference in the power dependence of the resonator depending on the presence of trapped vortices which provides a criteria to distinguish whether or not a resonator has trapped

vortices. We are studying the width dependence of the threshold field for trapping vortices.

Chapter 2

Superconductors and vortices

2.1 Introduction to superconductivity

2.1.1 Basic properties

Superconductors are amazing materials whose resistance drops to zero when cooled below its critical temperature. The following sections introduce some basic properties of superconductors, such as the Meissner effect and characteristic parameters. The relevant concepts for describing vortex dynamics, including the flux-flow resistivity, Lorentz force on vortices and how to introduce vortices into a superconductor are presented. At the end, there is a brief survey that describes the previous work on vortices at microwave frequencies.

2.1.1.1 Zero electrical dc resistance

In 1911, superconductivity was first observed in mercury by Dutch physicist Heike Kamerlingh Onnes at Leiden University. When the mercury was cooled below $4.1\,\mathrm{K}$, the resistance abruptly disappeared [29]. Other metals that exhibited zero resistivity below a certain temperature were also encountered. This phenomenon of the metal losing electric resistance was named superconductivity.
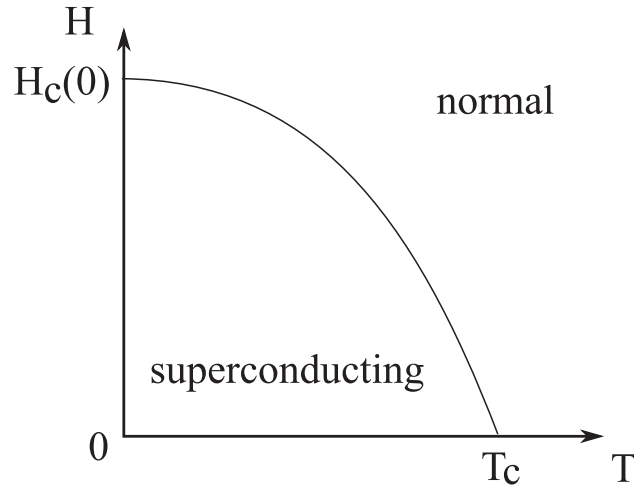
Figure 2.1: Critical magnetic field as a function of temperature (type I superconductors).

2.1.1.2   Meissner effect

The next remarkable phenomenon found in superconductivity occurred in 1933. German researchers Walther Meissner and Robert Ochsenfed discovered that superconductors expel magnetic flux from their interior; this has been known as the Meissner Effect [30].

If a non-magnetic normal metal has a uniform magnetic field through it when it is cooled, the magnetic field is expected to stay the same. However, for a superconductor, the field would be screened out from the interior of the material. The superconductor is a perfect diamagnet. The external magnetic field remains unchanged, but because of the diamagnetic response of the superconductor, magnetic flux density is zero inside the superconductor. A phase transition as shown in Figure 2.1 shows there is a critical magnetic field, below which, superconductivity can occur, so the external magnetic flux density is expelled. This critical magnetic field H_c is a function of temperature.

2.1.1.3 London equations and penetration depth

One of the theoretical explanations of the Meissner effect comes from the London equations which were developed by brothers Fritz and Heinz London in 1935 [31]. These equations provide a phenomenological description of superconductivity. The London equations are:

$$\frac{\partial \vec{j_s}}{\partial t} = \frac{n_s e^2}{m} \vec{E} \tag{2.1}$$

$$\nabla \times \vec{j_s} = -\frac{n_s e^2}{m} \vec{B} \tag{2.2}$$

where $\vec{j_s}$ is the superconducting current, $\vec{E}$ and $\vec{B}$ are the electric field and magnetic flux density respectively, e is the charge of an electron, m is the electron's effective mass, and n_s is the density of superconducting charge carriers.

We can use Ampere's law on one of the London equations 2.2, and obtain a second order differential equation whose solution shows that currents decay exponentially in from the surface of the superconductor with a characteristic length scale λ. The London penetration depth is expressed as:

$$\lambda = \sqrt{\frac{m}{\mu_0 n_s e^2}} \tag{2.3}$$

which characterizes one of the length scales. Beyond λ, external magnetic fields are exponentially suppressed, that is to say, the London equation requires that the magnetic flux density decay to zero inside a superconductor beyond penetration depth λ.

2.1.1.4 Ginzburg−Landau (GL) and BCS theory

Around 1950, Landau and Ginzburg derived the phenomenological Ginzburg-Landau theory of superconductivity [32] which can successfully explain the macroscopic properties of superconductors. In 1957, the widely accepted microscopic description of superconductivity was advanced by John Bardeen, Leon Cooper, and Robert Schrieffer [33]. Their well known theory of superconductivity is named BCS theory; it

explains the superconducting current as a superfluid of Cooper pairs. A Cooper pair is two electrons bonded as a pair and interacting through the exchange of phonons. In 1959, Lev Gor'kov showed that microscopic BCS theory can be reduced to the phenomenological Ginzburg-Landau theory near the critical temperature [34].

BCS theory produces an independent characteristic length scale, a coherence length ξ_0. This length is related to the Fermi velocity of the material and the energy gap associated with the condensation to the superconducting state as shown in equation 2.4.

$$\xi_0 = \frac{\hbar v_F}{\pi \Delta_0} \tag{2.4}$$

where v_F is the Fermi velocity, and Δ_0 is the superconducting gap which is the energy required to break up a pair of electrons. For weak-coupling superconductors, this energy gap is $\Delta(0) = 1.76 k_B T_c$ [34] where k_B is Boltzmann's constant. When impure systems are considered, the finite length of the eletron mean free path has to be taken into account. The deceasing value of mean free path results in the drop of the coherence length. A function $\xi(t)$ is given by [35]:

$$\xi(T) = 0.855 \frac{\sqrt{\xi_0 l}}{\sqrt{1-t}} \tag{2.5}$$

with $t = T/T_c$.

2.1.2   Superconductivity in different regimes

For certain regimes of applied magnetic field, the material is constituted by the combination of normal and superconducting domains. In the normal domains, magnetic flux passes through the material, however, the magnetic flux density equals to zero in the superconducting domains. This coexistence state is called 'mixed state' or 'intermediate state'. This domain wall separating a normal from a superconductor wall is associated with energy, and this energy is related to the penetration depth and the coherence length. The ratio of these two characteristic length scales is known as the

Ginzburg$-$Landau parameter (κ),

$$\kappa = \lambda/\xi \tag{2.6}$$

which helps to separate superconductors into two types.

$$\begin{cases} 0 < \kappa < \frac{1}{\sqrt{2}} & \text{type I superconductor} \\ \kappa > \frac{1}{\sqrt{2}} & \text{type II superconductor} \end{cases}$$

When penetration depth is shorter than coherence length, the domain boundary consists of mainly partially superconducting state, and this domain energy is positive. This means that the domain formation is discouraged. In the normal domains, there is a non-quantized amount of magnetic flux and large domain size. Superconductivity in this type can abruptly cease when the applied magnetic field is above a critical value ($H_c(T)$) as we can see from Figure 2.1. Such transition is of first order on a microscopic scale. This is the case of type I superconductors. Most superconducting pure metals are type I superconductors. Among them aluminum and lead are typical examples.

If $\kappa > 1/\sqrt{2}$, it is characterized as type II superconductor which has a gradual transition from superconducting to normal state, in contrast to the sharp change in type I superconductors. In this case, the domain energy is negative, which means the domain formation is preferred. The type-II superconductivity was first theoretically predicted by Alexei Abrikosov [36]. As Figure 2.2 shows, this type of superconductor has two critical magnetic fields (H_{c1} and H_{c2}) which are known as the upper and lower critical field. At fixed temperatures, if the field is above H_{c2}, the metal has normal resistance. When the field is below H_{c2} but still before superconductivity is perfectly formed, the type II superconductor demonstrates a region of 'mixed state' in which some quantized flux named vortex appears. The basic properties of vortices are extensively described later in this chapter. Type-II superconductors are usually made of metal alloys or complex oxide ceramics. Niobium, vanadium, and technetium, however, which are pure elements, are classified as Type-II superconductors.
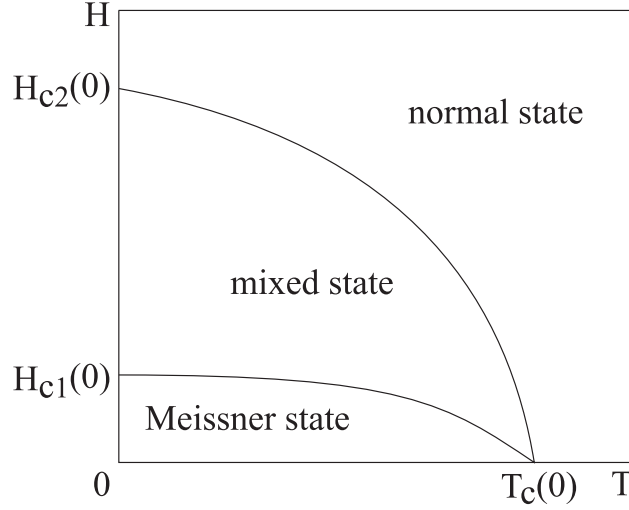
Figure 2.2: Magnetic field-temperature phase diagram for a type II superconductor.

By Comparing Figure 2.2 with Figure 2.1, these two types of superconductors have different shape of the magnetization curve; the magnetization can vanish either by a first order phase transition (type I superconductor), or slowly as a second order transition (type II supercondcutor). The differences between type I and type II superconductors in the microscopic level can be manifested by the different structure of 'intermediate state' and 'mixed state'.

Throughout our research, Al and Re thin film has properties of type II superconductors, despite the fact that Al was just mentioned to be a type I superconductor. In fact, both Re and Al are Type-I superconductors in the bulk; however, films of Type-I superconductors with thicknesses less than the bulk coherence length in perpendicular magnetic fields have been shown to support the nucleation of $h/2e$ Abrikosov vortices [35, 37–40].

Tinkham [37] was the first one to point out that superconducting thin film in perpendicular magnetic field would exhibit a mixed state structure which is similar to the Abrikosov state, even if the ξ was less than $1/\sqrt{2}$. Subsequently, an extensive investigation both theoretically and experimentally of the transition between normal and superconducting state in magnetic field has been made [35, 38–40]. Cody and
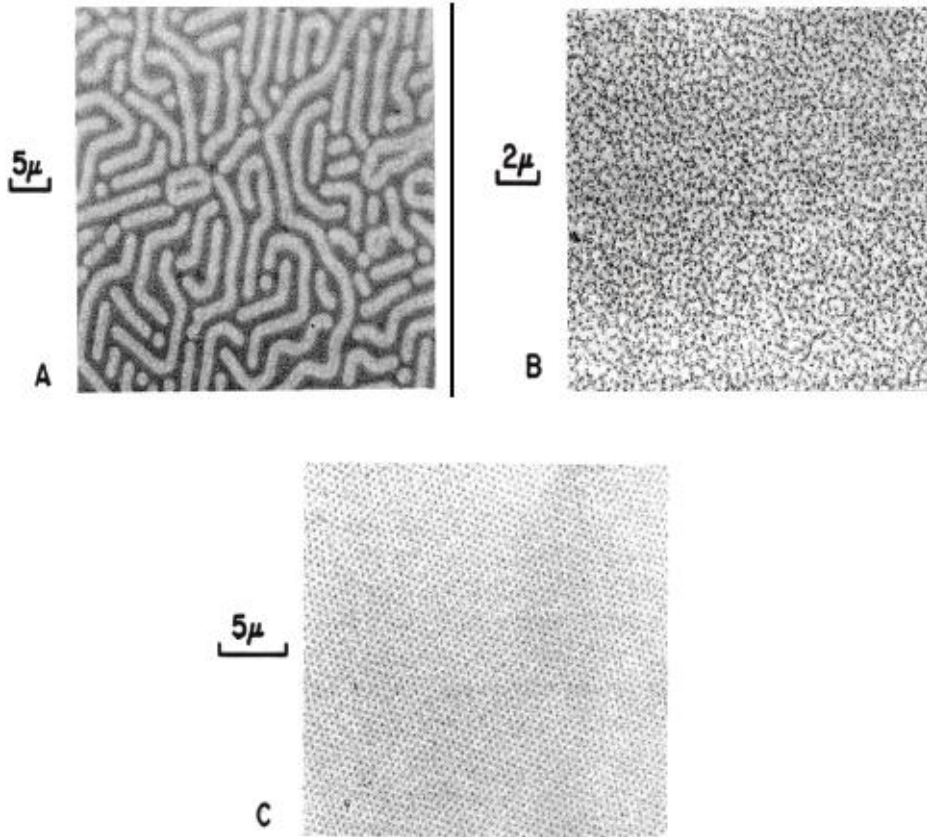
Figure 2.3: Magnetic structures are made visible by decorating the normal regions (dark) with ferromagnetic particles. (a) An intermediate state for a Pb film (b) A single fluxoid vortex mixed state for Pb film with slightly thicker thickness (c) The mixed state in Pb-Tl (5% Tl) alloy crystal. (from G. J. Dolan, 1974, p.133)

Miller [41–43] had a lot of discussions on Pb, Sn and In films and foils of their thickness dependence. Maloney *et al.* also presented the experiment results and analysis of critical field as a function of thickness and temperature on Al films and foils. Their results proved that vortices should exist in sufficiently thin specimens of type I materials. Later, the mixed state for superconducting thin films in magnetic field observed directly by decorating the samples with fine ferromagnetic particles. Using this method, Dolan [40] was able to see the magnetic structure in thin films of Pb, Sn and In with three different thicknesses. Figure 2.3 from Ref. [40] shows the images of magnetic structures at high field. (A) is an intermediate state structure

in a Pb film with the thickness of 770nm. As domain energy is positive in this type I superconductor, they tend to form as few domains as possible. (B) is the image of mixed state for 90nm thick Pb thin film and (C) is a mixed state of bulk Pb-Tl (5%Tl), a type II superconductor. Both Figure (B) and (C) have dense packed single-fluxoid spots; This similarity reflects that thin film of type I superconductor shows the properties of type II superconductor under certain thickness limit. Al and Re thin film in this thesis show the same feature.

2.1.3 Relationships between materials and superconductor parameters

The purity of a superconductor is characterized by the ratio l/ξ_0, in which ξ_0 is the coherence length of the pure material as given in 2.4, and l is the electron mean free path the average distance covered by a moving electron between two successive collisions. l is defined as $l = \tau v_F$ with τ being the time interval between collision determined in the normal state of the superconductor, and v_F being the Fermi velocity. If we apply the free-electron model, we can write:

$$v_F = (\pi k_B/e)^2/\gamma\rho l \tag{2.7}$$

where γ is the linear coefficient of the specific heat. The quantity ρl is the product of the resistivity and mean free path.

$$\begin{cases} l >> \xi_0, \lambda & \text{in clean limit} \\ \lambda << \xi_0 & \text{in dirty limit} \end{cases}$$

As mentioned above, we are in the dirty metal limit if the electronic mean free path l is much shorter than the coherence length ξ_0 and the magnetic penetration depth [44]. In the extreme anomalous limit, the penetration depth is much less than the coherence length. The Al film we work with are certainly in the extreme anomalous limit.
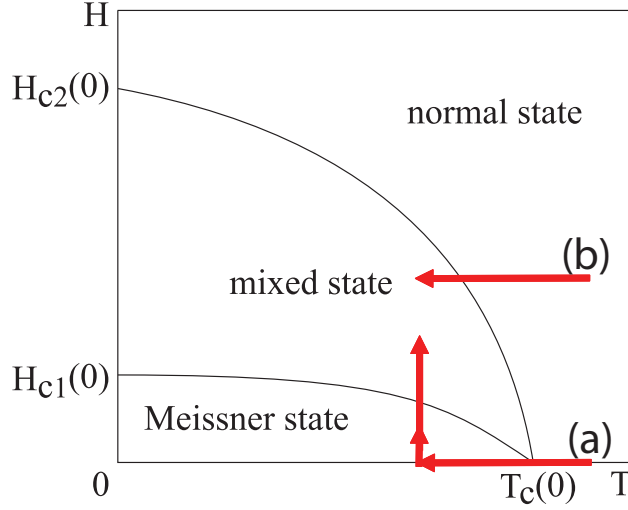
Figure 2.4: Two ways to introduce vortices into superconductors

From Figure 2.1 and 2.2, T_c is a function of the magnetic field, and the slope of the upper critical field can be defined as,

$$S \equiv -\mu_0 \frac{dH_{c2}}{dT}\Big|_{Tc} \tag{2.8}$$

where μ_0 is the magnetic permeability in a vacuum. By applying the BCS expression in Ref. [34], we can obtain the effective coherence length and penetration depth at zero temperature [45]:

$$\lambda(0) = 1.05 \times 10^{-3} \left(\frac{\rho_0}{T_c}\right)^{1/2} \tag{2.9}$$

$$\xi(0) = 1.81 \times 10^{-8} (T_c S)^{-1/2} \tag{2.10}$$

$$\kappa = 3.54 \times 10^4 (\rho S)^{1/2} \tag{2.11}$$

The above expressions are in SI units, so $[S] = T K^{-1}$, $[\rho_0] = \Omega m$ and $[\lambda(0)] = [\xi(0)] = m$

2.1.4 Introducing vortices into a superconductor

There are several ways to introduce vortices. One way is as arrow (a)in Figure 2.4 says, we can cool a superconductor through T_c without any external magnetic field,

which is called zero field cool (ZFC), and then increase the field further after ZFC. In this way, the superconductor experences a Meissner state and then goes to a mixed state where vortices will be driven into the superconductor.

The other procedure we used in this thesis is to cool the superconductor through T_c with a non zero magnetic field. It is called Field Cool (FC). In Figure 2.4, the arrow labeled with (b) indicates the FC process. When the applied field is appropriate, some vortices will be trapped in the superconductor. The details of vortex trapping in the field-cooling of SC strips will be discussed in Chapter 6.

2.2 General properties of vortices

The most important finding from GL theory was made by Alexei Abrikosov in 1957; it is now known as 'vortex physics' [36]. In type II superconductors, there is a vortex state for a certain range of applied magnetic fields. Every vortex has a normal core with a size ξ_0 surrounded by circulating supercurrent. In order to understand vortex dynamics in superconductor, some basic physics of vortices are discussed in the rest of this chapter, and at the end, we introduce two ways in which vortices were generated in our research.

2.2.1 Vortex lattice

As mentioned above, every vortex has a normal core where magnetic field can penetrate through. The magnitude of flux is quantized in unit of,

$$\Phi_0 = \frac{h}{2e} = 2.07 \times 10^{-15} \text{Wb}. \tag{2.12}$$

A group of vortices can form a flux lattice, if there are enough vortices. The vortices in a bulk superconductor experience a repulsive force from neighboring vortices due to the interaction with the circulating current. By this interaction between each vortex, a vortex lattice in a regular triangular shape is formed. This was first observed in

[46]. The lattice constants a_0 can be calculated as equation 2.13.

$$a_0 = \left(\frac{2}{\sqrt{3}}\right)^{1/2} \sqrt{\frac{\Phi_0}{B}}.$$ (2.13)

2.2.2 Lorentz force

When a current density $\vec{J}$ is applied to a type II superconductor in the mixed state, A Lorentz force is produced in the form of:

$$\vec{f_L} = \vec{J} \times \vec{\Phi}_0\, \mathbf{\hat{n}}$$ (2.14)

where $\vec{f_L}$ is the force per unit length of the vortex, and $\vec{\Phi}_0$ is flux quanta in the direction of the external magnetic field. The Lorentz force is perpendicular to the direction of the current and field. If vortex density is high, the Lorentz force density is commonly expressed as:

$$\vec{F} = \vec{J} \times \vec{B}$$ (2.15)

2.2.3 Flux flow

In an ideal type II superconductor where there are no defects, meaning an superconductor in the absence of any confining potential, any nonzero current can lead to a movement because of the Lorentz force. The direction of moving magnetic flux of the vortex is transverse to the applied current but parallel to the Lorentz force. Assuming vortices move at the velocity $\vec{v}$, an electric field will be induced,

$$\vec{E} = \vec{B} \times \vec{v}$$ (2.16)

This induced electric field is in the same direction as the applied current. The suppressed superconductivity in the vortex core leads to dissipation that results in a viscous force that damps the vortex motion.

$$\rho_{ff} = \frac{E}{J}$$ (2.17)

Here ρ_{ff} is the flux flow resistance [47], so the material is no longer in zero resistance region. Kim *etal.* [48] experimentally confirmed the flux flow resistance in type II superconductors. Equation 2.18 shows the vortex equation of the motion without any pinning, which I will discuss right after this section, it means any Lorentz force will lead to a motion of the vortices at constant velocity.

$$\eta\dot{\mathbf{x}} = \mathbf{F}_L, \tag{2.18}$$

This dissipation due to the flux flow can be characterized by the vortex viscosity:

$$\eta = \frac{\Phi_0 B_{c2}}{\rho_n} \tag{2.19}$$

where Φ_0 is the flux quantum, ρ_n is the normal state resistivity and B_{c2} is the upper critical field [34, 47, 49].

2.2.4 Flux creep

Anderson and Kim first described flux creep in Ref. [50, 51]; the basic concept of thermal activation of magnetic flux line out of pinning sites was introduced, and the magnetic relaxation in superconductors was first studied in low temperature superconductors. The idea in Ref. [50] can be simplified as following. A hopping time t for a vortex to hop out of a pinning well is:

$$t = t_0 \exp(U/kT) \tag{2.20}$$

with U to be the potential-energy barrier height and k to be Boltzmann constant [52]. As the hopping is driven by the Lorentz force which is related to the current density J, U should decrease for a larger J. If we assume the energy barrier without Lorentz Force to be U_0, the $U(J)$ can be approximated as [52]:

$$U = U_0 \left(1 - J/J_c\right) \tag{2.21}$$

Combining with equation 2.20 and 2.21, we can get:

$$J = J_c \left(1 - \frac{kT}{U_0} \ln(\frac{t}{t_0})\right) \tag{2.22}$$

which is known as Anderson-Kim equation for flux creep. From this flux creep equation, we can immediately see that magnetization decreases with temperature and logarithmically in time.

2.2.5   Vortex pinning

Any practical superconductor inherently contains various materials defects which produce vortex pinning, thus complicating the situation. Those defects in a superconductor result in regions of weakened superconductivity. The system of superconductor and vortices can lower its energy if the vortices, with cores of suppressed superconductivity, are located at the defects. Thus, the defects result in pinning potential wells. At vortex pinning sites, the flux lines do not move in spite of the Lorentz force in the type II superconductor. Since the force due to the pinning is in the opposite direction of Lorentz force which tends to move flux line, the pinning force [53, 54] along with the Lorentz force can provide a critical current density J_c for vortex motion [55].

In the simplest case, the pinning potential wells $U(x)$ can be assumed to be harmonic with spring constant k_p, giving a pinning force $\vec{F}_p = k_p \vec{x}$. The pinning force is proportional to the amplitude of the displacement of a vortex $\vec{x}$, while the viscous drag force is $\eta \dot{\mathbf{x}}$, with $\dot{\mathbf{x}}$ being the velocity of a vortex. The vortex equation of motion at zero temperature is given by

$$\eta \dot{\mathbf{x}} + k_p \mathbf{x} = \mathbf{F}_L. \tag{2.23}$$

As it was mentioned above, a possible vortex mass can be ignored. Thus, the interplay between the viscous force and the pinning will determine the frequency dependence of the vortex response. The equation 2.23 generates a characteristic depinning frequency,

$$\omega_d = k_p/\eta. \tag{2.24}$$

Thus, at low frequencies the pinning will dominate and the response will be primarily elastic, while at higher frequencies, the viscosity will become more important

and the response will be more dissipative. Gittleman and Rosenblum [18] worked out the analysis which is shown in this section and observed this changeover from a pinned regime without any resistance to a flux flow regime with a ρ_{ff}. In their work, they were making ac measurements of the vortex response as a function of frequency. At high frequency, the effective resistance that GR measured corresponded to the flux-flow value, but the regime was not free flux flow, i.e., the vortices were still simply oscillating about their individual pinning locations.

Pinning occurs at the place where the metal has spatial inhomogeneity such as impurities, grain boundaries, voids, *etc.* All different types of pinning have been studied in all sorts of superconductors. Dam *et al.* [56] also showed that vortices can be pinned at the interfaces between growth islands generated during film deposition.

2.3 Previous work on vortices at microwave frequencies

Vortex dynamics at microwave frequencies has been studied for some time both theoretically [57, 58] and experimentally in a variety of superconductors [16, 18, 20, 23, 24]. The response of vortices to an oscillatory Lorentz force is determined primarily by two forces: the viscous force, due to the motion of the vortex core and characterized by a vortex viscosity η; and the pinning forces in the material that impede the vortex motion and, in the simplest case, can be described by a linear spring constant k_p. The ratio of the pinning strength to the vortex viscosity in Eq. 2.24 determines the crossover frequency separating elastic and viscous response of the vortices.

However, all previous work involved rather large magnetic fields where the vortex density was quite high. As I mentioned in previous sections, Gittleman and Rosenblum [17, 18] did one of the original investigations of the microwave dynamics of vortices in superconductors, they developed a model for the oscillatory motion of the flux tubes in the presence of given pinning centers, and calculated the flux-flow

resistance. Suhl in Ref. [59] calcuated the effective mass of the flux tube which is so small that the term with mass in equation of the motion is probably negligible even at microwave frequencies. By measuring circuits patterned from Pb-In and Nb-Ta alloys foils, the experimental complex conductivity shows a good agreement with the calculated result from equation 2.23 in some simplified special cases.

Similar measurements were also performed on Al thin films in Ref. [19]. The experimental results on their Al thin films also had a reasonable agreement with the GR theory.

In a variety of contexts the microwave response of a superconductor is often characterized in terms of the surface impedance $Z_s = R_s + iX_s$. Changes in Z_s under different conditions, for example, different vortex densities determined by B, can then be separated into changes in the surface resistance $\Delta R_S(B)$ and reactance $\Delta X_S(B)$, where these quantities correspond to the differences between measurements at B and zero field. Several decades later, various groups studied vortices at microwave frequencies in YBCO films, with particular relevance to high-T_c thin-film microwave devices [20–23]. Belk *et al.* characterized the frequency dependence of vortex-induced Z_s over a large frequency span by taking data of the characteristic and the harmonics of a YBCO stripline resonator. They measured both real part R_s and the imaginary part X_s of the microwave complex surface impedance Z_s, partly resulting from vortex motion, at a frequency range from 1.2 to 22GHz and at temperatures from 5 to 65 K in magnetic fields from 0 to 4 T.

There is a simple fact that if there is no external force, such as Lorentz force, vortices are pinned in their potential wells individually. However, with some external force, vortices start to osscilate around the potential minima, at the same time, vortices can move to neighboring minima due to the thermal fluctuation (flux creep). Coffey and Clem [57] solved the basic equations of the model by using the modified Bessel functions of the zeroth (I_0) and first order (I_1), and the resulting complex-

valued effective resistivity can be written as:

$$\widetilde{\rho_v} = \frac{B\Phi_0}{\eta} \frac{\epsilon + (\omega/\omega_c)^2 + i(1-\epsilon)(\omega/\omega_c)}{1 + (\omega/\omega_c)} \tag{2.25}$$

where Φ_0 is the megnetic flux quantum, B is the dc magnetic field , ω_c is the characteristic frequency of a designed circuit, η is the viscous drag coefficient and ϵ is the flux creep factor:

$$\omega_c = \frac{\chi}{\eta} \frac{I_0(\nu)I_1(\nu)}{I_0^2(\nu) - 1}, \tag{2.26}$$

$$\epsilon = \frac{1}{I_0^2(\nu)}, \tag{2.27}$$

where $\nu = U_0/2k_BT$, and U_0 is the barrier height of the periodic potential if we have the assumption that all of the pinning wells have the same depth.

Although the Coffey-Clem theory was developed for high-Tc superconductors, we will see that it is still important to include a flux-creep factor in analyzing our measurements of vortices in Al films at low temperature. In our work, we have used equation 2.25 to fit our measurement data and get the magnitude of depinning frequency and flux creep factor [16].

Recently there have also been investigations of the microwave vortex dynamics in MgB$_2$ [24–26] and Nb films [27]. They have shown that MgB$_2$ behaves like a classical type-II superconductor and, consequently, quite different from the high-T_c cuprates. Zaitsev *et al.* [24] measured MgB$_2$ thin film for the temperature and magnetic field dependence of the surface impedance with the frequency range between 5.7 and 18.5 GHz using a dielectric resonator technique. The experimental results have shown that MgB$_2$ behaves like a BCS superconductor and reveals little analogy with high temperature superconducting cuprates. They have observed that when B is increased, vortex density is increased linearly, correspondingly such as loss from votices has linear increase. Figure 2.5 shows a rapid growth in both real and imaginary of surface impedance which has linear relation with the field. Such behavior is in accordance with the Coffey-Clem [57] and Brandt [58] model. They also observed the same
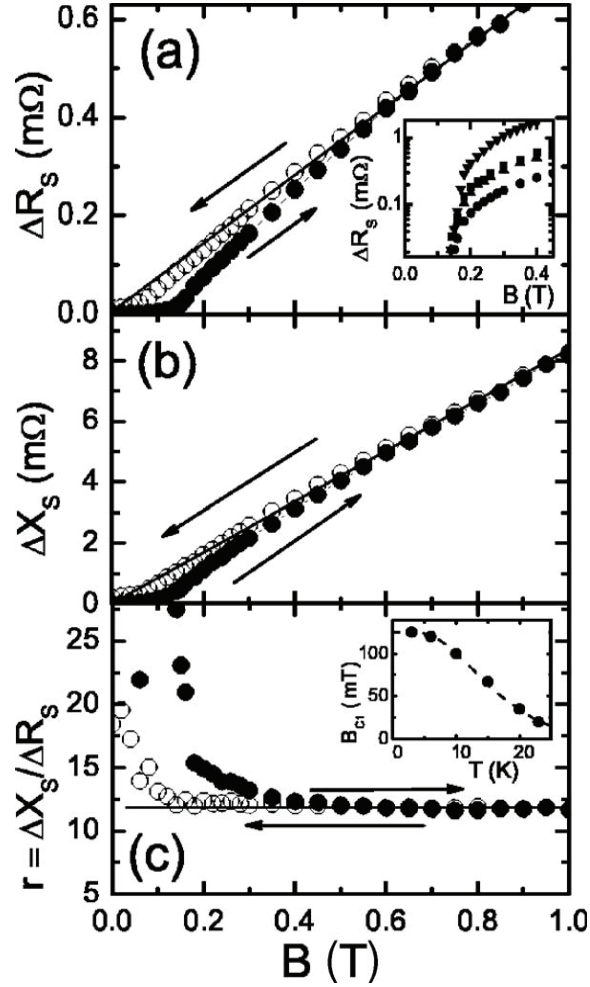
Figure 2.5: Field dependence of MgB_2 thin film measured by Zaitsev *et al.* [24]. Variation of the (a) microwave surface resistance, (b) reactance and (c) ratio of reactance and resistance versus the applied dc magnetic field at T=6K and f_0=5.75GHz. The solid ones are field-up measurements, while the open symbols mark the field-down ones. (from Zaitsev *et al.*, 2007, p.212505-1)

B_{c1} in the temperature dependence experiment. They also pointed out that both the relatively high value of the ratio $(\Delta X_s/\Delta R_s)$ and their frequency dependence indicate a weak effect of the flux creep for the microwave loss in MgB_2 films.

For the work presented in this thesis, we related microwave resistance to loss due to vortices and microwave reactance to frequency shift, and plot the ratio r versus

magnetic field [16]. By fitting our data with the model of Coffey and Clem [57] and Brandt [58], we have found flux creep as Zaitsev *et al.* found in their work. The work I have discussed here on the microwave response of vortices in superconductors has primarily involved large magnetic fields, at least several orders of magnitude larger than the Earth's field. On the other hand, superconducting resonant circuits for qubits and detectors are typically operated in relatively small magnetic fields, of the order of 100 μT or less and are fabricated from low-T_c thin films that are often type-I superconductors in the bulk. In this thesis, we report on measurements, such as probing the magnetic field and frequency dependence of the microwave response, of a small number of vortices using resonators fabricated from thin films of Re and Al – common materials used in superconducting resonant circuits for qubits and detectors.

Chapter 3

Superconducting Microwave resonators

The resonant circuits can be used to probe small changes in the response due to the introduction of a few vortices. Several resonant circuit geometries are possible, but the coplanar waveguide (CPW) geometry is particularly straightforward for implementing with thin films and is a common configuration used in superconducting qubit and Microwave Kinetic Inductance Detectors(MKID) circuits. In this chapter, all the possible transmission lines are discussed first, then the concept of S parameters from Network analyzer is presented, along with some basic information about half and quarter wavelength resonators. At the end, there is a survey of loss mechanisms in superconducting resonators.

3.1 Key concepts in microwave circuits

A transmission line is a specialized line that can be designed to carry alternating current of microwave frequency. This line is a system of at least two conductors for guiding electromagnetic signals from a source to a load. Figure 3.1 is a coaxial cable which has a core wire, surrounded by a non-conductive material (which is called
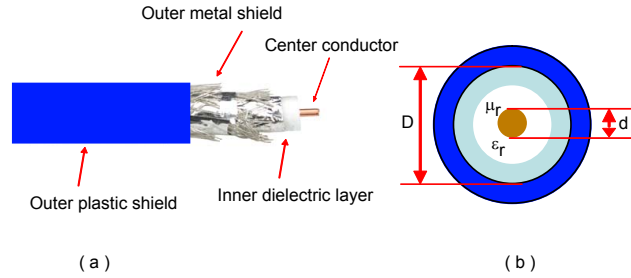
Figure 3.1: (a) 3D and (b) 2D views of coaxial cable. There are two round conductors in which one completely srrounds the other, with the two sperated by a dielectric layer.

dielectric or insulation), and then surrounded by an shielding which is often made of braided wires. The dielectric keeps the core and the shielding apart. The capacitance per length C' and inductance per length L' can be calculated based on the geometry of the coaxial cable. The characteristic impedance Z_0 and the propagation velocity V_P of the wave in a transmission line can be expressed as:

$$V_P = \frac{1}{\sqrt{L'C'}},\tag{3.1}$$

$$Z_0 = \sqrt{\frac{L'}{C'}}.\tag{3.2}$$

3.1.1 Transmission Lines

When we design a superconducting device to detect the microwave response due to the vortices, the first step is to decide what kind of transmission line should be employed to meet our needs. Since there are several types of transmission lines and waveguides are being used commonly today, it is better to know them before we finally choose.

3.1.1.1 Stripline

A stripline is a planar-type of transmission line which functions well in microwave integrated circuits and photolithographic fabrication. The geometry of a stripline is shown in Figure 3.2(a). A thin conducting strip of width s is centered between two
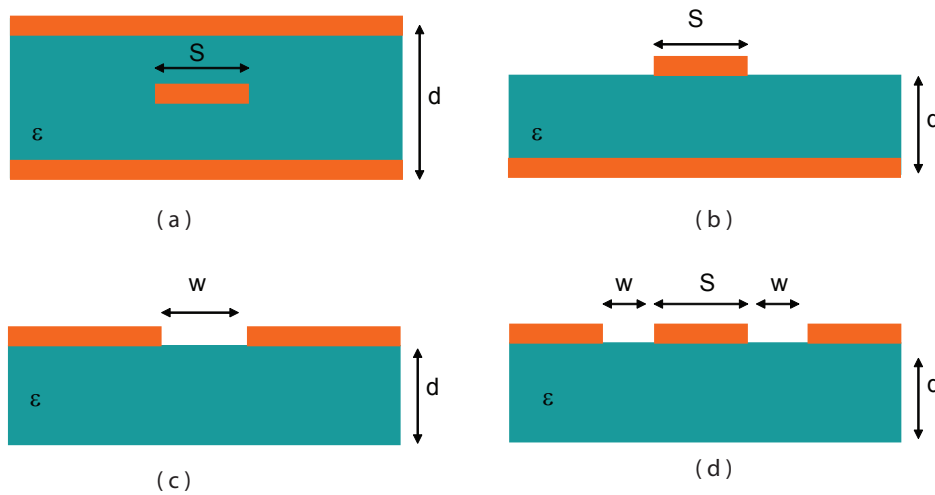
Figure 3.2: Transmission lines (a) stripline, (b) microstrip, (c) slotline, (d) grounded coplanar waveguide are being portrayed. The thickness of the cielectric layer is d, the width of signal line is s and the gap between center conductor and grounded plane is w.

wide conducting ground planes of separation d, and the entire region between the ground planes is filled with a dielectric.

3.1.1.2 Microstrip

A microstrip line is one type of planar transmission lines, primarily because it can be fabricated by photolithographic processes and is easily integrated with other passive and active microwave devices. The geometry of a microstrip line is show in Figure 3.2(b). A conductor of width s is printed on a thin, grounded dielectric substrate of thickness d and relative permittivity ϵ.

3.1.1.3 Slotline

In 1968, a slotline, a planar transmission structure, was proposed for use in microwave integrated circuits(MICs) by Cohn [60]. Figure 3.2(c) shows the basic slotline configuration. It is comprised of a dielectric substrate with a narrow slot etched in the metalization on the same side of the substrate, and there is no metal on the other

side of the substrate. Since it is a planar structure, it is suitable to use in microwave integrated circuits.

3.1.1.4 Coplanar waveguide

A coplanar waveguide (CPW) fabricated on a dielectric substrate was first demonstrated by C. P. Wen [61] in 1969. Coplanar waveguides are a type of planar transmission line used in (MICs) as well as in monolithic microwave integrated circuits (MMICs). With processing technology improving, the microwave circuits could be completely integrated and they were MMIC. Conventional coplanar waveguide is formed from a conductor separated from a pair of ground planes, both on the same plane, on top of a dielectric medium. A variant of coplanar waveguide is formed when a ground plane is provided on the opposite side of the dielectric; and it is grounded coplanar waveguide. A grounded coplanar waveguide is shown in Figure 3.2(d).

The unique feature of this transmission line is that all of the conductors are on the same side of the substrate. This attribute simplifies manufacturing and allows fast and inexpensive characterization using on-wafer techniques [62]. In my research, grounded coplanar waveguide has been used to design a microwave resonator due to its advantage; such as the convenience for patterning thin superconducting films. For field cool (refer to chapter 4) measurements, the configuration of the CPW also insures the vortices stay in the resonator traces.

According to Simons [63], the impedance can be solved analytically for a semi-infinite dielectric for coplanar waveguide transmission lines,

$$Z_0 = \frac{30\pi}{\sqrt{(1+\epsilon)/2}} \frac{K(k_0')}{K(k_0)}, \tag{3.3}$$

$$k_0 = \frac{s}{s+2w}, \tag{3.4}$$

$$k_0' = \sqrt{1-k_0^2}. \tag{3.5}$$

Where s is the width of the center strip, w is the width of the slots in the ground plane as in Figure 3.2 (d), and $K(k_0)$ is the complete elliptic integral with modulus k_0. We

Figure 3.3: Agilent N5230A network analyzer

design CPW signal line to be $s = 4\mu m$ and $w = 1.5\mu m$. Taking the fabrication into account, such CPW line yields almost 50 Ω. The detailed discussion can be found in chapter 4.

3.1.2 Microwave network analysis

Throughout my research, a microwave network analyzer as shown in Figure 3.3 was used to take measurement's data. The model is 'Agilent N5230A' network analyzer which has four ports, and the measurement frequency range is from 300KHz to 20GHz. We, however, only use two ports and up to 11GHz frequency in our measurements due to the limitation in the operating frequency range (0.5 - 11 GHz) of the low temperature high electron mobility transistor (HEMT) amplifier used. The HEMT is not part of network analyzer, and we use it in our refrigerator to boost the weak signal transmitted through our resonator chip. There are some basic theory of network analyzer.

3.1.2.1   S parameters

S parameters corresponding to the element scattering matrix. The concept was first popularized around the time that Kaneyuke Kurokawa of Bell Labs wrote his 1965
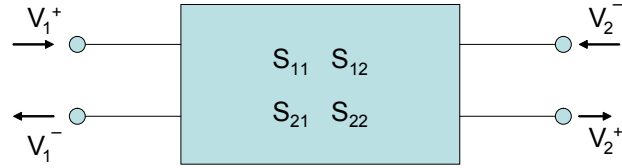
Figure 3.4: Two port network

IEEE article Power Waves and the Scattering Matrix, and this concept later helped introduce the first microwave network analyzer [62].

The scattering matrix is a mathematical construct that quantifies how energy propagates through a multi-port network. The S-matrix is what allows us to accurately describe the properties of complicated networks as a simple 'black box'. S parameters are complex quantities because both the magnitude and phase of the input signal can be changed by the network. They are defined for a given frequency and system impedance, and vary as a function of frequency for a network. For an N-port network, the S matrix contains N^2 coefficients (S-parameters), each one representing a possible input-output path.

For instance, Figure 3.4 is a two-port network. If we assume that each port is terminated in impedance Z_0, we can define the four S parameters of the two port as

$$S_{11} = \frac{V_1^-}{V_1^+}, \tag{3.6}$$

$$S_{12} = \frac{V_1^-}{V_2^+}, \tag{3.7}$$

$$S_{21} = \frac{V_2^-}{V_1^+}, \tag{3.8}$$

$$S_{22} = \frac{V_2^-}{V_2^+}, \tag{3.9}$$

Each two port S parameter has the following generic descriptions:

- S_{11} is the input port voltage reflection coefficient

- S_{12} is the reverse voltage transmission coefficient

- S_{21} is the forward voltage transmission coefficient

- S_{22} is the output port voltage reflection coefficient

Generally speaking, S_{mn} measures how much signal reflects(transmits) from port n to port m.

3.2 Introduction to microwave resonators

The operation of microwave resonators is similar to that of the lumped-element resonators. For our distributed microwave resonators, we can use the transmission line with various lengths and terminations, such as open or short end, to form either half or quarter wavelength resonators, and half and quarter wavelength resonators can be modeled to series and parallel RLC lumped-element equivalent resonate circuits. In this section, these two kinds resonators and their corresponding equivalent circuits will be discussed.

3.2.1 Difference between lumped and distributed elements

At low frequency, the circuits can be treated as lumped elements and we can understand the circuits by traditional lumped concepts. For example, one can form an electrical resonator by combining an inductor and capacitor. In such circuits, all the components are assumed to be single points, so that the dimensions of the components are not important. The ability to treat this as a circuit composed of discrete elements depends on the wavelength on resonance relative to the size of the circuit elements When it comes to microwave frequencies, the physical size of resist, capacitor and inductor can't be neglected. For instance, the wavelength on a transmission line for a typical microwave frequency, such as 10 GHz, is 3 cm which is comparable to the phisical size of lumped elements. In this regime, for example, wires must then
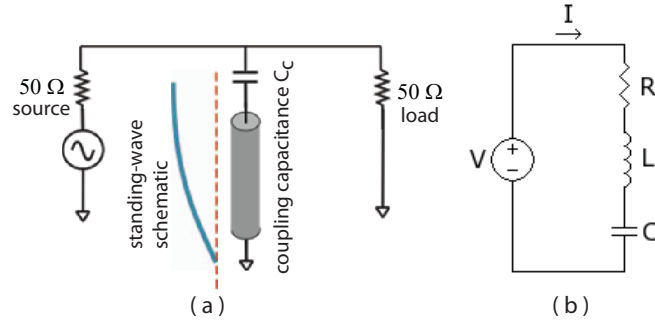
Figure 3.5: (a)Configuration of a quarter wavelength resonator. There are 50 Ω source, load resistance, and coupling capacitance. The standing-wave schematic is presented. (b) The corresponding equivalent circuit near the fundamental resonance of the 1/4-wave resonator. Capacitor c is equivalent capacitor for coupling capacitor and distributed capacitor.

be treated as transmission lines, that is to say, we have to consider the width, length and the thickness of the transmission line to characterize its electrical properties. If the wavelength is however much smaller than the length of the component, it can be treated as a lumped system. To summarize, the way to tell whether the circuit is lumped or distributed depends on the size of the circuit element relative to the shortest wavelength of interest.

In spite of their difference, there are still some links between lumped and distributed elements. The concepts from lumped circuirts can help to better understand a distributed circuits.

3.2.2   Half and quarter wavelength resonators

3.2.2.1   Quarter wavelength resonators

For quarter wavelength resonators, we use the layout as in Figure 3.5(a). There is one transmission line with one end shorted to ground and the other side connected with a capacitor to a feedline.

Figure 3.5(b) is the series RLC lumped element equivalent circuit for a quarter
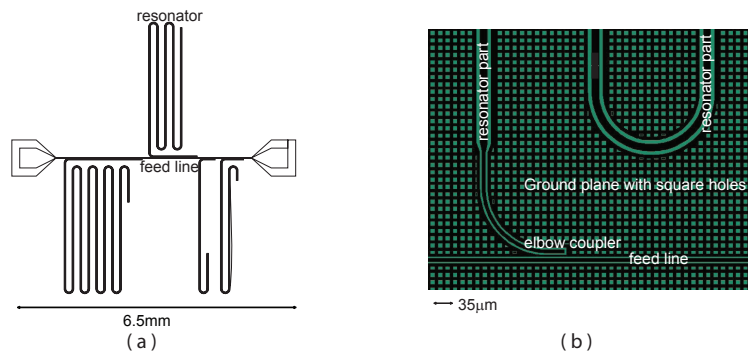
Figure 3.6: (a)quarter wavelength resonators with resonance at 1.8GHz, 3.2GHz, 6.8GHz and 10.8GHz respectively (b)zoomed in view of different parts of one quarter wavelength resonator (black part is metal Al)

wavelength resonator near resonance. The input impedance is

$$Z_{in} = R + i\omega L - i\frac{1}{\omega C} \tag{3.10}$$

At resonance, the energy stored in magnetic and electric energy are equal, the input impedance is simply real $Z_{in} = R$. The value of ω_0 then can be easily derived as

$$\omega_0 = \frac{1}{\sqrt{LC}} \tag{3.11}$$

An advantage of using quarter wavelength resonator in the research presented here is that multiple resonators can be capacitively coupled to one common feedline in one sample. Figure 3.6(a) shows four resonators. In Figure 3.6(b), different parts are labeled. A signal is going through a feedline, and the resonator can be excited by an elbow coupler. We will discuss how to design elbow length and center frequency of resonators in the next chapter.

Without these quarter wavelength resonators, all the power would be transmitted through the feedline so the base line level of S_{21} in Figure 3.7 is 0 dB. However, because of these resonators, input signal resonates near their center frequencies, forms a transmission dip, and shows a steep phase change. In reality, any lossless transmission line has some insertion loss, not to mention the solder joints and attenuators we used
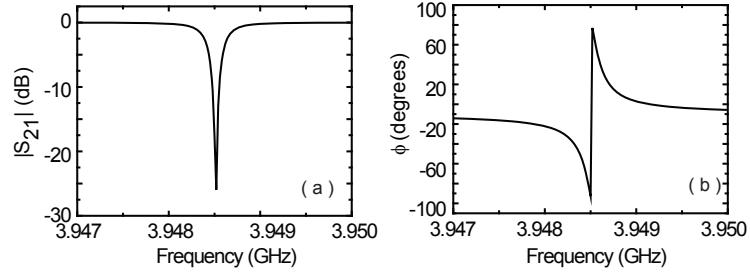
Figure 3.7: Simulation results of a quarter wavelength resonator from SONNET; a quarter-wavelength resonator produces a dip in the magnitude(a) and a steep slope in the phase(b) of transmission on resonances.

in our circuits, so the base line of the transmission S_{21} away from resonances would not close to 0 dB. A high frequency electromagnetic software named SONNET was used to simulate the above circuit, and the simulation results presented in Figure 3.7.

Since one end of resonator parts is shorted to ground, the resonance can occur when the wavelength on this transmission line is 1/4 of the λ, and harmonic resonance, such as $\frac{n\lambda}{4}$, n = 1, 3, 5, $\cdots$. There are only odd harmonics because of the boundary conditions; voltage node at the grounded end and antinode at the other end of the resonators. For example, our $\sim$ 3.95GHz quarter wave resonator also resonates at 11.85GHz $\cdots$. The quarter wavelength resonator is employed in my experiment because the multiplexing scheme which was developed recently for MIKIDs can be used; several resonators can be measured with the same temperature or magnetic field background.

3.2.2.2   Half-wavelength resonators

A half-wavelength resonator is constructed by a transmission line and a pair of coupling capacitors on each end, as shown in Figure 3.8(a). The coupling capacitors on either end could be a small gap or interdigital capacitors, depending on the level of capacitance required. From a pratical view, it is easy to fabricate a small gap or inter-digital capacitors at the ends for a thin-film transmission line. Putting capacitors at
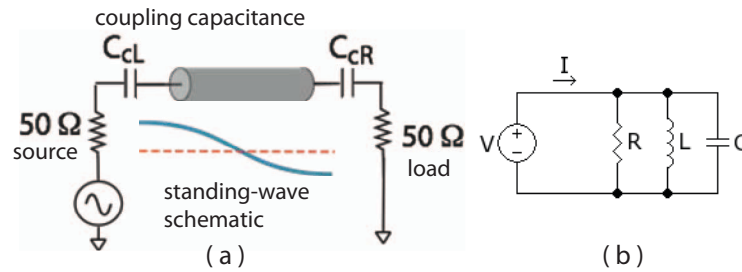
Figure 3.8: (a)Configuration of a half wavelength resonator. There are 50 Ω source, load resistance, and coupling capacitance at both sides of the 1/2-wave resonator. The standing-wave schematic is presented. (b) The corresponding equivalent circuit near the fundamental resonance of the 1/2-wave resonator. Capacitor c is equivalent capacitor for coupling capacitor (C_{cL} and C_{cR}) and distributed capacitor.
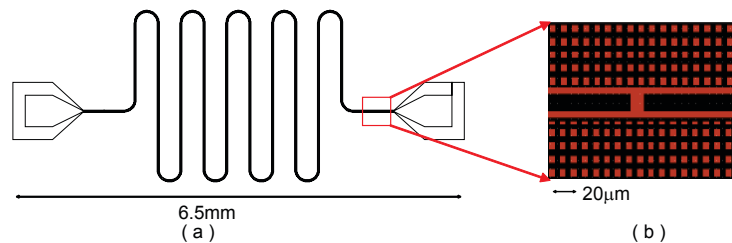
Figure 3.9: (a)a half wavelength resonator with resonance at 2.7 GHz, (b)close look of the coupling capacitors (black part is metal Al)

both ends of the transmission line imposes boundary conditions with a current node and voltage antinode at either end, thus the fundamental standing-wave resonance corresponds to half a wavelength. Half-wavelength resonators can be modeled as a parallel RLC lumped-element equivalent resonant circuits near resonance frequency [62] as Figure 3.8(b) shows.

We have built one half wavelength coplanar waveguide resonator as the Figure 3.9. In the Figure 3.9(a), the width of this resonator is 10 μm with the gap 4.2 μm at both sides to insure the characteristic impedance to be $\sim$ 50 Ω; this is extensively discussed in chapter 4. We put a 10 μm gap capacitor at each side of this resonator as Figure 3.9(b) indicates. We used SONNET to simulate the above circuit and it resonates at $\sim$ 2.7GHz. The simulation results are shown in Figure 3.10. For
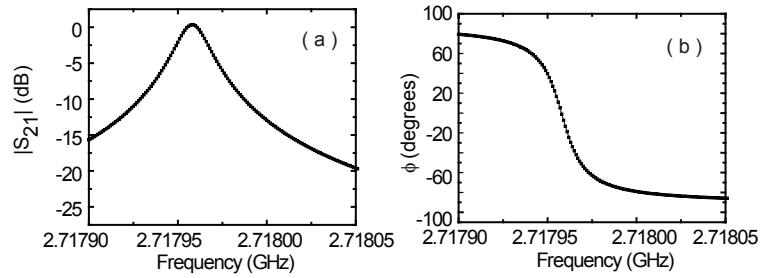
Figure 3.10: Simulation results of a half wavelength resonator for SONNET; a half wavelength resonator produces a peak in the magnitude(a) and a slope in the phase(b) of transmission on resonances.
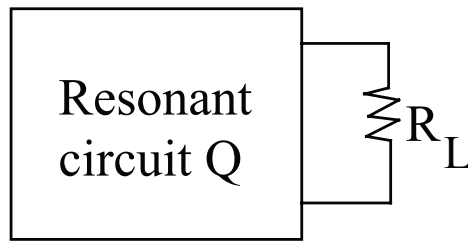
Figure 3.11: A resonant circuit connected to an external load R_L

a half wavelength resonator, the input signal only passes through near its resonance frequency, resulting in a transmission peak on resonance. Meanwhile, the phase varies rapidly as the frequency passes through the resonance as the Figure 3.10(B) shows.

Similar to quarter wavelength resonators, it has its harmonics at $\frac{n\lambda}{2}$, n = 1, 2, 3, $\cdots$. The 1/2-wave resonator has all harmonics, while the 1/4-wave resonator only has odd harmonics.

3.2.3 Coupling

For a resonator, we are always interested in quality factor of the circuits. According to Pozar [62], if the circuit is loaded with R_L, then the loaded Q (Q_{fit} is used in data

analysis) can be expressed as

$$\frac{1}{Q} = \frac{1}{Q_c} + \frac{1}{Q_i} \tag{3.12}$$

with Q_c is defined as an external quality factor and Q_i is internal quality factor. Pozar has defined the ratio of Q_i/Q_c to be g, then there are three cases:

$$\begin{cases} g < 1 & \text{Resonator is under-coupled to the feedline.} \\ g = 1 & \text{Resonator is critical-coupled to the feedline.} \\ g > 1 & \text{Resonator is over-coupled to the feedline.} \end{cases}$$

When we design our resonator to detect the properties of vortices inside resonator, we purposely designed our resonator to be slightly over coupled with no vortices present. so that the resonances are still observable when vortices are added and the internal quality factor decreases. In chapter 4, The magnitude of Q_c and the design process are extensively discussed.

In our experiment, without any field applied, the loss of the resonator is contributed by

$$\frac{1}{Q_{fit}} = \frac{1}{Q_c} + \frac{1}{Q_i} \tag{3.13}$$

Here Q_{fit} is exacted from the measurements by fitting and $1/Q_i$ is the intrinsic loss which is comprised of:

$$\frac{1}{Q_i} = \frac{1}{Q_{qp}} + \frac{1}{Q_{rad}} + \frac{1}{Q_{TLS}} + \frac{1}{Q_{diel}} + \cdot \tag{3.14}$$

$1/Q_{qp}$ is the loss due to quasiparticles, $1/Q_{rad}$ is loss from electromagnetic radiation, $1/Q_{TLS}$ is loss from two level system which will be discussed in detail in chapter 8 and $1/Q_{diel}$ is loss from dielectric. Q_{rad} and Q_{diel} are governed by geometry and material parameters. These loss terms add like resistors in parallel.

Vayonaskis [64] analytically calculated the radiation loss for a straight CPW half and quarter wavelength resonator with a semi-infinite dielectric; Eq. 3.15 is the equation to get Q_{rad} for half wavelength resonator:

$$Q_{rad} = \frac{\pi(1+\epsilon)^2}{8\epsilon^{2.5}} \frac{\eta_0}{Z_0} \frac{1}{I(\epsilon, n)} \frac{1}{n} \left(\frac{L}{S}\right)^2 \tag{3.15}$$

here S is the width of the center strip width plus one width of the gap next to the center strip, ϵ is the substrate dielectric constant, $\eta_0 = 377\ \Omega$ is the impedance of free space, Z_0 is the characteristic impedance of the line, n is the mode number and L is the length of the resonator. $I(\epsilon, n)$ has been calculated by Vayonaskis for the first ten modes and listed in the following table:

Table 3.1: Table of $I(\epsilon=10, n)$ for half wavelength resonator

n	1	2	3	4	5
$I(\epsilon = 10, n)$	0.330	0.941	1.51	2.08	2.66

The Radiation loss for a straight CPW quarter wavelength resonator is:

$$Q_{rad} = \frac{\pi(1+\epsilon)^2}{2\epsilon^{2.5}} \frac{\eta_0}{Z_0} \frac{1}{I'(\epsilon, n)} \frac{1}{n - 0.5} \left(\frac{L}{S}\right)^2 \tag{3.16}$$

With $I(\epsilon, n)$ listed in this table:

Table 3.2: Table of $I(\epsilon=10, n)$ for quarter wavelength resonator

n	1	2	3	4	5
$I(\epsilon = 10, n)$	1.62	4.92	7.26	9.55	11.9

For our CPW quarter wavelength resonator on sapphire ($\epsilon \approx 10$), we can use equation 3.17:

$$Q_{rad} = 5.6 \left(\frac{L}{S}\right)^2 \tag{3.17}$$

This calculation is not accurate due to the approximations that have been made, but it at least gives a rough estimation. For the geometry we use, S $= 18\ \mu m$ if we design a $12\ \mu m$ wide resonator, L $= 2.97$ mm ($f_0 \approx 10.8$GHz) for the highest center frequency we have ever made; then the rough radiation loss is 2.5×10^6. For our resonator, Q_c is usually designed to be around 2.0×10^5. By comparing the magnitude of Q_c and Q_{rad}, Q_{fit} isn't limited by radiation loss and Q_{rad} can be neglected in our analysis.

In a nonconstant electric field, dielectric loss is a kind of energy loss that heat a dielectric materials. For example, a capacitor incorporated in an alternating-current

circuit is alternately charged and discharged each half cycle. During the alternation of polarity of the plates, the charges must be displaced through the dielectric first in one direction and then in the other. The change of the charges position leads to a production of heat through dielectric loss.

At nonzero temperatures, the equilibrium state of a superconductor consists of the Cooper pairs and thermally excited quasiparticles. The quasiparticle density n_{qp} increases exponentially with increasing temperature. These charge carriers control the high frequency response of the superconductor through the complex conductivity $\sigma_1 - i\sigma_2$. The real part of σ_1 represents the conductivity from quasiparticles and the imaginary σ_2 is due to the superconducting condensate [34, 65]. According to Mattis-Bardeen theory of the electrodynamics of BCS superconductors which will be discussed extensively in Chapter 5.

If we intentionally put vortices into our resonator, then equation 3.13 changes to:

$$\frac{1}{Q_{fit}} = \frac{1}{Q_c} + \frac{1}{Q_i} + \frac{1}{Q_v} \tag{3.18}$$

From equation 3.18, if the resonator is too weakly coupled (Please refer to the previous chapter for the concepts of critical-, weak-, and strong-coupling), then the resonace dip would be very sharp, adding only a small number of vortices would cause the dip to vanish. On the other hand, the resonator shouldn't be designed overly coupled either, since the dip would be too broad and any change of f_0 wouldn't be easily detected. We have to design Q_c comparable to Q_v and Q_{qp} in order to easily measure any change of the loss due to changes of the vortices. However, overcoupled resonators with accordingly low quality factors are ideal for performing fast measurements of the state of a qubit integrated into the resonator [66, 67].

3.3 Survey of loss mechanisms in superconducting resonators

Low loss microwave resonators fabricated from superconducting thin films are playing key roles in many recent low-temperature experiments. For instance, high-Q superconducting microwave thin film resonators have shown significant promise to serve as qubits for forming the elements of a quantum computer [1]. In addition, there has been much progress in the development of superconducting Microwave Kinetic Inductance Detectors (MKIDs), which are highly sensitive photon detectors for astrophysical measurement applications [4] Because superconducting qubits or MIKDs are fabricated by the same materials and processes as resonators, the study of loss mechanisms that limit the Q in these resonators is useful for understanding and designing hight Q resonators [11, 13, 68, 69].

A variety of factors determine the quality factor of superconducting microwave resonators. In order to improve the performance of such circuits, there have been many recent efforts to probe the effects of microwave loss in a variety of areas, including dielectric loss in the substrates and thin-film surfaces that form the microwave superconducting circuits. [11–13, 68]. Such dielectric loss at higher powers and temperatures has been extensively reported [70]. Later, at low temperatures and low excitation strengths, it has been shown that the microwave performance of amorphous dielectric material displays significant excess loss [68]. Such loss is well modeled by two-level defects (TLS) system in the dielectric, which absorb and disperse energy at low power but become saturated with increasing voltage and temperature [11, 71]. TLS are found in most amorphous materials and it can be significantly reduced by using better dielectrics [11]. The introduction of TLS is extensively discussed in chapter 8.

In Ref. [12], Gao *et al.* fabricated five Nb resonators with CPW structure, which is similar to our design. Gao *et al.* have a model for how the surface TLS should

influence the resonance frequency of the resonator and they can relate this to the CPW geometry; roughly inversely proportional to the strip width, so the TLSs are distributed on the surface of the CPW rather than in the bulk substrate. Later, Wenner *et al.* investigated further and found dominated surface loss was from metal-substrate and substrate-air interfaces.

Martinis *et al.* in Ref. [11] reported dielectric loss from TLS which can be significantly reduced by using better dielectrics. Barends *et al.* in Ref. [13] had temperature dependence measurements on NbTiN resonators which are covered with SiO_x dielectric layers of various thickness and found out the logarithmic temperature dependent increase in the resonator frequency scales with the thickness of the layer of SiO_x.

Sage *et al.* [14] studied the excitation power dependence of the Q values of superconducting CPW resonators fabricated from Nb, Al, Re, and TiN metals deposited on sapphire, Si, and SiO2 and found that it depends strongly on both materials and geometry. They also find that at low excitation power, the loss is enhanced due to the presence of TLS located on the surface of the superconducting metal.

Later, Wenner *et al.* in Ref.[15] modeled and simulated the magnitude of the loss from interface surfaces in the resonator. By investigating the dependence on power, resonator geometry and dimensions, the dominant surface loss was found to come from the metal-substrate and substrate-air interfaces. The magnitude of the loss from the above two interfaces has 100 times bigger than the loss from metal-air interface. This information provides a guide that using microstrips with clean dielectrics can greatly reduce the loss.

In the presence of magnetic fields, many superconductors are threaded by vortices over a large range of magnetic field and temperature. We will demonstrate another possible loss mechanism in thin-film superconducting resonators, and it is the dissipation due to vortices trapped in the superconducting traces. If such superconducting resonators are not cooled in a sufficiently small ambient magnetic field, or if large pulsed fields are present for operating circuits in the vicinity of the resonators, vor-

tices can become trapped in the resonator traces, thus providing another loss channel. The presence of even a few vortices can substantially reduce the resonator quality factor [16]. This can play an important role in the design of superconducting microwave devices. Thus, understanding this dissipation mechanism is important for the design of microwave superconducting circuits.

Chapter 4

Experimental setup and device design

In this chapter, experimental setup, resonator design and fabrication is described in detail. I discussed several measurement strategies, such as the experiment of field cool, temperature dependence and power dependence to probe the microwave responses of our superconducting resonators. I explained the reasons to choose a layout of multiplex several quarter wavelength resonators by capacitive-coupling to a common feedline, then I intensively showed how to design microwave resonators in terms of center frequency f_0, coupling quality factor Q_c. A simulation by SONNET softerware is employed to verify if our circuits meet our needs. Lithography, etching, dicing and packaging are used to fabricate our superconducting CPW resonators. At the same time, a fitting routine to analyze our resonator data is presented.

4.1   Measurement setup and strategy

4.1.1   Measurement Setup

The purpose of our experiments is to measure responses of vortices at microwave frequencies and our most common approach for introducing vortices involves field-cooling as I mentioned in chapter 2, which requires heating above T_c and cooling through T_c for each different magnetic field. The typical superconductors that we use are Al and Re, and their T_c is roughly ∼1.15K and ∼1.7K respectively. The value of superconductor's transition temperature limits type of cryogenics and the places on the cryogenics.

There are different types refrigerators we can use to cool down our superconducting resonator: a blue Dewar (liquid Helium/Nitrogen bath Dewar), a Janis 3He refrigerator and a dilution refrigerator. When an insert is in the Helium bath inside the blue Dewar, we can pump on the liquid Helium and a temperature around 1.8K can be reached. For the 3He refrigerator, the lowest temperature is around 280mK, while the dilution refrigerator has a much lower base temperature around 30mK.

Almost all of our measurements are carried out by the Janis 3He refrigerator. The blue Dewar is easier to operator and cool samples down faster, but we can't choose to do our experiment with this because our resonator is either made of Al or Re, and the Tc of both these metals is lower than the base temperature of the blue Dewar. Also it is not practical to take measurements on the dilution refrigerator since for some of our experiments, we need to heat and then cool the sample multiple times. It wouldn't be easy to heat the whole dilution refrigerator, and further more, it would take a long time to cool the refrigerator back down to the temperature we needed. Because the dilution refrigerator carries much bigger thermal mass than ^{3}He refrigerator, the cooling time is long and it is difficult to heart ^{3}He/^{4}He mixture above 1K.

Figure 4.1 shows the measurement setup. A microwave driving signal comes out of one port of the network analyzer at room temperature, it goes into the top of the Janis
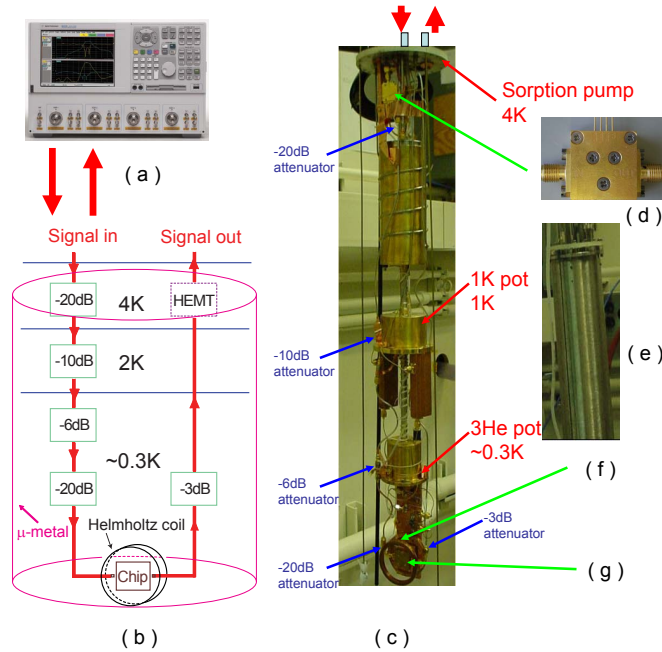
Figure 4.1: (a) N5230A PNA-L network analyzer, 4-ports, up to 20 GHz. (b) schematic of our measurement set up. (c) Janis 3He refrigerator. (d) High electron mobility transistor (HEMT) amplifier from Caltech. (e) μ-metal (f) Homemade Helmholtz coil. (g) A sample in the brass holder mounted in the middle of the customized PCBoard.

3He refrigerator; then through a lossy stainless-steel semirigid coaxial cable on the refrigerator. The signal travels by several cold attenuators at different temperature stages, and finally passes through the sample. The sample containing the resonators, which needs to be designed, is mounted and wirebonded into a custom chip carrier with ports for transmitting signals through the feedline. The chip sits in the middle of a home made Helmholtz coil. The low cryogenic High Electron Mobility Transistor (HEMT) amplifier that is mounted on the 4 K flange of the refrigerator amplifies the output signal before returning it to the other port of the network analyzer. A 6 dB attenuator is installed at the output signal port to suppress spurious resonances and reduce noise fed back from the HEMT input. S parameters in frequency domain are obtained on the network analyzer.

According to our setup in Fig. 4.1 (b), we used one lossy cable on the 3He
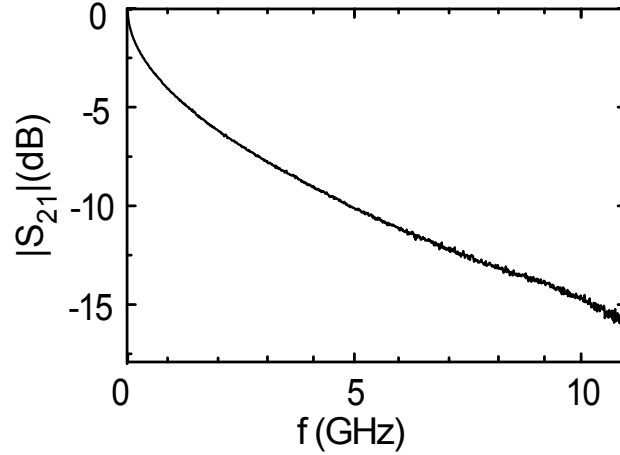
Figure 4.2: The plot of transmission of a Janis lossy cable from 300KHz to 11GHz

refrigerator to be our signal input. The lossy cable decreases the magnitude of S_{21} as Figure 4.2. At the same time, these attenuators along the signal line and even those solder joints attenuate our input signal. The output line is the lossless transmission cable with the low temperature HEMT which amplifies the output signal. The gain and the noise temperature of the HEMT is as in Figure 4.6 (data sheet from Caltech) later in this chapter.

By considering all these loss and gain in our measurement, we can estimate our S_{21} at different frequency. For example, at 1GHz, the lossy cable from Janis has around -5 dB loss, all the attenuators on both input and output line are -59dB, and the HEMT provides 36 dB gain. Counting the loss from the rest of the cables and solder joints, the base line of S_{21} would be around -30dB.

The purpose for putting all these attenuators is to reduce thermal noise and any interference from room temperature. As we all know, any thermal agitation of electrons in a conductor can generate noise. For a given bandwidth, the root mean square of the voltage, V_{tn}, is given by:

$$V_{tn} = \sqrt{4k_B T R \Delta f} \tag{4.1}$$

with Δf to be the bandwidth in hertz over which the noise is measured and k_B

is Boltzmann's constant in J/K. The thermal noise of the attenuator on high temperature stage can be attanuated by the ones at low temperature stages. There is the reason to put different attenuators on the different tempeature stages instead of putting all of them on ^{3}He pot.

Figure 4.1(e) is a μ-metal can used to prevent any external magnetic field.

S parameters can be interface with computer by the network analyzer. Please refer to chapter 3 to understand S parameters. The network analyzer in our lab has four ports which allows to test s parameter with a 4×4 matrix, but we only use 2 ports for these measurements. In terms of frequency, it can measure up to 20GHz, however, because of the limitation of other instruments such as the working range of the attenuator and HEMT, we haven't designed a resonator that functions at higher than 11GHz.

The cryostat we used to cool testing samples down is model HE-3-SSV HE-3 refrigerator which is a vacuum can surrounds the active portions of the ^{3}He refrigerator to isolate them from the liquid ^{4}He bath in the dewar.

Figure 4.3 is the picture of our ^{3}He refrigerator. There are three different temperature stages (a sorption pump, 1K pot and ^{3}He pot) which are all located inside the inner vacuum can (IVC). The sorption pump is a cylinder filled with charcoals wich can release or store ^{3}He gas, and it also can reduce the saturated vapor pressure of the condensend liquid ^{3}He and cool down the system. 1K pot can provide low enough temperature to triger the condensation. The ^{3}He pot is used to hold liquid ^{3}He to provide the lowest temperature in this system, and our sample is attached at the bottom of the 3He pot.

When a sample is ready to be cooled down, we put the IVC and μ metal can on. The μ metal can provents the sample from any external magnetic fields. IVC isolates three temperature stages from the liquid ^{4}He bath in the dewar and provides a vaccum space. Liquid nitrogen is used first to bring the system down to 77K, then ^{4}He liquid is employed to continue cooling the components to $\approx$ 4K after blowing all
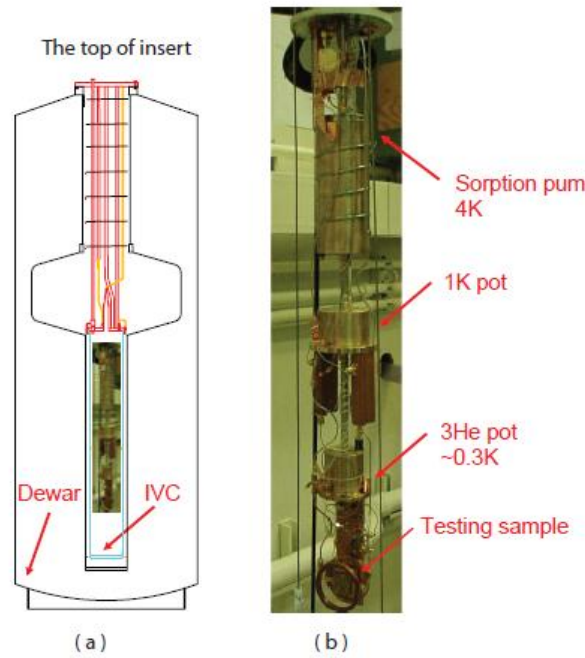
Figure 4.3: (a)Schematic of Janis ^{3}He refrigerator. (b)picture of Janis ^{3}He refrigerator.

the LN2 out of the Dewar. Finally the ^{3}He gas, which is sealed in a stainless steel can in the cryostat, comes into play. By heating the sorption pump to $\approx 45K$, ^{3}He gas is released for condensation. After the 1K pot is filled with liquid ^{4}He, we use the needle valve on the top of the cryostat to adjust the flow rate of liquid ^{4}He into the 1K pot to bring temperature below 2K. At this temperature, the ^{3}He gas can be liquefied, and drops into the ^{3}He pot. We can control the temperature of the sorption pump to ajust the pumping speed on the ^{3}He liquid, and this allows us to indirectly control the temperature of the measurement sample.

A Helmholtz coil is used in our experiment to provide a region of almost uniform magnetic field, or to be precisely, a region of magnetic field with small gradients. The frame of the Helmholtz coil, shown in Figure 4.4 A, is machined from a block of oxygen-free high thermal conductivity (OFHC) copper. OFHC copper is widely used in cryogenics. This type of copper is produced by casting electrolytically re-fined copper in a non-oxidizing atmosphere so it contains almost no oxygen or other
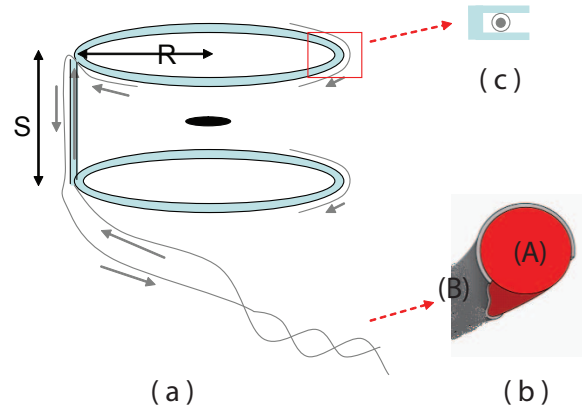
Figure 4.4: (a) Helmholtz coil, R = 1.25 inch and S = R (b) Single filament NbTi alloy clad with high conductivity cryogenic grade copper (A) NbTi superconducting wire, (B) copper cladding, (c) zoom in to show the groove of a coil and one wire in the groove.

impurities. The property of high thermal conductivity allows the metal reach the equilibrium quickly. A Helmholtz coil is comprised of two identical circular magnetic coils. The distance between these two identical coils should be equal to radius R of the coil (S = R). Each coil carries the current flowing in the same direction so they provide the same magnetic field. While the Helmholtz coil is wired, we put a cigarette paper under the wire to avoid the possibility that the frame and wire short each other. Every 3 to 4 turns, GE varnish is applied to secure and thermally anchor the wire. Along the joint axes of the two coils (the verticle part of the Helmholtz coil), there are two wires which carry opposite direction current so the magnetic field produced by these two wires are canceled out and doesn't affect the region of a nearly uniform magnetic field which is in the middle of two coils; the small black disk area (not to scale) in the Figure 4.4A. Unlike a long solenoid, Helmholtz coil allows access to middle so that we can install our testing sample at that place.

If the number of turns in each coil is n and the current flowing through the coils is I, then the magnetic flux density B at the center point is given by

$$B = \left(\frac{4}{5}\right)^{3/2} \frac{\mu_0 n I}{R} \tag{4.2}$$
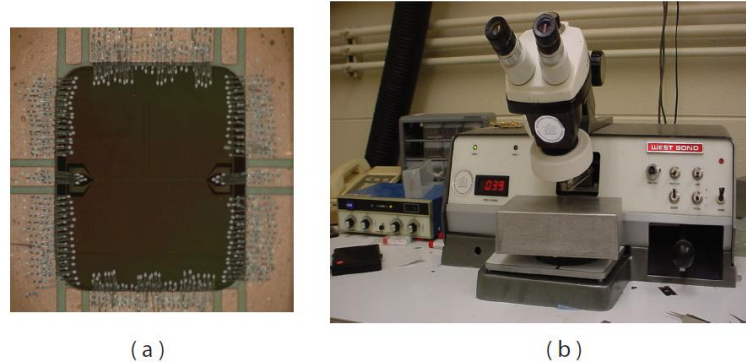
Figure 4.5: (a)A picture of PCBoard with a chip wire bonded in the middle (b) a picture of a wire bonder (model: West Bond 7400A)

where μ_0 is the permeability of free space ($4\pi \times 10^{-7}$ T $\cdot$ m/A), and R is in meters.

Our Helmholtz coil has a total of 230 turns for two coils (115 turns each coil). If we ignore the fact of each trun being not at the same location across the cross-section of the groove, we get 32.7 Gauss/A from the equation 4.2. After the Helmholtz coil was made, we used a '450 A' Gaussmeter from LakeShore to measure the actual magnetic field which gave us 34.4 Gauss/A.

The superconducting wire we use is the single filament NbTi alloy clad with high conductivity cryogenic grade copper. As we are doing low temperature measurements, and the Helmholtz coil is mounted on the 3He pot which is at 300mK, any heat directed from outside will affect the stability of the temperature of the 3He pot and the efficiency of how we cool it. Unfortunately the copper cladding is the perfect media for heat transfer, so we have to break it down, specially from the sorption pump (4K) to the 1K pot and between the 1K pot to the ^{3}He pot. The strong acid HNO_3 is used here. We dip 1 to 2 cm of superconducting wire into the HNO_3 liquid for almost 20 seconds which will etch the copper away but leave the NbTi. The magnetic field generated from Helmholtz coil comes from the exteral current which potentially creates heating if the resist of the wire is nonzero. Such heat can affect the temperature of ^{3}He pot and make it unstable. This is one more reason why we use the superconducting wire.
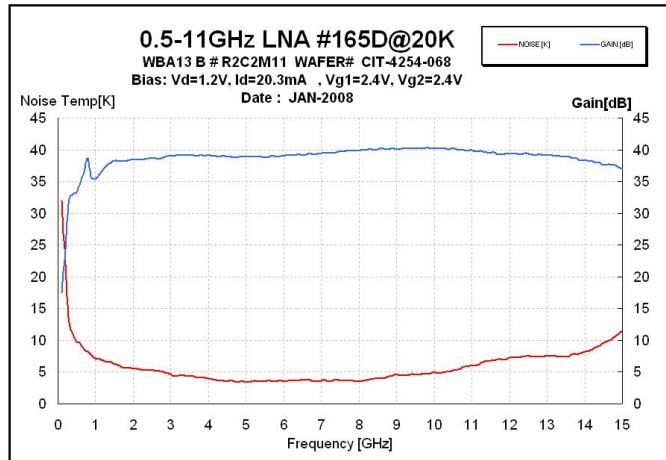
Figure 4.6: Noise temperature and gain of HEMT (model of 165D) up to 15GHz at 20K

In Figure 4.5(a), there are a lot of wires connected from PCBoard to test chip by a wire bonder. The PCBoard will be discribed in detail later. The model of the wire bonder in the picture 4.5(b) is the West Bond 7400A which makes interconnections between chip and substrate or between two chips. This machine makes bonds by application of ultrasonic energy. When we make bonds, different set of power and time is required for different metal surfaces and for the first and second bonds. Once the right power and time is set, the bonds won't be smashed and it will stick on the surface well. We direct the bonding tool toward PCBoard to make the first bond, after the beep, lift the bonding tool a little bit so that the wire will be fed automatically, then push the bonding tool away from the first bond towards substrate to make the second bond.

The wire of this West Bond 7400A used to make interconnections is annealed bare wire of aluminum 1% silicon with 0.00125 inch diameter. Such wire has an extremely homogeneous silicon distribution and its bonding deformation can produce the best bonding results.

A low temperature amplifier (HEMT) (Figure 4.1 d) is employed to amplify our output signal. This HEMT is a cryogenic, low noise, broadband amplifier which is commercially available and we obtained from Caltech. The particular one (165D) we

used on the 3He refrigerator works from 0.5 to 11 GHz, with a noise temperature of $T_N \approx 5$ K and a gain in our frequency range of ∼38 dB. The Figure 4.6 shows the noise temperature and gain of HEMT up to 15GHz at 20K. We built the bias circuit by ourselves to provide the bias voltage that the HEMT needs to function.

4.1.2   Measurement Strategy

After the resonators are designed and fabricated, the sample is wire bonded to a customized PCBoard, then put in the middle of the Helmholtz coil on the 3He insert. The Lakeshore temperature controller is used to monitor temperatures of all three different stages. As the chip is mounted on a 'L' shaped OFHC copper metal which is attached to the ^{3}He pot, the thermometer on the ^{3}He pot can read the temperature of the measurement's chip if we wait long enough for all mass on ^{3}He pot to reach an equilibrium thermal state. Hence, when the ^{3}He pot arrives at the desired temperature, it is time to take measurements. There are several types of measurements we take:

Field cool is the primary measurement procedure for many of our key experiments. If the starting temperature of the ^{3}He pot is below the critical temperature (T_c), we have to heat the ^{3}He pot above T_c so that the metal of the resonators becomes normal. For Al, we usually heat up to 1.4K, while for Re, we heat to 1.9K. The level is S_{21} is measured to assure all the vortices are released and the metal is normal. When the resonators are in normal state, current is driven through the Helmholtz coil to produce the desired magnetic field. We then cool the ^{3}He pot under the T_c with the magnetic field on. Vortices will then be trapped in the resonators. Measurements take place at low temperature and the field is maintained during measurements. By repeatedly heating and cooling through T_c, a lot of points are taken with different magnetic fields, we then can observe the variation of microwave response with different vortex densities.

The cooling time for each field point is approximately 30 minutes.

The following measurements are for characterization and calibration of our superconducting resonators. We have known that T_c is the temperature at which the electrical resistivity of the metal suddenly and completely drops to zero. The transmission coefficient (S_{21}) is different at temperatures above and below T_c since the feedline at normal state is much lossier than that at superconducting state, although it is not possible to see resonances in either case. When we cool down the ^{3}He pot with or without a magnetic field, we take data of S_{21} vs. frequency at different temperatures. We have written a labview program to take measurements perodically. After recording this data, we can plot S_{21} vs. temperature at any fixed frequency. A abrupt change of S_{21} indicates where the T_c is.

We have to cool down the ^{3}He pot slowly, the appropriate cooling speed is determined by the mass on the ^{3}He pot, so that each time we read the temperature from the temperature controller represents the actual temperature of the measurement's chip.

Some superconducting parameters, such as kinetic inductance fraction α and energy gap Δ, can be extracted from temperature dependence. We use the Lakeshore temperature controller to manipulate the temperature of the ^{3}He pot. We need to wait some time for the ^{3}He pot to reach equilibrium. However, from multiple experiences, we haven't been able to directly control the temperature of the ^{3}He pot above 600mK. So we changed the temperature of the sorption pump to indirectly control the temperature of the 3He pot. After knowing how to control the chip's temperature, we can record the s parameter at different Temperatures.

We measure power dependence at different temperatures and with different fields. Once a temperature and field is set, we excite signal at different powers from the network analyzer and record the corresponding S parameter. The data will be discussed later.

4.2   Microwave design and resonator layout

The purpose of our research is to understand the microwave response of superconductors, which can be profoundly influenced by the presence of vortices and the dynamics they exhibit at high frequencies. Our approach is to probe the different responses of microwave circuits due to the existence of vortices. As the microwave resonator has been widely used in qubit experiments which can be served as an element of a quantum computer [1] and of the superconducting Microwave Kinetic Inductance Detectors (MKIDs), which are highly sensitive photon detectors for astrophysical measurement applications [4], the microwave resonator has been employed to investigate the microwave response due to the vortices.

There are several planar transmission lines in common use today, such as stripline, slotline, microstrip and coplanar waveguide as chapter 3 is mentioned. They all have their advantages and disadvanges. The coplanar waveguide type of transmission line was chosen in our research project because it is a one layer device, and is particularly straightforward to implement with thin films.

We can design half-wavelength CPW resonators or quarter-wavelength CPW resonators. A $\lambda/2$ CPW resonator shows a peak in S_{21} vs. frequency plot, while a $\lambda/4$ CPW resonator produces a dip as its resonance. Both peak and dip are sensitive to the existence of vortices because vortices contribute a complex impedance – both loss and reactance – so this can have an influence on any type of resonator in general. By analyzing changes in frequency and bandwidth, we can infer the loss mechanic due to the vortices.

4.2.1   Frequency Domain Multiplexing

From a practical point of view, it is great if we can measure several resonators in a single cool down in experiments. Not only can this put the helium to good use, but also in one cool down, the same environment is provided to those resonators, meaning
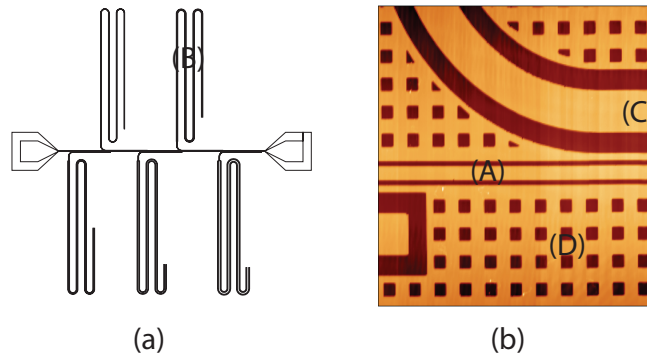
Figure 4.7: (a) Chip layout showing common feedline and five resonators. (b) Zoom in view of the feedline, resonator and ground plane.

we can measure the resonators by using the same superconducting film, with the same pinning and vortex viscosity, not to mention that, those resonators will be measured at the same temperature and magnetic field conditions. Such an arrangement is possible with a similar multiplexing scheme to what was developed recently for MKIDs, with multiple quarter-wave resonators of different lengths capacitively coupled to a common feedline [4, 5].

In contrast to a half wave CPW resonator, a quarter wave CPW resonator has the advantage of nearly perfect transmission away from its resonance frequency. The different lengths of resonators ensure different resonant frequencies, which avoid two resonators accidently overlapping each other. As with the resonators, our feedline also has a CPW layout, with a nominal impedance of 50 Ω, and runs across the centerline of the chip. Each resonator follows a serpentine path in order to fit on the chip, with an elbow bend at the open end, while the opposite end is shorted to the ground plane. The coupling capacitance between each resonator and the feedline is determined by the length of its elbow which is extensivly disscussed in this chapter later.

Figure 4.7(a) is one quadrant of our mask for using the multiplex technique. We put four different length resonators capacitively coupled to one common feedline. In figure 4.7, (A) is the common feedline which transmits the signal from one side to the other, and it has full transmission while away from all the resonances. Part

(B) is a meandered resonator. Because of space restrictions from the opening of the PCBoard, each resonator is meandered. The lines, however, have to be spaced out to avoid cross talk between different parts of the resonator. Part (C) is the elbow part of a resonator; none of two elbow shares the same section of the feedline to avoid the complication induced by the interaction of the electromagnetic field. Part (D) is the ground plane where is occupied by an array of squares.

All those squares in the ground plane are pretty critical in our measurements. Our purpose is to detect the changes of resonance due to those vortices in the resonator itself. Imagine we don't put those squares on the ground plane; while we cool down our resonator chip with a field, even though we have our μ-metal can on to prevent any external magnetic fields, we will still end up with vortices trapped in the ground plane. In threshold field imaging measurements for Nb strips of different widths, Stan *et al.* found that equation 4.3:

$$B_s = \frac{2\Phi_0}{\pi w^2} \ln(\frac{\alpha w}{\xi}) \tag{4.3}$$

with $\alpha = 2/\pi$ best described their observed values of B_{th}. where Φ_0 is the flux quantum $h/2e$, w is the width of the resonator trace and ξ is coherence length. According to their experiment, the threshold field for vortices getting into the ground plane is much smaller than that for the resonator. Hence, if we want to detect only the influence introduced by the vortices in the resonator, we have to break down the width of the ground plane by putting arrays of squares in so that the threshold field for vortices getting into the ground plane is much higher than the field we use in the experiment. For example, in chapter 6, we designed our resonator to be around 12 μm which is three times wider than the ground plane webbing, such that there would be almost a ten times range of cooling field with vortices only trapped in the resonator.

4.3   Resonator design parameters

4.3.1   Characteristic impedance

The signal flows along the transmission line to the feedline, goes out through the output transmission line, then is amplified by HEMT before it returns back to network analyzer. The characteristic impedance of the microwave transmission lines is 50 Ω. In order to maximize the power transfer and minimize reflections from the feedline, we have to match the impedance of the feedline to that of the transmission line; that is to say, the characteristic impedance of the feedline has to be designed to be 50 Ω. In our case, for sapphire $\epsilon \approx 10$, the feedline works out to be 50 Ω as long as we keep the ratio of w/s at 0.42, according to Eq. 3.5 in previous chapter. However, it is hard to control the exact ratio when we make the resonators using the lithography which indicate that we must compensate for linewidth changes due to over-exposure and over-etching during the lithography and patterning. Taking this into account, we designed our feedline to be $s = 4\mu m$ and $w = 1.5\mu m$ which yields 48.3 Ω. After we pattern our resonator, s is slightly smaller than 4 μm and w is a little bigger than 1.5 μm which yields a characteristic impedance fairy close to 50 Ω.

In terms of the actual resonator part, it isn't necessary to keep it at 50 Ω since it is decoupled from the feedline by its coupling capacitor. In our design, we usually take the ratio w/s of the resonator to be 1/2 which gives 53 Ω.

4.3.2   Center frequency

When designing a mask, we need to choose a center frequency to decide how long the resonator should be, what kind of substrate we should use, etc. As we use a multiplex scheme, there are a few constraints that come with it.

The center frequencies of each resonator along the same feedline have to be separated far enough so that they don't overlap. The frequency separation between the two adjacent resonances should be no smaller than the bandwidth of the resonator.

For two resonators with 20000 Q around 5GHz, the minimum separation would be 0.25MHz according to equation (4.4):

$$\Delta f = \frac{f_r}{Q}. \tag{4.4}$$

In our research, $4 \sim 6$ resonators will be designed in one resonator chip. If we want all the resonators have close by center frequencies, a 200MHz seperation is usually used.

If resonators with different widths are needed for some purpose, there is one more constraint that needs to be considered. The narrowest resonator has the biggest center frequency shift in either temperature dependence or the field cool experiment because of the fractional kinetic inductance. The kinetic inductance will be discussed later. This information compels us to design a narrower resonator responses at a lower frequency so that during the experiment it won't overlap with other resonances due to a significant frequency shift.

The measured center frequency is usually never equal to the designed center frequency. One of the reasons comes from the fabrication process. In lithographic patterning, we have to choose the best dose according to a individual visual choice. When we etch the pattern, the length of the exposure time also affects how accurately the actual pattern matches the designed one. Also our simulation tool SONNET doesn't take kinetic inductance into account. Even so, resonance near the designed center frequency should be expected.

Taking all the factors above into consideration, the center frequency of each resonator can be designed. The desired f_0 and the type of the dielectric constant ϵ determine the total length of the resonator. A wave can propagate at the speed of light on a lossless transmission line in vacuum. However, in reality the dielectric always slows down the propagation speed. For a quarter wavelength resonator, the

total length l should be:

$$l = \frac{c'}{4f_0},\tag{4.5}$$

$$c' = c\sqrt{\frac{2}{1+\epsilon}}\tag{4.6}$$

where c is the speed of the light, c' is the reduced speed, the phase velocity, of a wave in a dielectric and ϵ is the permittivity of the dielectric. For a half wavelength resonator, the total length l works out to be:

$$l = \frac{c'}{2f_0}\tag{4.7}$$

4.3.3   Coupling to external circuitry

In our multiplex design, multiple resonators capacitively couple to one common feed-line as in Figure 4.7 a. The length of the coupling elbow determines the coupling quality factor (Q_c), and this coupling loss measures how much energy leaks into the resonator through the capacitor. A quarter wavelength resonator can be analogical to a quarter wave transmission line resonator consisting of a series combination of a coupling capacitor C_c and quarter wavelength section of transmission line of load impedance Z_l, shunting a feedline. According to Pozar [62] and the thesis from Mazin [5], the Q_c can be calculated as,

$$Q_c = \frac{\pi}{4Z_0 Z_L(\omega_0 C_c)^2}\tag{4.8}$$

Where Z_0 is resonator impedance, Z_L is load impedance, and they are both usually 50Ω in our case. C_c is the coupling capacitance. Meanwhile, from a electromagnetic field simulator, such as SONNET [72], s parameters can be obtained, then by fitting a loop in complex plane, the coupling quality factor can be extracted out. The simulation and fitting will be extensively dicussed later. As in Figure 4.7 b, the elbow coupler is designed to have a $12\mu m$ center strip and $6\mu m$ gap, or as in Figure 4.8, the elbow coupler is a $4\mu m$ center strip and $2\mu m$ gap. We usually use the elbow
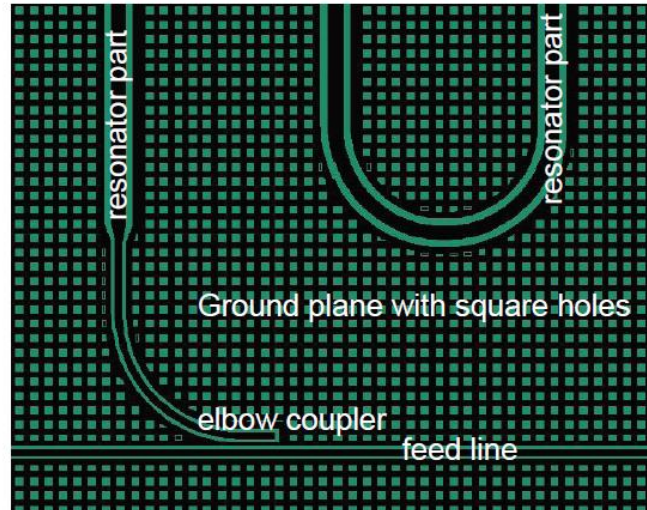
Figure 4.8: Close look of one resonator in Cadence.

configuration as shown in Figure 4.8; somewhere after the elbow a taper is used to vary the width for the remainder of the resonator. There is a fixed $2\mu m$ of metal space between the feedline gap and the coupling elbow gap which maitains the impedance of both the feedline and the resonator.

4.4 Numerical simulations of microwave resonators

After we decide what Q and f_0 should be, we can draw out the resonators according to the equations listed previously. With simulation, we can make sure resonators will resonate at the designed f_0 with the Q that we need before finalizing our pattern. SONNET is a high frequency electromagnetic software. It employs a modified method of moments analysis based on Maxwell's equations [72] according to the physical pattern of the circuit in arbitrary layout and material properties assigned for the metal and dielectrics. It performs a true three dimensional current analysis of our resonator (a planar structure). AWR and Ansoft Designer are also used to do the simulation. Both softwares use the embedded equations exacted from Maxwell's equations to quickly simulate the circuit and give results in a very short time. SONNET takes a

longer time than AWR and Ansoft Designer; however it gives more accurate results
because of the way how it simulates.

it's important to point out that Sonnet does not account for kinetic inductance,
so our actual resonators are always lower in frequency no matter how accurate the
simulation results are.

There is a way to estimate Q_c before cooling down a newly designed chip. S
parameters can be obtained from simulation by Sonnet, by fitting the loop in the
complex plane, we can extracted Q_c out. The fitting is being discussed right after
this section.

When all the design parameters are verified through simulation, a GDSII file is
exported out from SONNET and it can be imported to Cadence directly. Cadence
design system is an electronic design automation software. We use only one of plat-
forms named Virtuoso as a tool to draw our layout. After importing our GDSII file
into Cadence, the final layout of the mask will be produced.

4.5 Extracting resonator parameters from fits to microwave measurements

The measurements we take through network analyzer is a vector measurement of
transmission through feedline, i.e., the S parameters we recorded have magnitude
and phase. In the complex plane, each reasonance forms a loop. The transmission
data can be divided into I and Q axes. I axes are information about real part of the
transmission signal and Q axes are imaginary part of the signal. The total amplitude
of this signal is $\sqrt{I^2 + Q^2}$, and the phase of the signal is $\tan^{-1}(Q/I)$. By fitting this
loop in this complex plane, we can extract the quality factor Q_{fit} and center frequency
f_0 for each resonator. However, there are lots of factors that are difficult to calibrate
out, then they must be accounted for in this fitting.

we use fitting equations as Eq. 4.9

$$
\begin{aligned}
dx &= \frac{x - f_0}{f_0} \\
f &= \frac{2iQdx}{1 + 2iQdx} - \frac{1}{2} + cdx + a[1 - e^{i\nu dx}] \\
f_2 &= (g_I \mathrm{Re}[f] + ig_Q \mathrm{Im}[f])e^{i\theta} + I_c + iq_c
\end{aligned}
\tag{4.9}
$$

to fit our resonator data, following a fitting procedure similar to what is done for
MKID measurements [5]. This least-squares fit of resonance trajectory in a complex
plane can let us obtain fundamental resonator information with fit parameters to
account for gain, offsets, and electrical lengths of cabling. here is the list of ten fitting
parameters:

Table 4.1: List of ten fitting parameters

Q	resonator's quality factor
f_0	resonator's center frequency
a	off resonance amplitude
c	Linear offset of the beginning and end of the resonace curve
θ	Rotation angle of the data in terms of the origin
ν	Off resonance velocity
g_I	Scale factor of the I axes
g_Q	Scale factor of the Q axes
I_c	Center of the resonance circle in the x axes
q_c	Center of the resonance circle in the y axes

It is important to find the starting values for the fitting paramters. For example,
g_I is a scale factor of the I axes, and by looking at the loop in the complex plane,
we can choose the mininum and maximun value of the intersection of the loop with
I axes. For Q_c, we can choose the starting point of 10 time smaller/bigger than the
designed coupling Q, and so on. By doing so, the fitting routin can quickly find the
local minimun and give the fitting results.
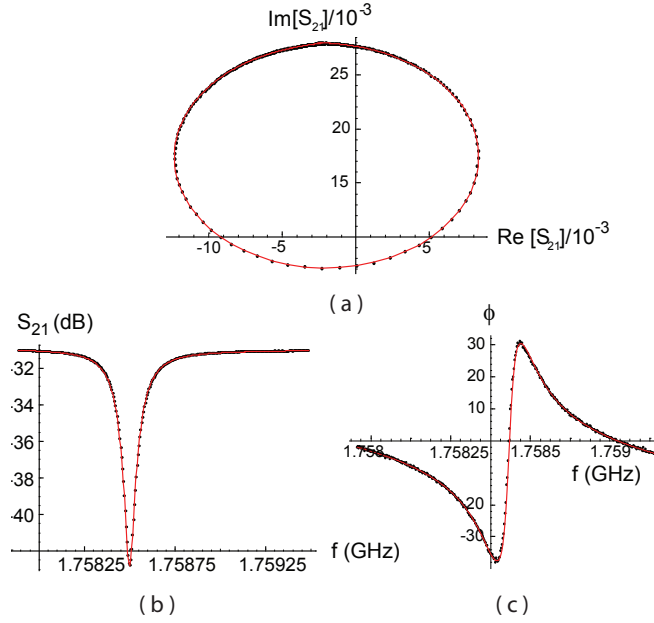
Figure 4.9: An example of the resonance fitting. The black points are actual measured data, and the red line is the result of a fit to the data. Among the ten fitting paramters, Q_{fit} is 10038 and f_0 is 1.75865 GHz

Figure 4.9 is one of the fitting examples. It is a Re resonator at 1.76 GHz cooled in 56.4 μT. Black points are measured data and red lines are results of a fit to the data. The parameters for this fit of the resonator are $Q_{fit} = 10038$, $f_0 = 1.75865$ GHz, a=1611.35, c=-19.84, g_I =0.0207, g_Q =0.0207, I_c =-0.001496, q_c =0.017316, ν =0.1622 and θ =1.690

4.5.1 Fitting routine to determine quality factor

Q_i is generally used in a lot of plots in this thesis. After Q_{fit} is obtained, measured $1/Q_c$ instead of designed $1/Q_c$ has to be subtracted out of $1/Q_{fit}$, in order to get $1/Q_i$. There are two ways to get intrinsic quality factor Q_i. One way is from measurement of temperature dependence. In TD, kinetic inductance fraction α can be extracted out according to Mattis-Bardeen fit. From equation 5.13, putting α back to $\frac{\alpha}{3}\frac{\sigma_1(T)}{\sigma_2(T)}$, Q_i^{-1} can be obtained. There is a second way to get Q_i. According to the equations
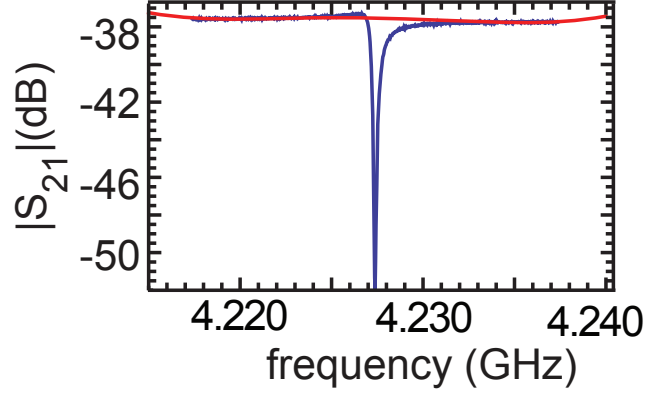
Figure 4.10: Fittings for base line of 18 μm resonator at 285mK which yields Q_c and Q_i to be
11564 and 51373, respectively.

4.10, both Q_c and Q_i can be obtained at the some time.

$$\frac{1}{Q_{fit}} = \frac{1}{Q_i} + \frac{1}{Q_c}$$
$$S_{21}^{min} = \frac{Q_c}{Q_i + Q_c} \tag{4.10}$$

S_{21}^{min} is the magnitude of transmission at the dip (the minimum of the resonator
transmission). In order to get the S_{21}^{min}, the resonance data S_{21} with a really big
span, such as 10MHz or even 20MHz, was taken. From fitting the data as it was
mentioned in chapter 4, we can get all the ten fitting parameters. By using the Q=0
and the rest nine fitting parameters, the transmission line without a dip(base line)
can be drawn. Then S_{21}^{min} can be calculated by subtracting the magnitude of S_{21} from
the base line.

Figure 4.10 shows an example of the fitting for base line of 18 μm resonator at
285mK which yields Q_c and Q_i to be 11564 and 51373, respectively.

Recently, we have developed a new fitting routine according to Ref. [73] to get
Q_i, Q_c and $Q_f it$ simultaneously by fitting the trajectory in complex plane. The
comparison has been done to the old and new fitting routine, and both ways yield
the similar results.

4.6 Fabrication

Throughout this thesis, Al and Re were two superconducting metals used to make resonators. Because the T_c of both materials are suitable for us to cool down with our ^{3}He refrigerator. The Re films were 50 nm thick and were deposited by electron-beam evaporation onto an a-plane sapphire at a temperature of 850 C. The Re film and Re resonators in this thesis were made by M. Neeley in University of California, Santa Barbara. While, the Al films were deposited in our lab by electron-beam evaporator which is dedicated to make Al thin films, hence our Al film should not be contaminated by other metals. The thickness of the Al film was 150 nm. The rest of the fabrication of the Al resonators took place at the Cornell NanoScale Science & Technology Facility (CNF). Both types of films were patterned photolithographically, followed by a reactive ion etch.

4.6.1 Lithography

There are several steps before we really put our pattern on a wafer. First the solvent isopropyl is used to clean the surface of the wafer, then spinning is used to get resist onto the substrate with the required uniform thickness. In our case, we spin 'SPR955 0.9' with a speed of 3000 rpm on Al thin film for 60 seconds which gives us 0.9 μm photoresist layer. In order to drive the solvent from the resist, we bake the wafer with coating resist at $90^0 C$ for 60 second; on the other hand, we shoudn't bake it too long because it will destroy the photoactive compound and reduce its sensitivity.

Autostep 200 is a repeat exposure tool for doing lithography that requires high resolution and/or critical alignment. The stepper in CNF is employed to expose our wafer through a mask we made. The exposure time is ~ 0.12 seconds, but it is better to expose the wafer after a dose test. The dose test is that an array of the same patterns get exposed by different exposure time with a fixed step size, then with the help of microscope, we can pick the optimum dose by comparing how close the

exposed pattern to the mask.

I have to mention that the mask is what we design and draw in Cadence and is made by Heidelberg Mask Writer DWL2000.

After the wafer is exposed, post baking at 115^0C for 60s is necessary. It hardens the resist and reduce standing waves in regular positive resist exposed on the steppers which affects the resist profile.

Before we develop our wafer, it is a good idea to check the pattern with a microscope. If the pattern is under or over exposed, we can still go back to the first step to remove the photoresist to start everything over. Otherwise, we can continue to develop the wafer.

We stir in 300MIF (Tetramethylammonium hydroxide) for 60 seconds then rinse in deionized water; this is how we develop our wafer. Most of the developers etch Al, including 300MIF. In fact, later in our resonator fabrication, we have tried several times to directly use Aluminum etch type A (a combination of Phosphoric acid, Acetic acid and Nitric acid) to wet etch our Al resonators.

4.6.2   Etching

The PT720-740 etcher is a dual chamber system. We use the left 740 side to etch Al wafers or pieces which can be glued onto a sapphire wafer carrier. A reactive ion etch takes place in a combination of BCl_3, Cl_2, and CH_4 (Al) or SF_6 and Ar (Re). Under vacuum or even low pressure, the chemically reactive plasma is generated by an electromagnetic field. All those high energy ions from the plasma attack the wafer, react with it and finally remove some material which is not being protected by resist.

Before we etch the real wafer, we always condition our chamber for 10 minutes by using the same recipe we use to etch our real wafer. By doing so, we can clean the chamber to avoid any contamination left in the chamber by other users.

4.6.3 Dicing

Noticing that sapphire wafer is a kind of crystal, it is very brittle and very hard to cut by hand. A dicing saw is necessary to cut our wafer, as some of our resonators are patterned on such sapphire wafers. In CNF, there is a KS 7100 dicing saw. Extra precausions are required to cut the sapphire wafer. We used a low cutting speed (0.5mm/s) and small cutting depth (120 μm each cut) to avoid breaking blades. As the thickness of our wafer is around $330\mu m$, we usually need to cut our wafer two times in order to break it easily.

4.7 Packaging

After all the fabrication is done, we have to pick one good chip to do our measurements. The chips with the desired pattern are soaked in Acetone for about one hour to remove the photoresist. When the resist is removed from the chips, isopropyl is used to rinse rest residue off; then we use N2 gas to dry them.

With the help of the microscope, chips with flaws from fabrication will be eliminated from all these candidates. The criteria of choosing good chips are these: whether the feedline and resonators are continuous and the dimension of the feedline, gap and resonators are close to what we designed. We can also use atomic force microscopy (AFM) to check the etching depth, width and the roughness of the resonators.

Figure 4.11 contains the front and back views of a customized PCBoard with a chip wire bonded in the middle. This PCBoard is designed by our collaborators at UCSB. It has three layers in which the top and bottom layers are grounded, and these two grounded planes are connected by multiple small holes in the PCBoard. The middle layer contains six possible ports which are used for transmitting signals. The flat center pin of a SMA is soldered to a small rectangular copper trace which is connected to the signal line embedded in the middle layer. These signal lines from
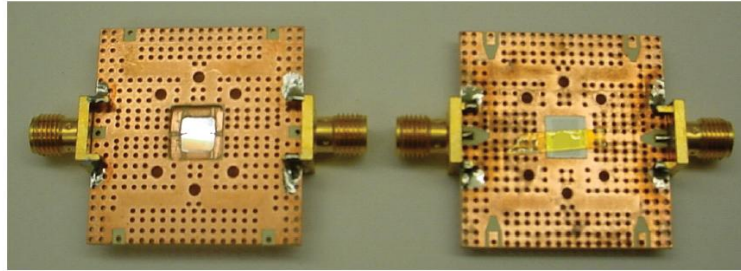
Figure 4.11: The left side is the front side of a customized PCBoard with a chip wire bonded in the middle and the right one is the back side.

(a) (b) (c)
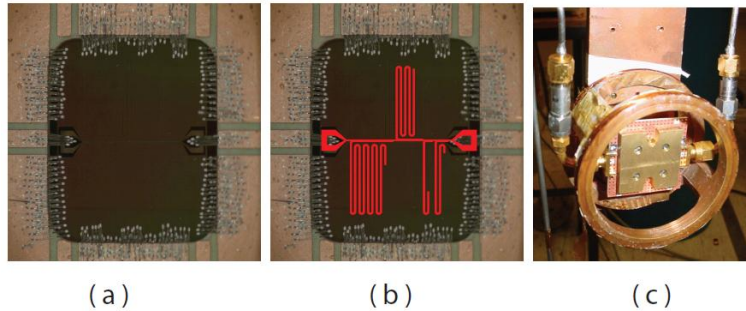
Figure 4.12: (a) Zoomed-in view to show the wire bonds between the PCBoard and a chip. (b) Zoomed-in view with a layout of resoantor. (c) PCBoard with a chip in a brass holder and mounted in the middle of Helmholtz coil on the 3He insert.

the PCBoard are then connected to our feedline from chip by several Al wires as in the Figure 4.12(a) and (b). In Figure 4.12(b), a schematic of a typical resonator has placed where resonators thenselves sit. We can see that the feedline is aligned to the signal copper trace on the PCBoard. After the chip is placed well to the PCBoard, next step is wire bond them. We usually put approximately ten wire bonds for the feedline to reduce the stray inductance contribution from the wirebonds. Besides the feedline, more than twenty wire bonds are made to connect the ground plane of the chip to the ground of the PCBoard each side. All these wire bonds have to stay away from the resonator parts. Once the chip is wire bonded, it will be put in a brass holder to mount on the ^{3}He insert to cool down as in Figure 4.12(c).

Chapter 5

Characterization of superconducting parameters from resonator measurements

In this chapter, the superconducting parameters, such as residual resistivity ratio (RRR) and T_c, to characterize the quality of the Al film are discussed. Later measurements of temperature dependence for resonators in zero magnetic field are presented, another superconducting parameter, kinetic inductance fraction is introduced in this part.

The Al films, we will discuss here, were 150 nm thick and were electron-beam evaporated onto c-plane sapphire that was not heated. This Al film was patterned photolithographically followed by a reactive ion etch in a combination of BCl_3, Cl_2, and CH_4 (Al) or SF_6 and Ar (Re). Please refer to chapter 4 for the fabrication details.

5.1   Residual resistivity ratio (RRR) measurements

The impurity of metals can be indicated by residual resistivity ratio (RRR). The RRR of a metal is expressed as the ratio of the electrical resistivity at the room temperature

($\sim$293K) to the resistivity at low temperature ($\sim$4.2K):

$$RRR = \frac{\rho_{293K}}{\rho_{4.2K}} \approx \frac{R_{293K}}{R_{4.2K}}. \tag{5.1}$$

In our case, this low temperature is just above the critical temperature T_c 1.15K or 1.7K for Al or Re, respectively. Resistance of a metal R and the resistivity ρ can be related as $R = \rho(l/s)$. Here l is the length and s is the cross section of the metal. Because the change of the l/s with the temperature from 293K to 4.2K is negligible, the ratio of $R_{293K}/R_{4.2K}$ is approximately equal to $\rho_{293K}/\rho_{4.2K}$ as shown in equation 5.1. The fact RRR is measured through the ratio of $R_{293K}/R_{4.2K}$, instead of $\rho_{293K}/\rho_{4.2K}$, is because R is the experimentally measurable quantity, while calculating ρ requires detailed knowledge of the geometry.

Total resistivity (ρ_{total}) can be expressed as [74]:

$$\rho_{total} = \rho(T) + \rho_0. \tag{5.2}$$

There is a temperature-dependent portion that is dominated by phonon scattering and a temperature-independent part that is related to the defect in crystal structure like grain boundaries, dislocations and impurity [74]. Temperature-dependent portion from the scattering, which is due to thermal vibration prevailing in the lattice, decreases as the temperature is reduced.

In our experiment, we measured R of Al at $\sim$2K. The resistivity at 2K is almost the same as that at 4.2K, since the temperature is already low enough. The measurement is based on their voltage-current(VI) curves by using four point method, as Figure 5.1 shows, which involves the connections of two potential and two current leads to our sample. The advantage of four wire measurement is the separated current and voltage electrodes eliminate current flowing in the sense wire, so it is a more accurate measurement than traditional two wire measurement. At room temperature, the Al film deposited in our lab had the resistance 180.1 Ω. According to $R = \rho(l/s)$, resistivity was $3.4 \times 10^{-8}\Omega \cdot m$ with the length, width and thickness of the feedline to be 2970 μm, 4 μm and 150 nm, respectively. At 2K, resistance(resistivity) was
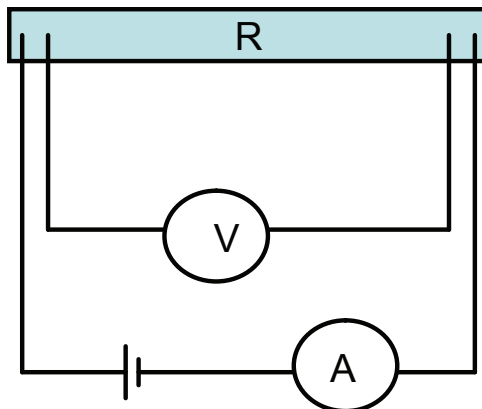
Figure 5.1: Configuration of four wire measurement.

found to be 18 Ω ($3.3 \times 10^{-9} \Omega \cdot m$). Hence, according to equation 5.1, RRR was ~10. We did the same measurements to several Al films and found out the RRR of the Al film we deposited on sapphire in our lab had a range of 10 ~ 20, depending on the condition of the chamber of the ebeam evaporator, purity of the Al bath.... The RRR of the Re film was 11.

5.2 T_c measurements

Tc is the critical temperature when the film becomes superconducting. It is usually measured for several purposes. First of all, the T_c of a thin film is different from the bulk value due to the oxygen that got incorporated into the film during the deposition, so it would be good if we measure the T_c for every thin films. Secondly, if we know the T_c of the film before the field cool experiment, we can heat sufficiently so that the entire resonator enters the normal state, at which point the magnetic field distribution throughout the film will become uniform. Thirdly, the measurement of T_c with different magnetic fields allows us compute one of the length scales that characterizes the superconductor, the effective coherence length ξ_{eff}.
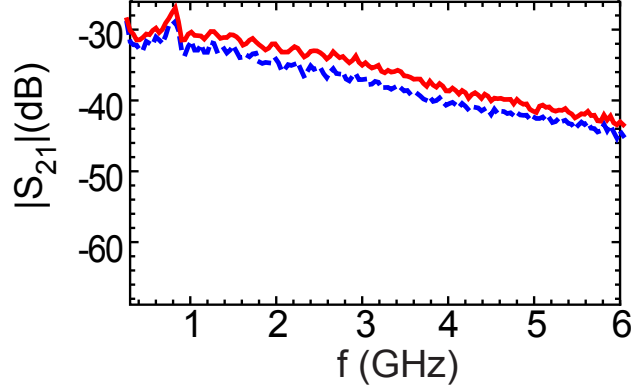
Figure 5.2: Base lines at two different temperatures, blue dotted line is the base line at 1.59K and red line is the the base line at 0.97K.

The following is the way how we measure T_c. This method works only to the specific case of resonators that are C-coupled to a feedline as in our particular geometry (quarter wavelength resonators), but it wouldn't apply for through-measurements of a 1/2-wave resonator. In an ideal case for our 1/4-wave resonators, the superconducting transmission line would pass through all the power we excited to the other side and lose no energy at dc, however, at microwave frequencies, there are different kinds of microwave losses, so the magnitude of S_{21} wouldn't be 0 dB at all frequencies. The level of $S_{21}(f)$ is consistent with the measured losses for all of the individual components, as described in Chapter 4. Figure 5.2 is the baseline measurement from 300KHz to 6GHz. In this Figure, the red base line (labeled as a solid line) was measured at 1.59K, we also took the base line at 1.5K, 1.4K, etc., but those lines overlapped with the red one. When the temperature is cooled down below T_c, the feedline becomes superconductor at T_c, then the level of S_{21} increases at this temperature. The overall shift of the level is related to the change in the loss through the feedline as T goes through Tc. In our measurement, the blue line (labeled as a dotted line) was measured at 0.97K. The traces of S_{21} way below T_c are on top of each other. In our T_c measurement, we decrease temperature of test resonators in a very slow rate to make sure that the T values on the thermometer are representative of the T of the sample.
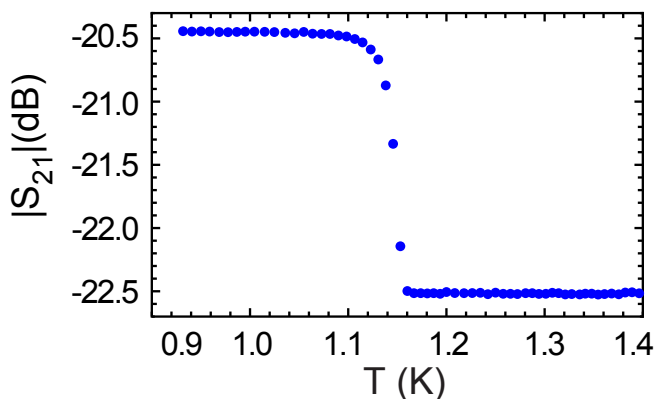
Figure 5.3: Tc vs. temperature without field for an Al film at 1.5GHz which gives T_c 1.15K
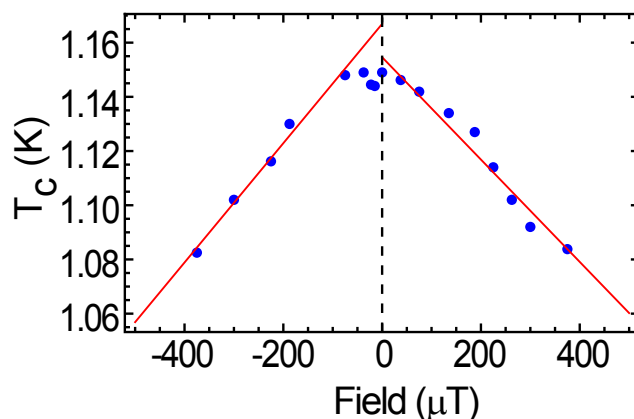
Figure 5.4: T_c as measured with the microwave transmission procedure described in the text vs. magnetic field for an Al resonator, and the red straight lines are the linear fits slope (-0.00022$K/\mu T$ at positive side and 0.00021$K/\mu T$ at negative side)

At the same time, the S_{21} parameters are frequently measured every 30 seconds. A set of S_{21} at different temperatures at a fixed frequency can be obtained after a group of baselines are measured. The S_{21} vs. Temperature is plotted in Figure 5.3 for one Al thin film; there is a steep S_{21} change at 1.15K which indicates the critical temperature. Typically, it takes around one hour to finish one T_c measurement for a fixed field.

By repeating this T_c measurements with different fields, a graph of T_c vs. field can be plotted out as Figure 5.4. The T_c is almost symmetric at the positive and negative

field. There is, however, the slight offset between the two polarities of field might be caused during the cooling process. Because when the temperature of ^{3}He pot of the ^{3}He refrigerator is higher than $\sim$ 700mK, we manipulate the temperature of sorption pump to indirectly control the temperature of ^{3}He pot; this means that we can't stay at certain temperature for long enough to make sure everything attached to ^{3}He pot are at equilbrium state. Hence, the temperatures of the test chip probably are slight off from the thermalmeter. Linear fits for both sides are included in Figure 5.4 and the fit at positive side give a slope of 0.00022 $K/\mu T$ while -0.00021 $K/\mu T$ is obtained at negative side.

According to the dirty-limit expressions equations 2.8 and 2.10, we can calculate the effective coherence length since the magnitude of $\frac{dH_{c2}}{dT}\mid_{Tc}$ and T_c are known. For this Al film we measured, the ξ_{eff} to be around 230nm. Furthermore, we can derive the mean free path by Eq. 2.5 as we know T_c and ξ_{eff} from experiments.

5.3 Measurements of temperature dependence for resonators in zero magnetic field

5.3.1 Mattis-Bardeen theory of high-frequency response of superconductors

From standard electromagnetic theory, a normal metal with conductivity σ and permeability μ will screen an electromagnetic wave of frequency ω over a length given by the skin depth δ. The equation of skin depth 5.3 is a function of three variables, frequency (ω), conductivity (σ), and relative permeability (μ):

$$\delta = \sqrt{\frac{2}{\omega\mu\sigma}}.\tag{5.3}$$

For a local relationship $\vec{j}(\vec{r}) = \sigma\vec{E}(\vec{r})$ and the skin depth, the electric field $\vec{E}$ remains constant within a radius l around some point $\vec{r}$, and l is much smaller than the

skin depth. Because the skin depth decreases at higher frequencies and l increases at lower temperature, a non-local relationsip between $\vec{j}$ and $\vec{E}$ occurs [75]. In 1958, Mattis and Bardeen (MB) [65], and independently Abrikosov, Gor'kov, and Khalatnikov [76], derived a general theory of the anomalous skin effect in superconducting metals based on the BCS model of superconductors. Generally the MB formula can be expressed in terms of the Fourier components of the current density $\vec{j}(q)$ and the vector potential $\vec{A}(q)$ by defining K(q) as [65]:

$$\vec{j}(q) = -K(q)\vec{A}(q). \tag{5.4}$$

Where

$$K(q) = \frac{3}{4\pi^2 \hbar \nu_0 \lambda_L^2(0)} \int \frac{\vec{R}\vec{R}\vec{A}(\vec{r'})I(\omega, R, T)e^{-R/l}}{R^4} d\vec{r'}, \tag{5.5}$$

$$I(\omega, R, T) = -i\pi \int_{\Delta-h\omega}^{\Delta} [1 - 2f(E + h\omega)][g(E)\cos(\alpha\Delta_2) - i\sin(\alpha\Delta_2)]e^{i\alpha\Delta_1}dE$$
$$-i\pi \int_{\Delta}^{\infty} [1 - 2f(E + h\omega)][g(E)\cos(\alpha\Delta_2) - i\sin(\alpha\Delta_2)]e^{i\alpha\Delta_1}dE$$
$$+i\pi \int_{\Delta}^{\infty} [1 - 2f(E)][g(E)\cos(\alpha\Delta_1) - i\sin(\alpha\Delta_1)]e^{-i\alpha\Delta_2}dE \tag{5.6}$$

$$\Delta_1 = (E^2 - \Delta^2)^{1/2}, \Delta_2 = [(E - \hbar\omega)^2 - \Delta^2]^{1/2},$$
$$\alpha = R/(\hbar\nu_0), g(E) = (E^2 + \Delta^2 + \hbar\omega E)/(\Delta_1\Delta_2) \tag{5.7}$$

with $\vec{R}=\vec{r'}-\vec{r}$. The non-local effects are included in the $I(\omega, R, T)$ and in the exponential function $e^{-R/l}$. The kernel equation $K(q)$ is also mentioned by Tinkham [34]. $\lambda_L(0)$ is the London penetration depth at T = 0 K, $f(E)$ is the Fermi function Eq. 5.8, and k_B is the Boltzmann constant.

$$f(E) = \frac{1}{1 + exp(E/k_BT)} \tag{5.8}$$

The relationship between $\vec{j}$ and $\vec{A}$ is relatively simple in two limits. For $l << \xi_0$ (the dirty limit and the ξ_0 can be thought as the minimum size of a Cooper pair as dictated

by the Heisenburg uncertainty priciple [77]), $I(\omega, R, T)$ can be assumed as a constant
in the range of R. At the extreme anomalous limit ($\lambda << \xi_0$), $I(\omega, R, T)$ varies slowly
in space with respect to the other part in the kernel equation, and it can be taken as
a constant too. In my experiments, we usually use the extreme anomalous limit.

5.3.1.1   Complex conductivity and surface impedance

The Mattis-Bardeen expression for the current density Eq.5.4 can be reduced to
surface impedance in a simplified form with certain approximation. According to
Glover and Tinkham [78], a complex conductivity ($\sigma = \sigma_1 - i\sigma_2$)can be introduced
as:

$$\frac{K_\infty}{K_{n\infty}} = \frac{\sigma_1 - i\sigma_2}{\sigma_n} \tag{5.9}$$

here σ_n is the normal conductivity at a given frequency.

The equations for the complex conductivity in the superconducting state normal-
ized to the normal conductivity was derived by Mattis and Bardeen in Ref. [65].
When there are quasiparticles due to the temperature change, the normalized real
and imaginary conductivity can be rewritten according to Gao [77, 79] as following:

$$\frac{\sigma_1(T)}{\sigma_n} = \frac{4\Delta_0}{\hbar\omega}e^{-\frac{\Delta_0}{kT}}\sinh(\xi)K_0(\xi) \tag{5.10}$$

$$\frac{\sigma_2(T)}{\sigma_n} = \frac{\pi\Delta_0}{\hbar\omega}[1 - \sqrt{\frac{2\pi kT}{\Delta_0}}e^{-\frac{\Delta_0}{kT}} - 2e^{-\frac{\Delta_0}{kT}}e^{-\xi}I_0(\xi)] \tag{5.11}$$

where I_n and K_n are the nth order modified Bessel function of the first and second
kind, respectively. Δ_0 and ξ are defined in chapter 2. At the extreme anomalous
limit, the temperature dependence of f_0 and Q_{fit} can be rewritte as [5]:

$$\frac{\delta f_0}{f_0} = \frac{-\alpha\delta\sigma_2(T)}{6\sigma_2(0)} \tag{5.12}$$

$$\delta\left(\frac{1}{Q_{fit}}\right) = \frac{\alpha\sigma_1(T)}{3\sigma_2(T)} \tag{5.13}$$

here α is the fractional kinetic inductance:

$$\alpha = \frac{L_{kin}}{L_{total}}. \tag{5.14}$$

These equations are used in my research to fit both frequency shift and loss due to temperature dependence. From this fitting, either the energy gap or the kinetic inductance fraction can be derived.

There is another way to describe the ac response of a superconductor. We have mentioned in chapter 2; in the case of superconductors, currents decay exponentially in the surface of the superconductor with a characteristic length scale λ. This effect has lead to the use of the notion of surface impedance, Z_s. The Z_s can be written in terms of a dissipative component (resistance) and a conservative component (reactance):

$$Z_s = R_s + jX_s$$
$$= R + i\omega\mu_0\lambda \tag{5.15}$$

where μ_0 is the permeability of free space $4\pi \times 10^{-7}$ H/m. The surface resistance R_s is associated with the conductor loss and the surface reactance X_s is directly connected to the superconducting penetration depth as equation 5.15 shown. The ratio of the real to imaginary impedance is:

$$\frac{\mathrm{Re}(Z_s)}{\mathrm{Im}(Z_s)} = \gamma\frac{\sigma_1}{\sigma_2} \tag{5.16}$$

with γ to be 1, 1/2 or 1/3 for thin film limit, local (dirty) limit or extreme anomalous limit, respectively.

The temperature dependence of the surface impedance predicts how the resonance frequency f_0 and quality factor Q_{fit} of a superconducting resonator vary with the temperature. The relationship between f_0, Q_{fit} and X_s, R_s are [77]:

$$\frac{\delta f_0}{f_0} = \frac{f_0(T) - f_0(0)}{f_0(0)} = -\frac{\alpha}{2}\frac{X_s(T) - X_s(0)}{X_s(0)} = -\frac{\alpha}{2}\frac{\delta\lambda_{eff}}{\lambda_{eff}} \tag{5.17}$$

$$\delta\left(\frac{1}{Q_r}\right) = \frac{1}{Q_{fit}(T)} - \frac{1}{Q_{fit}(0)} = \alpha\frac{R_s(T) - R_s(0)}{X_s(0)} \tag{5.18}$$

The penetration depth is defined in chapter 2, the λ_{eff} is:

$$\lambda_{eff}(l, T) = \lambda(T)\sqrt{1 + \epsilon_0/l} \tag{5.19}$$

The change of reactance due to the temperature results in the frequency shift, meanwhile the resistance change causes loss.

5.3.2 Introduction to kinetic inductance fraction

In superconducting resonator, kinetic inductance, which arises because of the inertia mass of the moving cooper pairs, plays an important role especially when the superconducting film is thin.

When a transmission line is made of superconducting material, part of the external magnetic field penetrates into the superconductors with the finite penetration depth. The current flowing in this penetrated layer carries kinetic energy of the Cooper pairs and adds to the total inductance. The penetration depth changes with temperature, so this kinetic inductance L_{kin} varies with temperature and the density of the quasiparticles. The field outside of the superconductor depends on the geometry of our superconductor which is independent on the temperature, and the inductance caused by this field is geometrical inductance L_m. The total inductance can be written as:

$$L_{total} = L_m + L_{kin}. \tag{5.20}$$

In equation 5.19, α measures how large L_{kin} is relative to the total inductance. The model of treating L_{kin} as a function of temperature and thickness of the film has been employed in earlier works [80, 81].

In order to calculate L_{kin}, we can start from kinetic energy density which can be written as:

$$E_{kin} = n_s \left(\frac{1}{2} m \nu_s^2 \right) \tag{5.21}$$

where n_s is the electron pair density, m is the Coopair mass, and ν_s is the pair velocity. The current density is $J_s = n_s q \nu_s$ with q being the pair charge. Combining 5.21 and the expression of λ from Eq. 2.3, the kinetic energy density can be rewritten as:

$$E_{kin} = \frac{\mu_0 \lambda^2 J_s^2}{2} \tag{5.22}$$

The total energy stroed in the magnetic field then can be expressed as:

$$E_{total} = \frac{1}{2\mu_0} \int \left[B^2 + \mu_0^2 \lambda^2 J_s^2 \right] dV \tag{5.23}$$

where $B^2/2\mu_0$ is the magnetic field energy density [82]. The E_{total} has two parts: (1) the integral of the magnetic field density across the cross section of the transmission line including the space between signal strip and gound plane and the place where field penetrates into; (2) the integral of the kinetic energy density due to the motion of the electrions in the superconducting cross section. On the other hand, the E_{total} is equal to $LI^2/2$ with L being the total inductance per unit length of the line. In Ref. [82, 83], the inductance per unit length of microstrip geometry has been calculated.

Meservey and Tedrow [84] calculated L_{kin} of a superconducting strip in 1969. When the strip has a rectangular cross section, L_{kin} is written as:

$$L_{kin} = \frac{\mu_0}{\pi^2} (\lambda/w) \ln(4w/d) \frac{\sinh(d/\lambda)}{\cosh(d/\lambda) - 1} \tag{5.24}$$

w and d are width and thickness of the cross section of the strip line. In the thick and thin film limits, the relationship between L_{kin} and λ is expressed in a much simpler form; $L_{kin} \propto \lambda$ for d $>>$ λ and $L_{kin} \propto \lambda^2$ for d $<<$ λ. The general expressions at these two limits are:

$$\begin{cases} d >> \lambda, & L_{kin} = \frac{\mu_0 l \lambda}{4w} \frac{2}{\pi^2} \ln \frac{4w}{d} \\ d << \lambda & L_{kin} = \frac{\mu_0 l \lambda^2}{4wd} \frac{2}{\pi^2} \ln \frac{4w}{d}. \end{cases}$$

Up to now, Coplanar Waveguid (CPW) has attracted a lot of attention, hence there are several reference [81, 85, 86] discussed L_{kin} for coplanar waveguide resonators.

Watanable *et al.* [87] used a conformal mapping technique to calculate the analytical expression for the kinetic inductance of the superconducting CPW. The NbN CPW resonators were fabricated to carry out the temperature dependence of resonant frequency. A good agreement were found between the expression and the experimental results, specially in the case of a film thickness smaller than the penetration depth
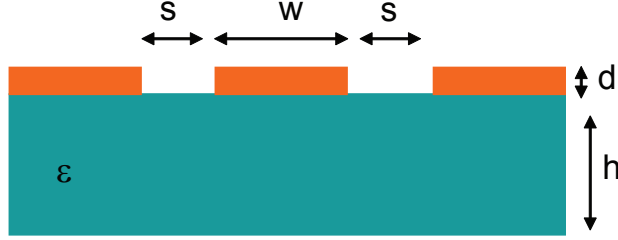
Figure 5.5: Configuration of a coplanar waveguide with labels for paper from Watanabe *et al.*[87]

$(d << \lambda)$ which is consistent with the Ref. [84]. The expression for two kinds of inductance are:

$$L_m = \frac{\mu_0}{4} \frac{K(k')}{K(k)} \tag{5.25}$$

$$L_{kin} = \mu_0 \frac{\lambda^2}{dw} g(s, w, d) \tag{5.26}$$

$$g(s, w, d) = \frac{1}{2k^2 K(k)^2} \times$$
$$\left(-\ln(\frac{d}{4w}) - \frac{w}{w+2s} \ln \frac{d}{4(w+2s)} + \frac{2(w+s)}{w+2s} \ln \frac{s}{w+s} \right) \tag{5.27}$$

where K(k) is the complete elliptic integral of the first kind with the modulus:

$$k = \frac{w}{w+2s} \tag{5.28}$$

$$k' = \sqrt{1+k^2} \tag{5.29}$$

d is the film thickness, w is the width of the center strip and s is the gap between center strip and the ground plane as indicated in Figure 5.5. $g(s, w, d)$ is a geometrical factor. Eq. 5.27 of L_{kin} shows that L_{kin} increases with the decrease of d or s.

Later, Inomata *et al.* [86] investigated film thickness dependence and temperature dependence of resonant frequency with series of Nb $\lambda/2$ CPW resonators at low temperature range of 0.02-5 K. Their experimental results can be explained by taking into account the L_{kin} of the CPW center conductor which was calculated in Ref. [87].

In Gao's thesis, the procedure for deriving L_{kin} for a specific CPW is listed. Tests are carried out to calculate α [77]. For a CPW geometry with small α, the temperature

dependence of the resonant frequency and quality factor, which can be expressed as equation 5.18, is used to determine the value of α. Al resonators with two kinds of thickness, 200nm and 20nm, are fabricated on a silicon substrate which corresponding to the two different cases, the thickness is larger than the effective penetration depth λ_{eff} and the thickness is smaller than λ_{eff}. The experimental and theoretical results of α show good agreement.

After this section, the experiment on temperature dependence of center frequency and quality factor of Al resonators with 150nm thickness are presented. Using the same fitting function Eq. 5.18 as Mazin and Gao's thesis [5, 77], we extracted the α out.

5.3.3 Temperature dependence of Al resonators

As I mentioned in the previous section, temperature dependence data can give us the superconducting parameters of energy gap or kinetic inductance fraction. We can fit the data of temperature dependence, which was described in chapter 4, to get the resonator quality factor Q and center frequency f_0, then the Mattis-Bardeen theory can be used to fit the data of Q and f_0 vs. temperature to derive the kinetic inductance fraction α, given the superconducting energy gap to be $\Delta = 1.76k_BT_c$ [34].

The data we present here are from the 200nm thick Al resonator on Sapphire with the layout as the Figure 6.13 shows. In this design, we have four resonators with different widths of center conductor 4, 8, 12 and 20 μm. The designed frequencies are 3.9, 4.2, 4.6 and 5.0GHz. They all have the same capacitive coupling and are designed to have a similar coupling quality factor of $\sim$15000. In the temperature dependence, we observed strong center frequency shift and loss change. Figure 5.7 covers the temperature range from 0.31 mK up to 0.553 mK for the 12 μm wide resonator. When the temperature is lowered, the density of the thermal quasiparticles is decreased which results in the change of kinetic inductance. According to equations
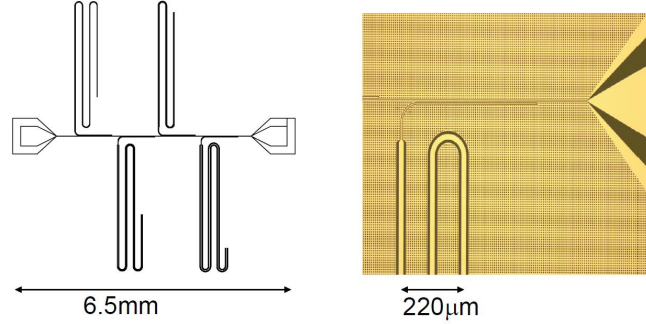
Figure 5.6: (a)The layout of four resonators with different widths of 4, 8, 12 and 20 μm. The designed frequencies are 3.9, 4.2, 4.6 and 5.0GHz which are different from the measured frequencies due to the existence of L_{kin} in measurement. (b) zoomed in image of partial chip under microscope
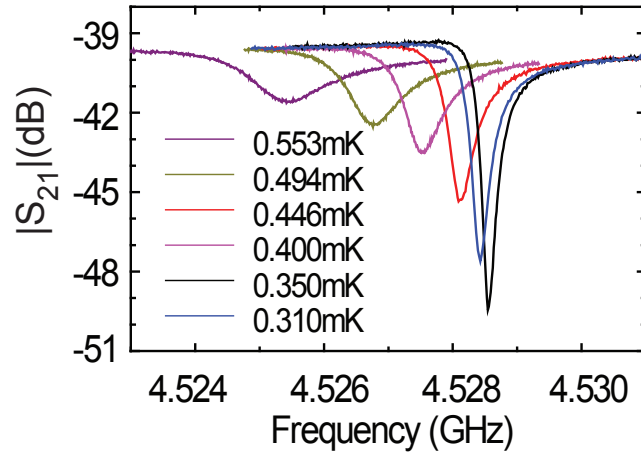
Figure 5.7: Magnitude of S_{21} at a temperature range from 0.31K to 0.553K for a resonator near 4.52GHz

5.13, both f_0 and the loss due to quasiparticles change with temperature. After fitting the resonances for all four resonances, we get f_0 and a fitting Q_{fit} for every dip. $\Delta(1/Qfit)$ and $\delta f/f_0$ vs. temperature from Eqs. 5.31 are plotted out in Figure 5.8.

$$\Delta(\frac{1}{Q_{fit}}) = \frac{1}{Q_{fit}(T)} - \frac{1}{Q_{fit}(T_0)} \tag{5.30}$$

$$\frac{\delta f}{f_0} = \frac{f_0(T) - f_0(T_0)}{f_0(T_0)} \tag{5.31}$$

T_0 is the base temperature which was 310mK in this measurement. The red line
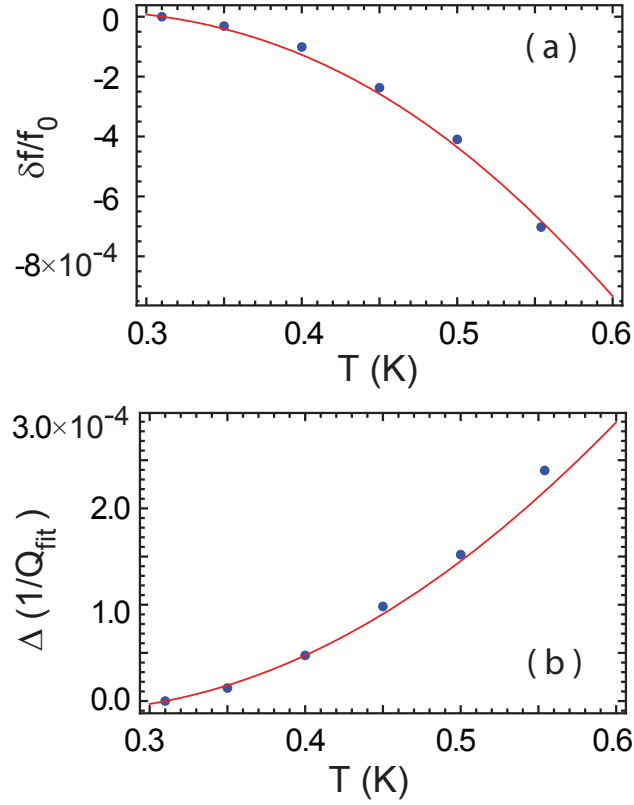
Figure 5.8: (a) The temperature dependence of frequency shift (b) $\Delta(1/Q_{fit})$ vs. temperature. The blue dots in both figures are raw data from measurements and the red line are fits according to Mattis Bardeen theory.
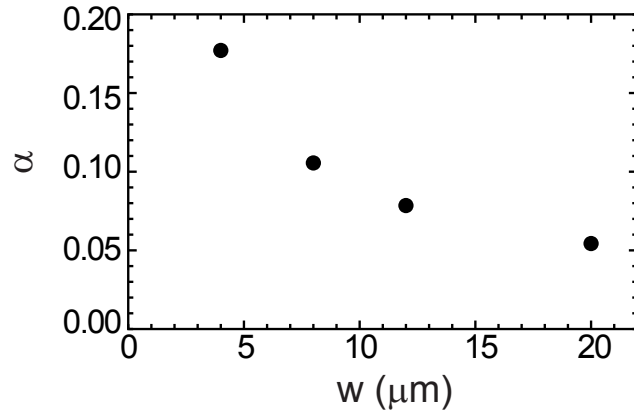
Figure 5.9: α for different width resonators

in Figure 5.8 is the fitting from Mattis-Bardeen theory according to Eq. 5.13, and it gives α of each resonance for the fixed energy gap at exterme anomalous limit. Because the T_c is measured to be 1.15K, Δ is fixed at 0.18meV. The fitting results α are plotted out in terms of the width in Figure 5.9 which indicates the 4 μm resonator has the biggest kinetic inductance fraction.

Chapter 6

Microwave response of vortices in superconducting thin films of Re and Al

6.1 Motivation

In the previous chapter, we have discussed the characterization of superconducting parameters from resonator measurements, such as T_c, RRR measurements and temperature dependence measurements. Here we will try to extract some useful informations out of field cool experiments. As we discussed in section 3.3, the ability of fabricating low loss resonator plays a important role in the design of superconducting microwave devices. In this chapter, we will show that the dissipation due to vortices trapped in the superconducting traces can result in substantial reductions in the quality factor of superconducting resonators. Thus understanding this dissipation mechanism is important for the design any these type circuits.

The section 2.3 has shown that some previous work on the microwave response of vortices in superconductors has primarily involved large magnetic fields, at least several orders of magnitude larger than the Earth's field. On the other hand, su-
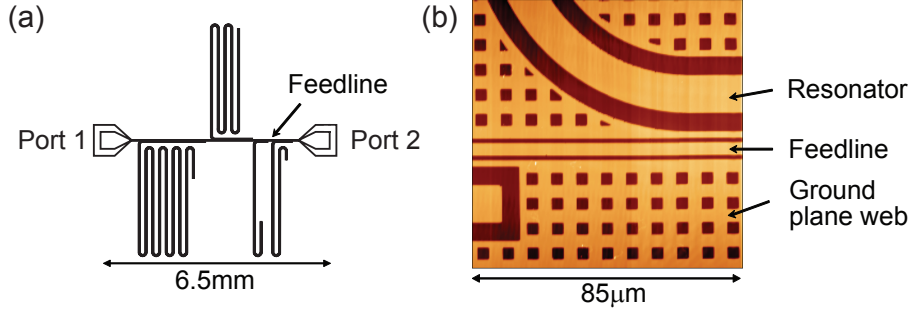
Figure 6.1: (a) Chip layout showing common feedline and four resonators. (b) Atomic Force Microscope (AFM) image of portion of Al chip. (c) Schematic of measurement setup, including cold attenuators with values listed in dB.

perconducting resonant circuits for qubits and detectors are typically operated in relatively small magnetic fields, of the order of 100 μT or less and are fabricated from low-T_c thin films that are often type-I superconductors in the bulk.

In this chapter, we report on measurements probing the magnetic field and frequency dependence of the microwave response of a small number of vortices using resonators fabricated from thin films of rhenium and aluminum – common materials used in superconducting resonant circuits for qubits and detectors. Related measurements that motivated the present work were performed in Ref. [28].

6.2 Resonator design and measurement procedure

6.2.1 Resonator layout and fabrication

In chapter 4, we have discussed how to design and fabricate resonators extensively. In this measurement, one thing have to be pointed out is a wide range of frequency is needed so that we can map out the frequency dependence of the vortex response. The multiple resonators of different lengths patterned from the same film is designed and fabricated.

Our layout, as Figure 6.1(a) shows, consists of four quarter-wave CPW resonators

with lengths 15.2, 9.3, 4.4, and 2.8 mm, which, if we neglect the effects of the kinetic inductance of the superconductors for now, yields fundamental resonances near 1.8, 3.3, 6.9, and 11.0 GHz, as calculated with the Sonnet microwave circuit simulation software [72]. We design for the resonators to be somewhat over-coupled at zero field, where the loss at the measurement temperatures is dominated by thermally-excited quasiparticles. This gives us the ability to continue to resolve the resonance lines with the anticipated enhanced levels of loss once vortices are introduced.

In order to control the number of vortices in the resonators, we cool through the transition temperature T_c in an applied magnetic field B which as been discussed in chapter 4. The process for the trapping of vortices in a thin superconducting strip of width w upon field-cooling has been studied experimentally [88–90] and theoretically [91–93], indicating a threshold cooling field B_{th} below which all of the magnetic flux will be expelled from the strip. Apart from numerical details of the various approaches, this threshold field has been shown to scale approximately like $B_{th} \sim \Phi_0/w^2$. In order to trap vortices only in the resonators, we design the ground plane to have a lattice of holes, with the webbing and the feedline linewidth to be a factor of three narrower than that of the resonator, which is nominally 12 μm [Fig. 6.1(b)]. This should then provide about a decade of range in the cooling field where vortices are primarily trapped in the resonators, with $\Phi_0/w^2 \approx 14$ μT.

We use the same layout from Fig. 6.1(a) to pattern resonators from thin films of Re and Al. Please refer to chapter 4 for the fabrication of Re and Al resonators. The superconducting transition temperatures T_c for the films were identified with the corresponding step in the microwave transmission S_{21} through the feedline away from any of the resonance dips, leading to $T_c^{Re} = 1.70$ K and $T_c^{Al} = 1.13$ K. T_c measurement has been extensively discribed in chapter 3. The width of the center conductors for the measured resonators was 11.9 μm for the Re and 11.5 μm for the Al. The normal state resistivities were measured to be $\rho_n^{Re} = 1.6$ $\mu\Omega$-cm at 4 K, with RRR = 11, for the Re, and $\rho_n^{Al} = 0.33$ $\mu\Omega$-cm at 2 K, with RRR = 10, for the Al. RRR measurement
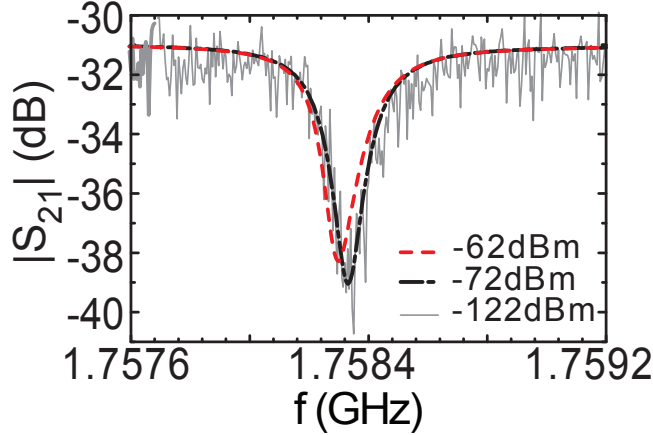
Figure 6.2: Dips in magnitude of S_{21} for different microwave drive power for the Re resonator near 1.8 GHz, $B = 92.5$ μT.

can be found in chapter 3.

6.2.2 Measurement procedure

We cool the resonators to ~ 300 mK using a ^{3}He refrigerator and we generate the magnetic field with a superconducting Helmholtz coil. A μ-metal cylinder attenuates stray magnetic fields in the laboratory. We perform our measurements using a vector network analyzer (Agilent N5230A) to record the magnitude and phase of the transmission through our feedline, S_{21}. The measurements setup is (4.1(b)) as what we discussed in chapter 4.

Away from any of the resonances, the feedline exhibits full transmission, while there is a transmission dip near a resonance. Over a wide range of power, roughly 60 dB, we observe no variation of the resonance lineshape [Fig. 6.2]. For stronger driving, ~ -62 dBm or larger delivered to the feedline, the dip becomes nonlinear and the quality factor decreases. The nonlinear response of strongly driven superconducting resonators has been investigated extensively in a variety of contexts [94–96]. To avoid such strong-driving nonlinearities we measure our resonators with a weak microwave drive, typically delivering a power of less than -82 dBm to the feedline.

The related discussion of power dependence in greater depth can be found in chapter 8.

6.3 Field cool experiment and measurement results

We study the influence of vortices in the resonators by repeatedly field-cooling through T_c in different magnetic fields. As it is mentioned in chapter 4, for each value of B, we heat the sample above T_c to 1.95 K (1.4 K) for Re (Al), adjust the current through our Helmholtz coil to the desired value, then cool down to 300 mK (310 mK) for Re (Al). During our measurements we regulate the temperature on the sample stage to within ± 0.2 mK of the stated values.

The addition of vortices through field-cooling results in a downward shift in the resonance frequency and a reduction in the quality factor. This general trend can be seen in Figure 6.3 where we plot the magnitude of S_{21} for several different cooling fields for the Re and Al chips for the resonator near 1.8 GHz. While the general trend is similar for the Re and Al resonators, the details of the response for the two materials are clearly quite different, with a more substantial broadening of the resonance dip with B for Al compared to the Re. By fitting the resonance trajectories for each of the four resonators at each cooling field on the Re and Al chips, we are able to extract the field and frequency dependence of Q_{fit} and f_0 for the two materials. This fitting process can be found in chapter 4.

We compute the excess loss in each resonator due to the presence of vortices, $1/Q_v$, by fitting the resonance at a particular magnetic field to obtain $1/Q_{fit}(B)$ and subtracting the inverse quality factor measured with $B = 0$, according to

$$\frac{1}{Q_v} = \frac{1}{Q_{fit}(B)} - \frac{1}{Q_{fit}(0)}, \tag{6.1}$$

thus removing the loss due to thermal quasiparticles, coupling to the feedline, and
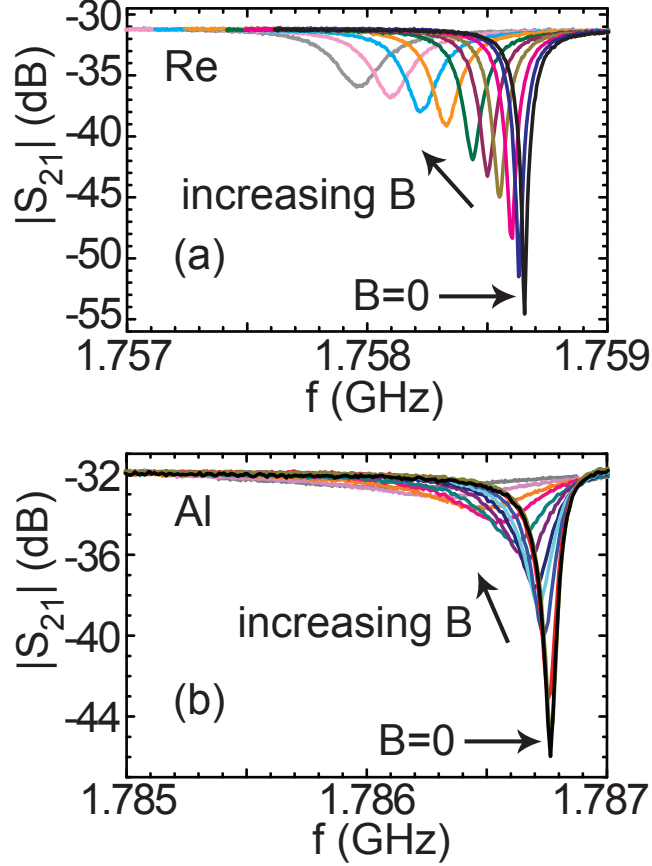
Figure 6.3: Magnitude of S_{21} for different cooling fields B for resonator near 1.8 GHz on (a) Re chip with B from 0 to 149.6 μT; (b) Al chip with B from 0 to 94.5 μT.

any other field-independent loss mechanisms. We also extract the fractional frequency shift of each resonance relative to its center frequency at $B = 0$:

$$\frac{\delta f}{f_0} = \frac{f_0(0) - f_0(B)}{f_0(0)}. \tag{6.2}$$

We plot $1/Q_v(B)$ and $\delta f/f_0(B)$ for Re [Figs. 6.4(a, c)] and Al [Figs. 6.4(b, d)]. For both materials, there is a region near zero field where there is essentially no change in $1/Q_v$ or f_0, corresponding to cooling fields below the threshold for trapping vortices in the resonators. Above this threshold, both $1/Q_v$ and $\delta f/f_0$ increase with
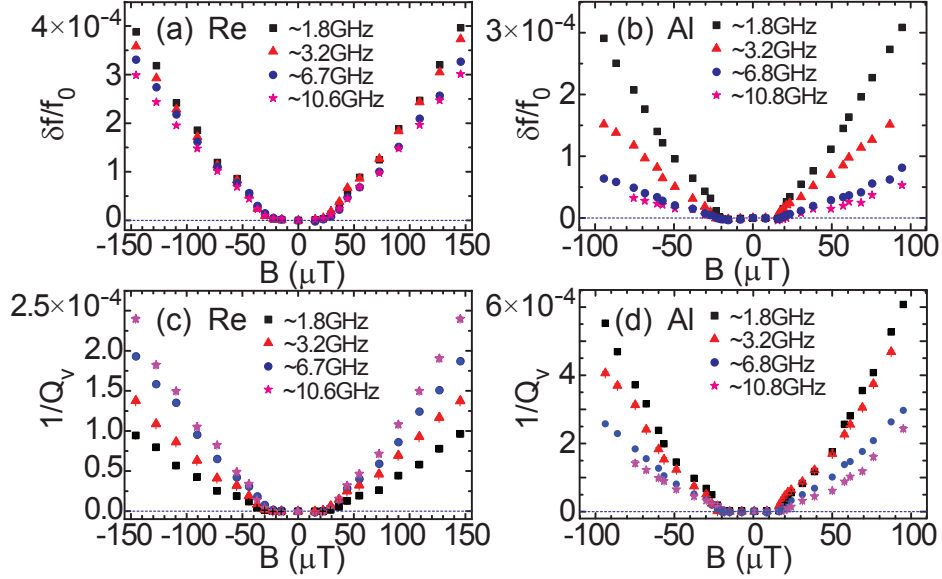
Figure 6.4: Fractional frequency shift $\delta f / f_0(B)$ for (a) Re and (b) Al. Excess loss due to vortices $1/Q_v(B)$, as defined by Eq. (6.1) for (c) Re and (d) Al.

$|B|$ for both materials. However, the frequency dependences of these quantities are quite different between the Re and Al films. For the Re resonators at a particular B, $\delta f / f_0$ decreases slightly with increasing frequency [Fig. 6.4(a)], while for Al there is a substantial decrease in $\delta f / f_0$ with increasing frequency [Fig. 6.4(b)]. Even more striking, the loss due to vortices $1/Q_v$ increases with frequency for Re [Fig. 6.4(c)], while it decreases for Al [Fig. 6.4(d)].

6.4 Model for high-frequency vortex response

6.4.1 Surface impedance analysis

In chapter 2, we have mentioned that Gittleman and Rosenblum (GR) first considered Eq. (2.23) and derived a complex resistivity due to the vortex response [18]. This model was later extended by Coffey and Clem [57], as well as Brandt [58], to address issues of microwave vortex dynamics in the high-T_c superconductors, including the

influence of flux creep, where vortices can wander between pinning sites either by thermal activation or tunneling [97]. Pompeo and Silva demonstrated that these various models can be described by a single expression for an effective complex resistivity $\tilde{\rho}_v$ due to vortices [23]:

$$\tilde{\rho}_v = \frac{\Phi_0 \left(B - B_{th} \right)}{\eta_e} \frac{\epsilon + if/f_d}{1 + if/f_d},$$
(6.3)

where $f_d = k_p/2\pi\eta_e$ is the characteristic depinning frequency that corresponds to the crossover from elastic to viscous response; ϵ is a dimensionless quantity that describes the strength of the flux creep and can range between 0 – recovering the zero-temperature GR model – and 1 – when $\tilde{\rho}_v$ is purely real and equal to the conventional Bardeen-Stephen flux-flow resistivity [47]. The threshold cooling field is accounted for by including B_{th}. For $B < B_{th}$ there are no vortices present and $\tilde{\rho}_v = 0$, although pinning can result in the trapping of vortices for B somewhat smaller than B_{th}. The real part of $\tilde{\rho}_v$ is associated with the loss contributed by the vortices, while the imaginary part of $\tilde{\rho}_v$ determines the reactive response of the vortices. Relating f_d and ϵ to the pinning potential depends on the details of the particular vortex dynamics model one considers [23].

We have mentioned in chapter 2, in a variety of contexts the microwave response of a superconductor is often characterized in terms of the surface impedance $Z_s = R_s + iX_s$. Changes in Z_s under different conditions, for example, different vortex densities determined by B, can then be separated into changes in the surface resistance $\Delta R_S(B)$ and reactance $\Delta X_S(B)$, where these quantities correspond to the differences between measurements at B and zero field. For a particular superconducting resonator, $\Delta R_S(B)$ and $\Delta X_S(B)$ can be related to the observable quantities $1/Q_{fit}$ and $\delta f/f_0$ through

$$\Delta R_s(B) = G\Delta \left[\frac{1}{Q_{fit}(B)} \right] = G \left[\frac{1}{Q_v(B)} \right],$$
(6.4)

$$\Delta X_s(B) = 2G \left[\frac{\delta f}{f_0(B)} \right],$$
(6.5)

where the geometrical parameter G depends on the details of the resonator geometry,

the current distribution, and the kinetic inductance contribution [98, 99]. Often the dimensionless ratio $r = \Delta X_S/\Delta R_S$ lends useful insight into the microwave response and thus eliminates the influence of G. The complex vortex resistivity $\tilde{\rho}_v$ can also be related to r as

$$
\begin{aligned}
r &= \frac{\text{Im}(\tilde{\rho}_v)}{\text{Re}(\tilde{\rho}_v)}, \\
&= \frac{1 - \epsilon}{(f/f_d) + (f_d/f)\epsilon}.
\end{aligned}
\tag{6.6}
$$

thus providing a path for comparing our measured quantities with the generalized vortex response given by Eq. (6.3) [23, 24]. By analyzing the $r-$parameter and its frequency dependence from our measurements, we will extract f_d and ϵ for the Re and Al films. We can then study the field dependence of the loss or frequency shift data separately to compare η_e for the two materials.

In Figure 6.5 we plot $r(B)$ calculated from the data in Figure 6.4 for the four different resonators on the Re and Al chips. For the Re resonators r is well above unity, indicating the dominance of the reactive contribution of the vortex dynamics in the frequency range covered by our chip layout. In contrast, r is near or somewhat less than unity for the Al resonators, indicating the significant loss related to the vortex motion in this system. When $|B|$ is less than the threshold to trap vortices, $1/Q_v \approx 0$ and r diverges, thus we do not include values for r in this range in Fig. 6.5. For $|B|$ somewhat larger than the threshold, r becomes roughly field-independent, particularly for the Re film. When $|B|$ is just beyond the threshold, there are clear differences in $r(B)$ between the Re and Al films that will be addressed shortly.

6.4.2   Determination of depinning frequency

The frequency dependence of r can be seen in Figure 6.5 by focusing on a particular value of B and observing the variation in r for the four resonators. We plot this explicitly in Figure 6.6 for one field each for Re and Al, where, for both films, r decreases with frequency. We can make a two-parameter fit to the $r(f)$ data in Fig.
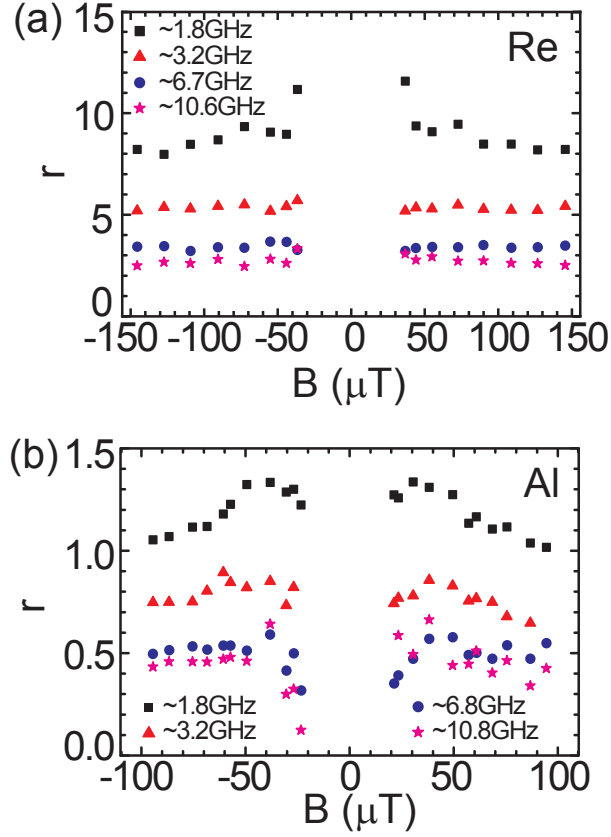
Figure 6.5: $r(B)$ for (a) Re and (b) Al films for four different resonator lengths.
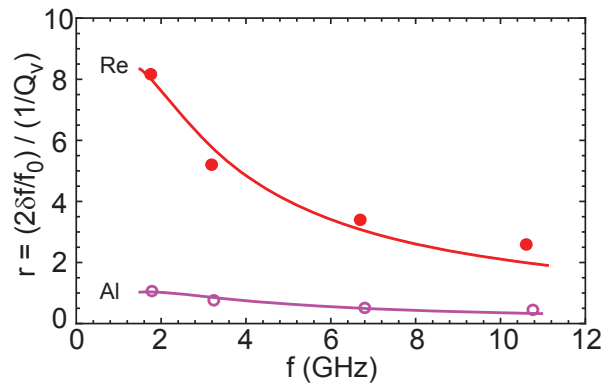
Figure 6.6: $r(f)$ for Re with $B = -130.9$ μT (closed circles) and Al with $B = -94.4$ μT (open circles) along with fits as described in text. Fit parameters are $f_d = 22.6$ GHz (4.2 GHz) and $\epsilon = 0.0039$ (0.17) for Re (Al).
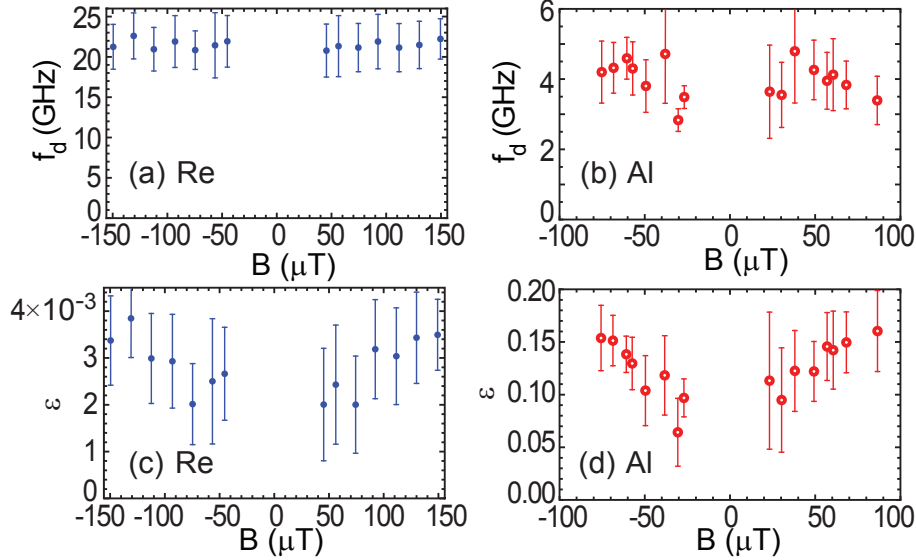
Figure 6.7: $B-$dependence of parameters from fits to $r(f)$ at each B: f_d for (a) Re and (b) Al; ϵ for (c) Re and (d) Al films. Note the different scale factors on ϵ between (c) and (d).

6.6 with Eqs. (6.6) by varying f_d and ϵ. Performing this same analysis for each value of B in Figure 6.5 yields fit values $f_d(B)$ and $\epsilon(B)$ (Fig. 6.7). We note that for both our Re and Al data, it is not possible to fit $r(f)$ with $\epsilon = 0$.

From Figure 6.7, there is clearly a substantial difference in f_d for the Re and Al films. For $|B| > 50$ μT, well beyond the threshold for trapping vortices, the average of f_d^{Re} from Figure 6.7(a) is 22 GHz, much higher than our highest resonator fundamental frequency. In contrast, for Al, the average of f_d^{Al} from Figure 6.7(b) is 4 GHz, near the lower end of our resonator frequencies.

6.4.3 Modeling microwave vortex response

The ratio of the depinning frequencies $f_d^{\mathrm{Re}}/f_d^{\mathrm{Al}}$ can be used to compare the relative pinning strength for the Re and Al films with the following expression

$$\frac{k_p^{\mathrm{Re}}}{k_p^{\mathrm{Al}}} = \left(\frac{f_d^{\mathrm{Re}}}{f_d^{\mathrm{Al}}}\right)\left(\frac{\eta_e^{\mathrm{Re}}}{\eta_e^{\mathrm{Al}}}\right). \tag{6.7}$$

We can extract $\eta_e^{\mathrm{Re}}/\eta_e^{\mathrm{Al}}$ from the $1/Q_v(B)$ data of Figure 6.4 based on Eq. (6.3) by writing the resistance due to vortices R_v as

$$
\begin{aligned}
R_v &= j(x)\mathrm{Re}\left[\tilde{\rho}_v\right]\left(\frac{l}{wt}\right) \\
&= j(x)\frac{B\phi\left(f/f_d + f_d/f\epsilon\right)}{(f/f_d + f_d/f)\eta_e}\frac{l}{wt}
\end{aligned}
\tag{6.8}
$$

where l is the resonator length, t is the thickness, and $j(x)$ is a dimensionless factor that scales R_v based on the current density $J_s(x)$ at the position x of the vortices across the width of the resonator. In general, $J_s(x)$ will be non-uniform with more current flowing along the edges of the center conductor. Thus, $j(x) = J_s(x)^2/\langle J_s\rangle^2$, where $\langle J_s\rangle$ is the average current density across the center conductor. The numerical calculation of $j(x)$ will be discussed further in the later section 6.6.1. For a resonator at f_0, $1/Q_v$ can be related to R_v and then $\tilde{\rho}_v$ by

$$
\begin{aligned}
1/Q_v &= \frac{(R_v/l)}{2\pi f_0 L'} \\
&= \frac{j(x)\mathrm{Re}\left[\tilde{\rho}_v\right]}{2\pi f_0 wt L'}
\end{aligned}
\tag{6.9}
$$

where L' is the inductance per unit length of the resonator. After applying the definition of $\tilde{\rho}_v$ from Eq. (6.3) we then differentiate both sides of Eq. (6.9) with respect to B:

$$
1/Q_v = j(x)\frac{B\phi\left(f/f_d + \epsilon f_d/f\right)}{(f/f_d + f_d/f)\eta_e}\frac{1}{wt2\pi f_0 L'}
\tag{6.10}
$$

$$
\frac{\partial(1/Q_v)}{\partial B} = \frac{j(x)\Phi_0}{2\pi f_0 wL'}\left(\frac{1}{t\eta_e}\right)\left[\frac{\epsilon + (f_0/f_d)^2}{1 + (f_0/f_d)^2}\right].
\tag{6.11}
$$

By scaling with the frequency-independent factors on the right-hand side of Eq. (6.11), we can investigate the frequency dependence of $\partial(1/Q_v)/\partial B$. In Figure 6.8(a), we plot $q(f_0/f_d)$

$$
q(f_0/f_d) = (f_d/f_0)\frac{\epsilon + (f_0/f_d)^2}{1 + (f_0/f_d)^2}
\tag{6.12}
$$

for the ϵ values obtained from fits to the $r(f)$ data for Re and Al. With ϵ small, $q(f_0/f_d)$ is an increasing function for $f_0 < f_d$ – characteristic of our measurements
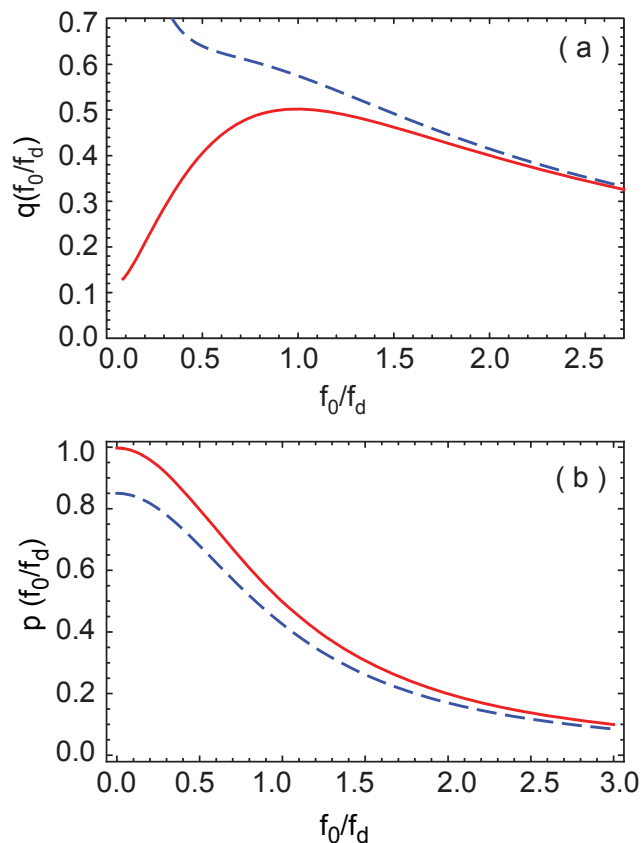
Figure 6.8: Plot of $q(f_0/f_d)$ and $p(f_0/f_d)$. computed based on definition in the text, $q(f_0/f_d)$ $(p(f_0/f_d))$ is proportional to $\partial(1/Q_v)/\partial B$ $(\partial(\delta f/f_0)/\partial B)$ with ϵ values from text corresponding to Re (solid red line) and Al (dashed purple line).

on Re, where all of the resonances are below f_d^{Re} and there is greater loss at higher frequencies. For $f_0 > f_d$, $q(f_0/f_d)$ is a decreasing function. In addition, a larger value of ϵ enhances the loss at frequencies comparable to and less than f_d, and this dependence is characteristic of our measurements on Al, where f_d^{Al} is near the lower end of our resonances and we observe a decrease in the loss for increasing frequency.

At the same time, we can also follow the same process to explain the frequency dependence of frequency shift due to the applied field. In Figure 6.8(b) we plot

$p(f_0/f_d)$ for the ϵ values obtained from fits to the $r(f)$ data for Re and Al.

$$\frac{\partial(\delta f/f_0)}{\partial B} = cons.(f_d/f_0)\left[\frac{(1-\epsilon)(f_0/f_d)}{1+(f_0/f_d)^2}\right] \tag{6.13}$$

$$p(f_0/f_d) = (f_d/f_0)\left[\frac{(1-\epsilon)(f_0/f_d)}{1+(f_0/f_d)^2}\right] \tag{6.14}$$

From Figure 6.8(b), frequency shift for both Al and Re decreases with the center frequency. At the same time, the range of f_0/f_d is $\sim (0.08 - 0.49)$ for Re and $\sim (0.45 - 2.7)$ for Al and it indicates from Figure 6.8(b) Al has bigger frequency shift than Re which agrees with what we see from the measured data as plotted in Figure 6.4(a) and (b).

We can compute $\partial(1/Q_v)/\partial B$ from the data in Fig. 6.4(c) and 6.4(d) by making linear fits for the intermediate-range B data beyond the threshold shoulder. If we then use the ϵ and f_d parameters from the $r(f)$ fits in Figure 6.7, and neglect the small difference in L' between the Re and Al resonators because of differences in kinetic inductance, we can apply Eq. (6.11) to the Al and Re data, then take the ratio of these for each of the four resonator lengths. After accounting for $t^{\mathrm{Re}}/t^{\mathrm{Al}}$ we obtain $\eta_e^{\mathrm{Re}}/\eta_e^{\mathrm{Al}} \approx 1$. At the same time, we can also compute $\partial(\delta f/f_0)/\partial B$ from the data in Fig. 6.4(a) and 6.4(b) by making similar linear fits as the fits in Fig. 6.4(c) and 6.4(d). Taking the ϵ and f_d paramters from Figure 6.7, and appling Eq. (6.13) to the Al and Re data, such analysis yields approximately the same value for $\eta_e^{\mathrm{Re}}/\eta_e^{\mathrm{Al}}$.

For comparison, we can also estimate $\eta_e^{\mathrm{Re}}/\eta_e^{\mathrm{Al}}$ assuming η_e corresponds to the Bardeen-Stephen (BS) flux-flow viscosity η [47]. In this model, each vortex core is treated as a normal cylinder with a radius equal to the effective coherence length ξ_e with resistivity ρ_n. Dissipation during the vortex motion leads to a viscosity as equation 6.15 [34, 47].

$$\eta = \frac{\Phi_0^2}{2\pi\rho_n\xi_e^2} \tag{6.15}$$

Using $\rho^{\mathrm{Al}}l^{\mathrm{Al}} = 4 \times 10^{-16}$ Ω m^2 from Ref. [100] and our measured value of ρ^{Al}, we estimate the electronic mean free path of our Al film to be of the order of 100 nm,

much less than the BCS coherence length for Al, $\xi_0 \approx 1500$ nm [34], thus putting the Al film well into the dirty-limit. We have measured the shift in T_c as a function of magnetic field for the Al film, and thus obtained $S = -dB_{c2}/dT \mid_{T_c}$ (please refer back to chapter 5), which we can then use with the standard dirty-limit expression [101] to obtain the effective coherence length $\xi_e^{\text{Al}} \approx 230$ nm, consistent with estimates for other Al thin films [100].

We are not aware of any measurements of the coherence length in Re. Furthermore, it is not clear if the Re films are in the dirty limit, thus we can attempt to estimate ξ_e^{Re} using the BCS expression: $\xi_0 = \hbar v_F / \pi \Delta(0)$ with $\Delta(0) = 1.76 k_B T_c$ [34]. If we apply the free-electron model, we can write $v_F = (\pi k_B / e)^2 / \gamma \rho l$, where γ is the linear coefficient of the specific heat (260 J m^{-3} K^{-2} for Re [102]). The quantity ρl is the product of the resistivity and mean free path with reported values for Re of 4.5×10^{-15} Ω m^2 in Ref. [103] and 2.16×10^{-15} Ω m^2 in Ref. [104]. This results in $\xi_0^{\text{Re}} \approx 50 - 100$ nm. We note that these values of ρl imply a mean free path for our Re film between $\sim 140 - 280$ nm, thus confirming that the film is not in the dirty limit. Thus, we will assume $\xi_e^{\text{Re}} = \xi_0^{\text{Re}}$.

Using the BS flux-flow model with the parameter estimates above results in a viscosity ratio:

$$\frac{\eta_e^{\text{Re}}}{\eta_e^{\text{Al}}} = \left(\frac{\rho_n^{\text{Al}}}{\rho_n^{\text{Re}}} \right) \left(\frac{\xi_e^{\text{Al}}}{\xi_e^{\text{Re}}} \right)^2 \tag{6.16}$$

between 1 and 4, depending on the value for ξ_e^{Re}, with the lower end of this range consistent with our measured viscosity ratio of ~ 1 from the $1/Q_v(B)$ data. Combining a viscosity ratio of $\eta_e^{\text{Re}}/\eta_e^{\text{Al}} \approx 1$ with the ratio of our depinning frequency fit values $f_d^{\text{Re}}/f_d^{\text{Al}}$ in Eq. (6.7) results in:

$$\frac{k_p^{\text{Re}}}{k_p^{\text{Al}}} \approx 5. \tag{6.17}$$

The Re films in our experiment are nearly epitaxial, but highly twinned, based on reflection high-energy electron diffraction (RHEED) measurements during the film deposition. Such extended defects likely result in strong pinning, particularly when

the twins are oriented roughly along the length of the resonators, and thus perpen-
dicular to the Lorentz force direction. On the other hand, the Al films deposited on
non-heated substrates likely do not have such extended defect structures, but rather
have defects that are small compared to ξ_e^{Al}. Thus, one would expect weaker pinning
in the Al films, consistent with $k_p^{\mathrm{Re}}/k_p^{\mathrm{Al}} > 1$.

6.5 Threshold cooling fields for trapping vortices

6.5.1 Previous studies of the threshold cooling field for su- perconducting strips

The field-cooling of a thin superconducting strip has been studied theoretically by
Likharev [93], Clem [91], and Maksimova [92] and these treatments were also described
in Refs. [88–90], as it is mentioned in chapter 2. Sufficiently close to T_c, the effective
thin-film penetration depth $\Lambda = 2\lambda^2/d$ can become comparable to the strip width
w, resulting in a uniform field distribution throughout the strip just below T_c. As
the temperature is lowered further and superconducting order develops, the magnetic
field through the strip nucleates into vortices and the ultimate spatial distribution of
these depends on the vortex Gibbs free energy.

The theoretical treatments of this problem have considered the Gibbs free energy
for a single vortex in the strip, $G(x)$, where the x-coordinate is oriented across the
width of the strip. This is determined by the interaction energy of the Meissner
screening currents in the strip with the vortex and the self-energy of the vortex
circulating currents. As the Figure 6.9 in paper [88],For small magnetic fields, $G(x)$
has a maximum in the center of the strip and falls off towards the edges of the strip,
thus vortices do not nucleate in the strip upon cooling below T_c. As the strength of
the cooling field is increased, the maximum in the middle of the strip flattens and
eventually develops a dip in the center of the strip.

Clem [91] and Maksimova [92] considered the development of this dip at magnetic
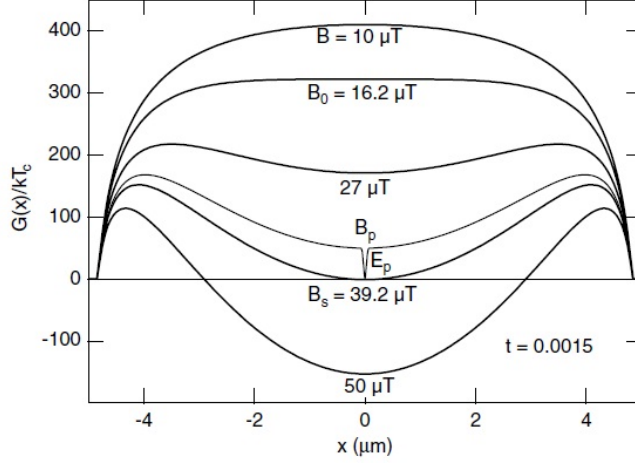
Figure 6.9: The Gibbs free energy of a single vortex located at position x at several values of the applied field $\vec{B}$, at a reduced temperature $t = 1 - T/T_c$ of 0.0015. (from Stan *et al.*, 2004, p.97003)

field:

$$B_0 = \frac{\pi \Phi_0}{4w^2}. \tag{6.18}$$

to correspond to the threshold field for trapping vortices near the center of the strip.

Likharev argued that the trapping threshold is not reached until $G(x) = 0$ in the center of the strip [93], leading to the expression:

$$B_s = \frac{2\Phi_0}{\pi w^2} \ln\left(\frac{\alpha w}{\xi}\right). \tag{6.19}$$

The constant α is related to the treatment of the vortex core and can be $2/\pi$ by Clem [105] or $1/4$ by Likharev [93].

Stan *et al.* fabricated the different width Nb strips and cooled them through T_c to do threshold field imaging experiment. In their measurements, they used a low-temperature scanning Hall-probe microscopy (SHM) to image vortices in Nb thin film strips. The SHM device they used has wide field scanning head which allows them to get good counting statistics. The representative images of vortices with magnetic field in these different width Nb strips was observed as Figure 6.10. Stan *et al.* determined the critical field by repeating field cool measurements at many different applied fields and counting the number of vortices in each strip. For instance, for a 10 μm strip
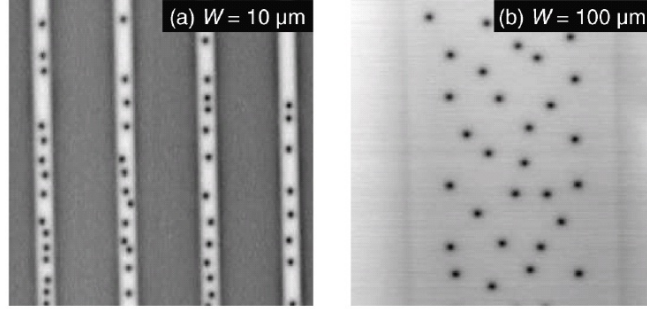
Figure 6.10: Image (a) is vortices in 10 μm strip at B=85 μT, and image (b) is vortices in 100 μm strip with applied field B=5.3 μT. (from Stan *et al.*, 2004, p.97003)
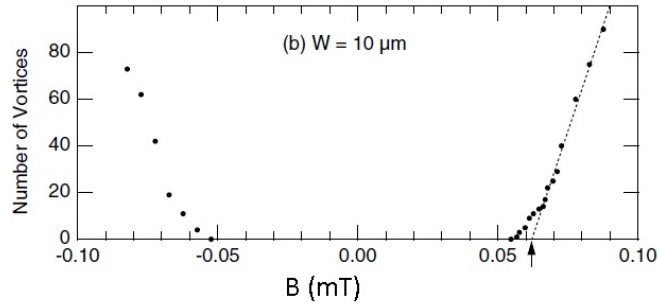
Figure 6.11: Field cool for 10 μm strip. (from Stan *et al.*, 2004, p.97003)

which is close to our resonator's width 12 μm, Figure 6.11 showed the relationship between the number of vortices and the different external field. In Stan's paper, they claimed that Eq. (6.19) with $\alpha = 2/\pi$ best described their observed values of B_{th}.

A related model for vortex trapping in thin superconducting strips was proposed by Kuit *et al.* [89], who considered the creation of vortex-antivortex pairs upon cooling through T_c. This model predicts a threshold field:

$$B_K = 1.65\frac{\Phi_0}{w^2}.$$
(6.20)

and successfully described the measured B_{th} values for field-cooled YBCO strips of different widths [89].

6.5.2   Extracting threshold fields for Al and Re resonators

In our experiment, we have made testing resonators on a chip with wide center fre-
quency range, but the same width of 12 μm, or resonators with similar center fre-
quency but different widths. Compared with Stan's experiment, they used Nb thin
film strips, but we made resonators with different material than theirs, Al and Re.
Our results can furtherly approve the magnitude of the threshold field. In this sec-
tion, we will find out the B_{th} for 12 μm Al and Re resonators, and in section 6.5.4,
B_{th} for Al resonators with different width will be discussed.

In order to examine the field dependence near B_{th} more closely, in Figure 6.12
we plot $1/Q_v(B)$ for Re and Al together, but only for $B \geq 0$ for the lowest- [Fig.
6.12(a)] and highest-frequency [Fig. 6.12(b)] resonators. Near $B = 0$ we observe
$1/Q_v \approx 0$, indicating the presence of a threshold field below which vortices are not
trapped in the resonators. For magnetic fields beyond the initial onset from $1/Q_v = 0$,
there is a linear increase in $1/Q_v$ and we include linear fits to $1/Q_v(B)$ [Fig. 6.12(a,
b)]. Assuming $1/Q_v$ is proportional to the density of vortices in the resonator, our
observed $1/Q_v(B)$ corresponds to a linear increase in vortex density with B, consistent
with previous magnetic imaging measurements of field-cooled superconducting strips
[88, 89]. Following this analysis, we can identify the point where these linear fits
intercept $1/Q_v = 0$ as B_{th}. For the linear fits to the Re (Al) data, we obtain $B_{th}^{\mathrm{Re}} =
45 \pm 2$ μT ($B_{th}^{\mathrm{Al}} = 30 \pm 2$ μT) for the resonator near 1.8 GHz.

If we take our B_{th} values from the resonators near 1.8 GHz, $B_{th}^{\mathrm{Re}} = 45 \pm 2$ μT
and $B_{th}^{\mathrm{Al}} = 30 \pm 2$ μT, we can compare these with the various approaches. All of
our resonators are nominally 12 μm wide, thus $B_0 = 11$ μT and $B_K = 24$ μT,
which are below our measured B_{th} and do not account for the differences between
the Re and Al films. Applying Eq. (6.19) with $\alpha = 2/\pi$ and assuming $B_s = B_{th}$, we
obtain $\xi_e^{\mathrm{Re}} = 60$ nm and $\xi_e^{\mathrm{Al}} = 360$ nm. We note that these are within a factor of
~ 2 of our earlier estimates for ξ_e^{Re} and ξ_e^{Al}, although one might expect the relevant
coherence lengths in determining B_{th} to be somewhat larger, corresponding to an
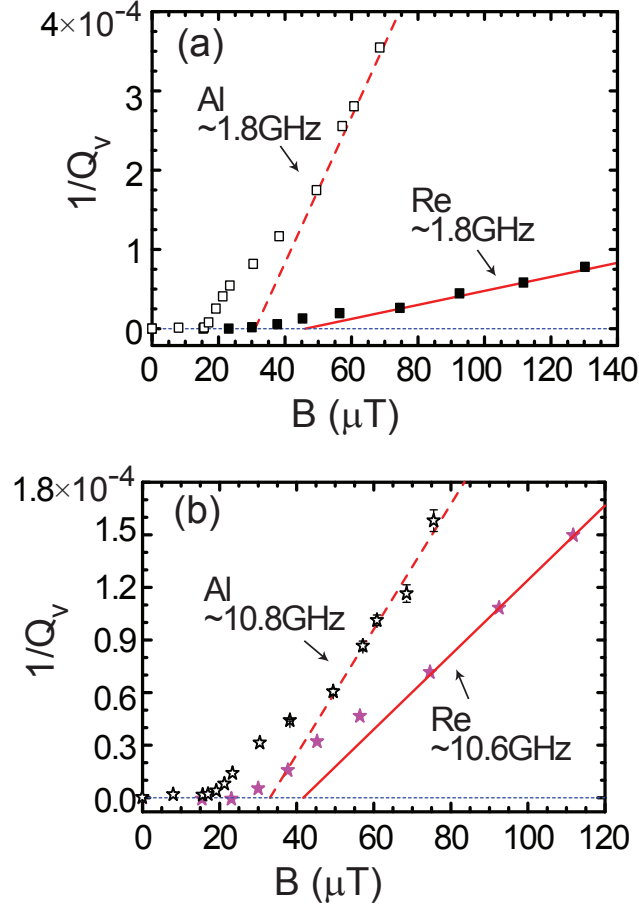
Figure 6.12: $1/Q_v(B)$ for $B \geq 0$ for Re and Al together for (a) lowest-frequency resonator; (b) highest-frequency resonator. Solid lines are linear fits to the B-dependence well beyond the shoulder region as described in text. B_{th} corresponds to intercept of fit line with $1/Q_v = 0$.

elevated temperature at which vortices first become trapped in the films during the cooling process. On the other hand, the logarithm makes the dependence of B_s on w/ξ weak, thus making it difficult to perform a detailed quantitative comparison of ξ_e based on the B_{th} values alone. It is possible that the various trapping models require modifications to account for films of superconductors that are Type-I in the bulk and thus have relatively short penetration depths. If Λ were to remain finite compared to w at the temperatures where vortices begin to nucleate, the assumptions of weak screening and nearly uniform magnetic field distributions would need to be adjusted.

6.5.3   Initial trapping of vortices

In Figure 6.12(a) and 6.12(b) it is clear that $1/Q_v(B)$ deviates from the linear dependence for fields near B_{th}, and $1/Q_v$ first becomes nonzero at $B = B_{onset} < B_{th}$. Thus $1/Q_v(B)$ exhibits shoulders, with $B_{onset}^{\text{Re}} \approx 30~\mu$T and $B_{onset}^{\text{Al}} \approx 20~\mu$T. Stan $et~al.$ observed a deviation at small fields from the linear increase of vortex density with B and the initial trapping of vortices occurred at magnetic fields somewhat below B_{th} [88]. This behavior was attributed to the presence of pinning, which resulted in local minima in $G(x)$ such that vortices could become trapped in the strip for $B < B_s$. Subsequently, Bronson $et~al.$ performed numerical simulations of this process and were able to obtain $n(B)$ curves that agreed with the measurements of Stan $et~al.$ [90], where n is the vortex density. By varying the pinning strength and density, Bronson $et~al.$ found regimes where $n(B)$ increased for $B < B_{th}$ with a smaller slope than the linear increase observed at large fields, as well as regimes where $n(B)$ increased more steeply for $B < B_{th}$ than the linear dependence at large fields, resulting in a shoulder on $n(B)$.

If we assume that $1/Q_v(B)$ is proportional to $n(B)$ in our Re and Al resonators, the shoulders that we observe in $1/Q_v(B)$ for $B < B_{th}$ would be related to the same enhancement of vortex trapping by pinning as discussed in Refs. [88, 90]. However, if one examines the $r(B)$ data plotted in Fig. 6.5, it appears that the situation may be somewhat more subtle. In the simplest case, if there were pinning wells of only one depth, one would expect $r(B)$ for a particular frequency to be flat, at least for $n(B)$ less than the density of pinning sites, as the $B-$dependence in the frequency shift and loss would cancel out for the calculation of r. On the other hand, a distribution of pinning well depths would likely favor the initial trapping of vortices in the deepest pinning wells, which would result in larger values of r for B just above B_{onset}. Such a picture, with a few deeper pinning wells, is consistent with our measurements of $r(B)$ in Re [Fig. 6.5(a)], where $r(B)$ is mostly flat, with a small upturn as $|B|$ approaches B_{onset}, particularly for the lowest frequency resonator. The measurements of $r(B)$ for
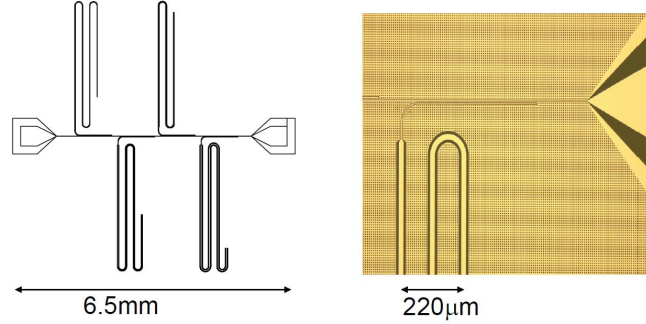
Figure 6.13: (a)The layout of four resonators with different width of 4, 8, 12 and 20 μm capacitively couple to one common feed line, (b) is the image of one 20 μm resonator from a microscope.

Al [Fig. 6.5(b)] exhibit a more gradual increase in r as $|B|$ is reduced towards B_{th}, which may be related to a broader distribution of pinning energies in the Al films. The decrease in $r(B)$ for $B_{onset} < B < B_{th}$ for the Al resonators, implying a weaker pinning of the initial vortices trapped in the film, is not understood presently.

6.5.4 Variations in threshold field for different width resonators

A new set of resonators with different width was designed as Figure 6.13(a) in order to explore the variation of the threshold field with the center-conductor width. In this layout, we have four resonators with width of 4, 8, 12, and 20 μm capacitively couple to one common feed line. Instead of a wide range of center frequency, all of the resonators resonate $\sim$ 4GHz and has the same elbow width $4\mu m$ and $2\mu m$ gap, After the elbow part, a taper is used to change a resonator to the desired width. There is also $2\mu m$ metal part between the feed line gap and elbow gap. The coupling Q_c are around 15k.

This film was made by our cooperator in Wisconsin. A 150 nm-thick Al was sputtered onto 2-inch sapphire wafer which is a different way of deposition. We were looking at differences in pinning between sputtered and evaporated films, at the same time, this chip also can help to reveal the variation of the threshold field with diffenent
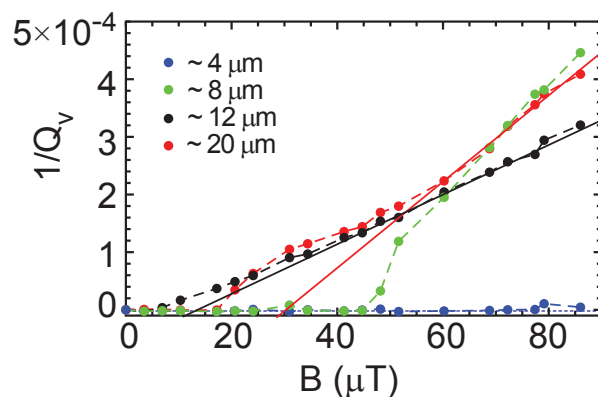
Figure 6.14: Loss due to vortices $1/Q_v(B)$

center strip width. The resonators were then patterned photolithographically followed by a reactive ion etch in a combination of BCl_3, Cl_2, and CH_4 (Al) or SF_6 and Ar (Re) as I mentioned in chapter 4. The T_c of this Al film is around 1.15K and the RRR is 5.7.

We cooled our resonators to 310 mK using a 3He refrigerator, the similar measurement set up as figure 6.1 is used. A 3 dB attenuator is installed on the output side of the sample to reduce any power reflecting back from HEMT or any non matching joints. A HEMT is used to amplify the output signal and a homemade Helmholtz coil is employed to provide the magnetic field.

Counting the attenuation and the loss from the cable and to avoid the nonliearity, driving power $\sim$ -85 dBm or less power delivered to the feed line. Related disscussion has been made in section 6.2.2.

By repeating the field cool experiment with different magnetic field (discussed in chapter 4) and analysing the data from fitting as I mentioned in section 4.5, Figure 6.14 shows the relationship between vortex loss and the applied magnetic field. Only the positive field is presented here. The dashed line connecting points with labels as a, b, c, and d represent the resonators with width 4, 8, 12 and 20 μm respectively. For the $4\mu m$ resonator, quality factor doesn't change with the field. For the wider resoantors, however, the loss increases in different rate with the field after their own

threshold field (B_s). The linear fits can be drawn in the Figure for 12 and 20 μm resonators, and x-intercept of linear fits gives us B_s. For 8 μm resoantor, although loss increases when the field is above ~ 45 μT, we believe it is still the shoulder and haven't enter the linear part yet, hence, the fit is not included. As we disscussed before, the threshold field can be theoretically predicted from the following equation by assuming ξ_e is what we got from the last chip which is 230 nm (Please refer to Table 6.2).

$$B_s = \frac{2\Phi_0}{\pi w^2} \ln\left(\frac{2w}{\pi\xi}\right). \tag{6.21}$$

Meanwhile, I have to point out that this expression 6.21 was the most consistent with the earlier imaging experiments and agreed with our initial measurements on $12\mu m$ resonators

A Table 6.1 is included here to compare the measured and calculated B_s. B_{sm} is measured threshold field and B_{sc} stands for the calculated threshold field according to equation 6.21. In this Table, the theoretical threshold field for $4\mu m$ resonator is

Table 6.1: Table of measured and calculated threshold field

Width of Resonator	$4\mu m$	$8\mu m$	$12\mu m$	$20\mu m$
$B_{sm}(\mu T)$	n/a	n/a	30.3	13.6
$B_{sc}(\mu T)$	198.0	63.8	32.1	13.2

198 μT which is beyond the field we have measured, and it explains the constant quality factor we got for this resonator in the experiment. For two wider resonators, calculated values are close to the measured ones.

The points in Figure 6.15 are two threshold fields of 12 and 20 μm resonators. We took the same ξ value from before and calculated $B_s(w)$ and found good agreement with the two data points
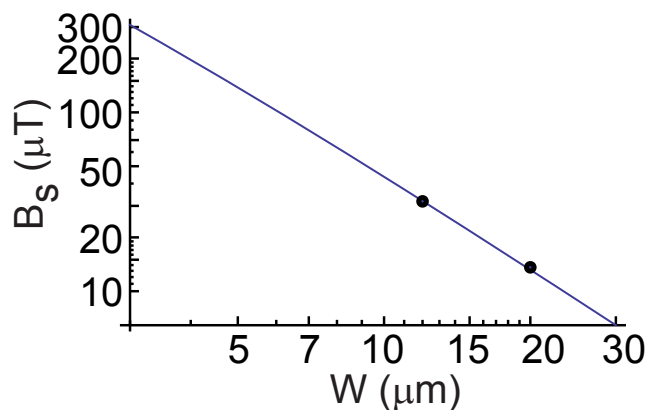
Figure 6.15: Plot of threshold field with width of resonators, and the straight line is the line calculated according to equation with ξ to be 230nm. 6.21
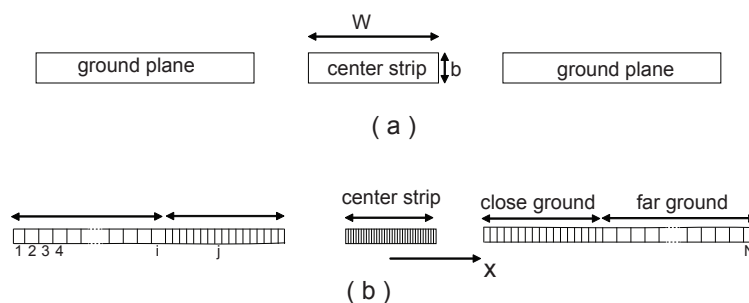
Figure 6.16: (a) Cross section of a thin ceter strip carrying a current in the z direction (b) Configuration of CPW for calculating current density $J_s(x)$

6.6   Vortex distribution

6.6.1   Calculation of $J_s(x)$

The vortex position in the resonator plays an important role in determining the response because of the non-uniform current density distribution in a superconducting coplanar waveguide $J_s(x)$, where the current density is larger at the edges. Thus, one must account for this when converting from $\tilde{\rho}_v$ to, for example, an effective resistance R_v, as in Eq. 6.8.

It is well known that if the width of a thin film strip w as it is shown in Figure 6.16(a) is much greater than penetration depth λ, and the thickness b is much smaller

than the λ, we can assume that the current density is uniformly distributed in the film strip. In our case, as the width of our film $(12\mu m)$ is much bigger than the penetration depth and the thickness (150nm), we can use this assumption to assume the current distribution in y axes is uniform. In the x direction, however, we know the current mostly flows at the edge, not in the center where the vortices are located. There is an analogy between these two situations: two dimensional magnetic fields from current flowing in a superconducting thin strip as it is shown in Figure 6.16(a) and the electrostatic fields produced by the surface charge around the same shape conductor. As they both have to satisfy the same differential equations and the same boundary equations. Because of this analogy, current density $\vec{J}$ must be distributed in the superconductor in the same way as ρ in the conductor [82]. In order to get the numerical solution to the current density, we divided our center condutor and ground plane into multiple columns using the idea from a Ref. [106]. Figure 6.16(b) is a configuration of cross section view of our CPW with multiple divisions. We treated ground plane as two different parts; close ground plane has more fine divisions and far ground plane has bigger ones. As we have an idea in advance of how the distribution will look like; A finer mesh where J(x) will vary more rapidly and a wider mesh where it will vary more slowly can get us relatively more accurate results. By doing so, we can assume the current density in each column to be uniform.

In Figure 6.16(b), each division can be treated as one rod and they are labeled as 1, 2, 3, $\cdots$, i, $\cdots$ N. The potential of a rod i carrying a charge density ρ_i at distance r is:

$$V(r) \propto \rho_i \log(1/r) \tag{6.22}$$

the net potential at position i (V_i) due to all the other rods from 1 to N is:

$$V_i = \sum_{n=1}^{N} V_{in} \tag{6.23}$$
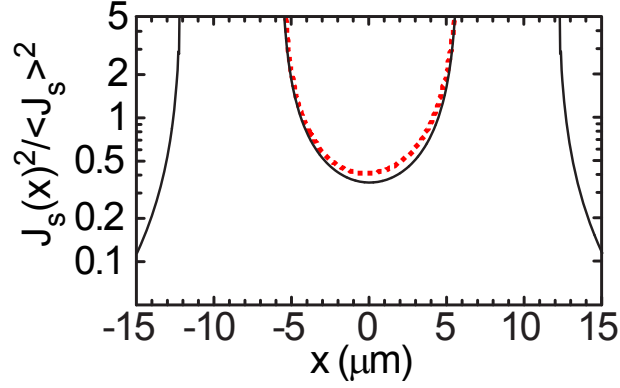
Figure 6.17: Dotted red line is current density predicted from equation 6.24 and black line is the solution by dividing conductor and ground plane into multiple rectangle patches. They show fairly reasonable agreement.

we can express the voltage and charge density in a matrix form as:

$$
\begin{pmatrix} V_1 \\ V_2 \\ \vdots \\ V_N \end{pmatrix} \propto \begin{pmatrix} \log(1/r_{11}) & \log(1/r_{12}) & \ldots & \log(1/r_{1N}) \\ \log(1/r_{21}) & \log(1/r_{22}) & \ldots & \log(1/r_{2N}) \\ \ldots & \ldots & \ldots & \ldots \\ \log(1/r_{N1}) & \log(1/r_{N2}) & \ldots & \log(1/r_{NN}) \end{pmatrix} \times \begin{pmatrix} \rho_1 \\ \rho_2 \\ \vdots \\ \rho_N \end{pmatrix}
$$

Then the charge distribution can be calcualted from equation above, the voltages in our CPW configuration, is 0 for two ground plane and 1 for the center strip.

Using the above assumption and the analogy method, the simulation result are plotted out in Figure 6.17(the back continuous line) for our CPW geometry, where we have scaled $J_s(x)^2$ by the square of the average current density in the center conductor $\langle J_s \rangle^2$ to obtain the dimensionless factor $j(x)$ that we introduced previously. Vortices trapped along the centerline of the resonator will experience the smallest $J_s(x)$ and will thus exhibit the weakest response compared to vortices trapped near the resonator edge, which will respond most strongly.

Van Duzer [82] developed an alternative to a numberical calculation; an analytic approximation to the current distribution across the width of an isolated, current-carrying superconducting strip. The normalized square of the current density is found
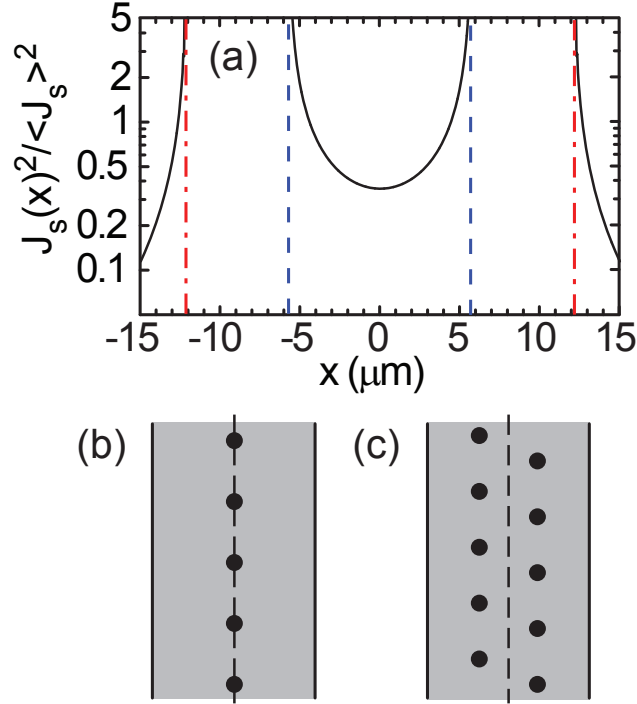
Figure 6.18: (a) Calculated current density distribution normalized by the average current density, $j(x) = J_s(x)^2/\langle J_s \rangle^2$, for CPW geometry with parameters for Al resonator: $w = 11.5$ μm (indicated by blue dashed lines) and 6.4 μm gap between the center conductor and the ground plane (indicated by red dash-dotted lines). Predicted vortex configurations in absence of pinning disorder based on Ref. [90] for (b) $B_{th} < B < 2.48B_{th}$; (c) $B > 2.48B_{th}$.

to be

$$\frac{J_s(x)^2}{\langle J_s \rangle^2} = \frac{4}{\pi^2} \frac{1}{1 - (2x/w)^2} \tag{6.24}$$

This prediction is also plotted in Fig. 6.17 (the red dotted line), and shows fairly reasonable agreement even though the ground planes are quite close to the center strip.

6.6.2   Model of vortex distributions

As we all known, the tendency of vortices in a clean, infinite SC sheet is to form a lattice due to the mutual repulsion between all the vortices. In a strip, however, the

vortices repel each other but they also interact with the screening current distribution in the strip. From the vortex imaging measurements of Stan *et al.* and Kuit *et al.*, for B just beyond B_{onset}, the vortices tended to line up in a single row along the centerline of the strips, while for somewhat larger B the vortices formed multiple rows [88, 89]. The numerical simulations of Bronson *et al.* indicated that the confinement of the vortices by the screening currents flowing in the strip forces the vortices form a single row until $B = 2.48 B_{th}$, at which point the distribution would split into two rows, one on either side of the strip centerline at $x \approx \pm (w/2)/3$ [90] [Fig. 6.18(b, c)]. For $B \approx 5 B_{th}$ the vortices would then form three rows, and so on. Following these simulations, our measured values of B_{th} for the Re and Al films would correspond to the single-row configuration over much of the range of B from our measurements, with the condition $B > 2.48 B_{th}$ occurring towards the upper end of our cooling fields. Assuming a single-row configuration, we can estimate the typical vortex spacing near the middle of our field range if we assume the vortex density to be described by $n(B) = (B - B_{th})/\Phi_0$ for B well beyond B_{th}, which is consistent with the measurements of Stan *et al.* [88]. For a cooling field of $2 B_{th}$ as an example, this corresponds to a vortex spacing of $4~\mu$m at $B = 86~\mu$T for the Re resonators.

If pinning disorder were negligible, such that a clear transition from the single- to double-row configurations were to occur, one would expect a kink in the $1/Q_v(B)$ data with a larger slope at the largest fields of our measurements and beyond. The ratio of the slope of $1/Q_v(B)$ above and below the kink should correspond to the ratio of $j(x)$ for $|x| = (w/2)/3 \approx 1.9~\mu$m (the vortex location in the two-row configuration) and $x = 0$ (the vortex location in the one-row configuration), or $J_s(1.9~\mu\text{m})^2/J_s(0)^2 = 1.15$. While such a kink (please refer to figure 6.4) is not so clear from our data, a denser series of measurements over a somewhat larger field range could potentially reveal this slope change, provided the random pinning was not too strong.

For magnetic fields just beyond the range that is plotted in Figure 6.12, we have a couple of points and one could argue that there is a subtle kink in $1/Q_v(B)$ followed
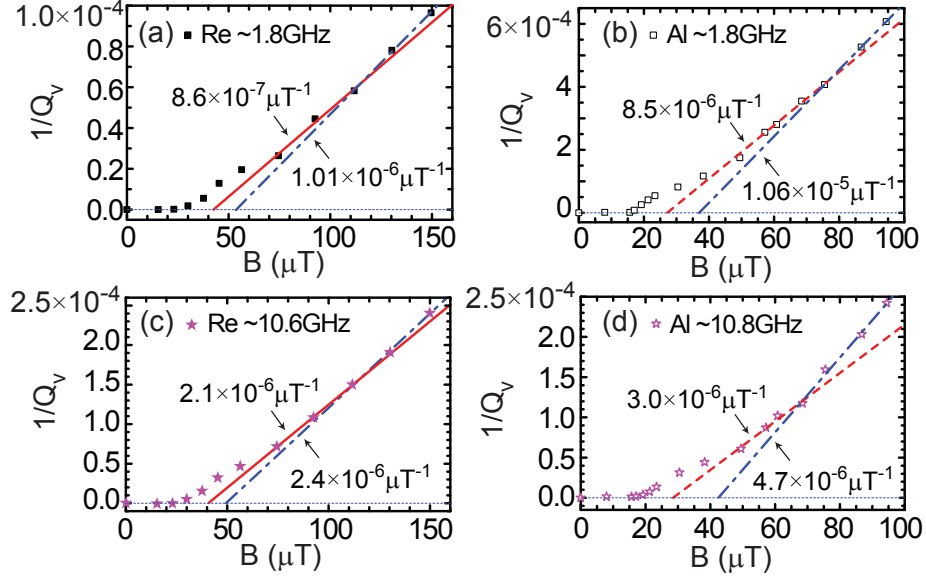
Figure 6.19: $1/Q_v(B)$ for $B \geq 0$ for lowest-frequency resonator for (a) Re and (b) Al; highest-frequency resonator for (c) Re and (d) Al. Red lines are fits below kink and are the same as the fits in Figure 6.12. Blue lines serve as a guide to the eye to suggest the possibility of a kink in the data.

by a linear increase with a larger slope. At higher fields, there are only a few points involved, so we put a straight line as a guide to the eye in Figure 6.19 to suggest the possibility of a kink in the data. Such kink is consistent with the probable spatial distribution of the vortices in our resonators and the non-uniform current distribution across the center conductor. Following simulations from Bronson *et al.* that was mentioned above, our measured values of B_{th} for the Re and Al films and the range of B from our measurements would correspond to just one or two rows of vortices along the centerline of our resonators. It is also quite plausible that random pinning in the film could wash out any kink due to a clear transition from one-row to two-row distributions

6.7   Conclusions

According to our analysis of the response of vortices in microwave resonators, we can rewrite Eq. (6.3) for $\tilde{\rho}_v$ as

$$\tilde{\rho}_v = j(x)\rho_n \frac{2\pi\xi_e^2}{a_0^2} \frac{\epsilon + if/f_d}{1 + if/f_d},$$ (6.25)

where $(B - B_{th})/\Phi_0 = 1/a_0^2$ with a_0 to be the approximate vortex spacing, and we have assumed $\eta_e = \eta$. In this form, one can see that the effective resistivity of the superconductor is related to the normal-state resistivity multiplied by the fractional area of the film that has a normal core from the vortices.

Based on our measurements we have compiled a table of the various parameters for our Re and Al films (Table 6.2). These values can be used to compute $\tilde{\rho}_v$, then combined with $j(0) = 0.35$ [Fig. 6.18(a)], assuming a single-row vortex configuration, and Eq. (6.11) to calculate $\partial\left(1/Q_v\right)/\partial B$. This results in a calculated slope that ranges between a factor of $0.6 - 1.0$ of the fit slopes in Fig. 6.12 for the different Re and Al resonators. A similar analysis for the $\partial\left(\delta f/f_0\right)/\partial B$ data, following the approach of Eqs. (6.9-6.11), yields a comparable level of agreement between our calculated and fit slopes. As described previously, disorder in the vortex positions caused by a random distribution of pinning sites could lead to deviations from the ideal single-row vortex configuration. Thus, this microwave vortex response model provides a satisfactory description of our measurements on Re and Al resonators. The same approach could be used to predict the microwave response of vortices in resonators patterned from other materials, although this would require some assumptions about the pinning strength in advance in order to estimate probable values for f_d and ϵ.

Despite the low vortex densities of our measurements, the response can be described reasonably in the context of an effective complex resistivity, which involves the pinning strength and vortex viscosity, along with a flux creep factor to account for the escape of vortices from pinning wells.

Material	T_c (K)	ρ_n ($\mu\Omega$ cm)	f_d (GHz)	ϵ	ξ_e (nm)	B_{th} (μT)
Re	1.70	1.6	22	0.003	50 — 100	43
Al	1.13	0.33	4	0.15	230	27

Table 6.2: Characteristic parameters for Re and Al thin films and vortices.

Chapter 7

Reducing microwave loss in superconducting resonators due to trapped vortices

A variety of factors determine the quality factor of superconducting microwave CPW resonators, including dielectric loss in the substrates and thin-film surfaces [68]. We have learned from chapter 6 that if the resonators are not cooled in a sufficiently small ambient magnetic field, or if large pulsed fields are present for operating circuits in the vicinity of the resonators, vortices can become trapped in the resonator traces, thus providing another loss channel. The presence of even a few vortices can substantially reduce the resonator quality factor [16].

In this chapter we demonstrate a technique for patterned pinning on the resonator surface to reduce the excess microwave loss due to trapped vortices. We compare field-cooled measurements for a series of coplanar waveguide (CPW) resonators patterned from the same thin film of Al, a common material used for qubits and MKIDs. Some of the resonators had a single longitudinal slot partially etched into the surface along the center conductor, while others had no slot. A surface step in a superconductor can pin a vortex because of the line energy variation associated with the change in
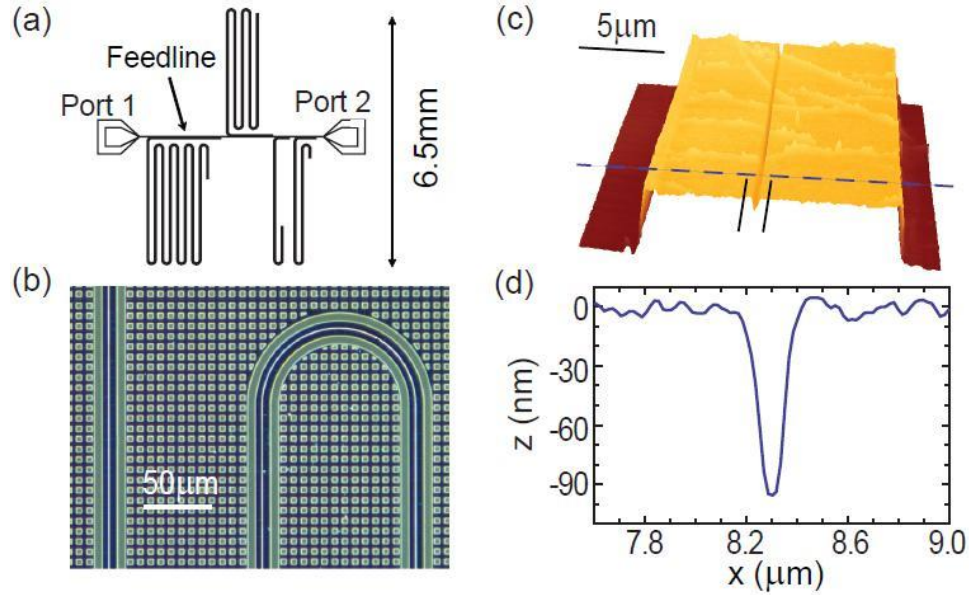
Figure 7.1: (a) Chip layout showing common feedline and four resonators. (b) Darkfield optical micrograph near shorted end of resonator. (c) Atomic Force Microscope (AFM) image showing configuration of slot on center conductor. (d) AFM line trace across slot.

thickness [107, 108]. Orienting the slot, with its surface steps on either side, along the length of the center conductor of a CPW resonator, aligns the pinning forces from the slot to oppose the Lorentz force due to the microwave current that flows in the resonator. Intuitively, one would expect such a slot to be most effective with a width comparable to the vortex core size, determined by the coherence length, which is of the order of a few hundred nm in these films [16].

7.1 Resonator design and fabrication

The layout of Al resonators on sapphire is identical to that in our previous work [16], with four quarter-wave CPW resonators of lengths corresponding to fundamental resonances near 1.8, 3.3, 6.9, and 11.0 GHz, as calculated with the Sonnet microwave circuit simulation software [72]. These resonators are coupled capacitively to a common CPW feedline, thus allowing for frequency multiplexing [Fig. 7.1(a)]

[4, 5], although we will focus on the resonators near 1.8 GHz in this work. We design for the resonators to be somewhat over-coupled at $B = 0$, where the intrinsic loss at the measurement temperature (310 mK) is dominated by thermal quasiparticles. This gives us the ability to continue to resolve the resonances with the anticipated enhanced levels of loss once vortices are introduced.

A 150 nm-thick Al film was electron-beam evaporated onto on a 2-inch sapphire wafer for patterning into multiple resonator chips with the layout of Fig. 7.1(a, b). On three of the dies, slots with a width of 200 nm, along with alignment marks, were patterned using electron-beam lithography and reactive ion etching (RIE) in a combination of BCl_3, Cl_2, and CH_4, with the etch timed to stop at a depth of 90 nm [Fig. 7.1(c, d)]. Three other dies had no slots written on them. Electron beam lithography writes patterns on a film, Al in our case, covered with ebeam resist by emitting a beam of electrons, then selectively develop away either exposed or non-exposed area of the resist, similarly to photolithography. Ebeam lithography creates very small structures in the film on the substrate; the one we use in CNF is JEOL 9300 with 20nm resolution. The resonators were then patterned photolithographically and aligned to the previously etched slot patterns, followed by a second RIE step that transferred the resonator pattern into the Al film. For the dies with slots, these follow the entire length of each resonator up to the feedline coupling elbow. A slight misalignment during the photolithography step caused all of the resonators to be shifted by 1.5 μm so that the slots are offset from the centerline of each resonator by this amount.

7.2 Measurements of vortex response with patterned pinning

We cool the resonators on a ^{3}He refrigerator and we measure the complex transmission S_{21} through the feedline using a a vector network analyzer (Agilent N5230A). The
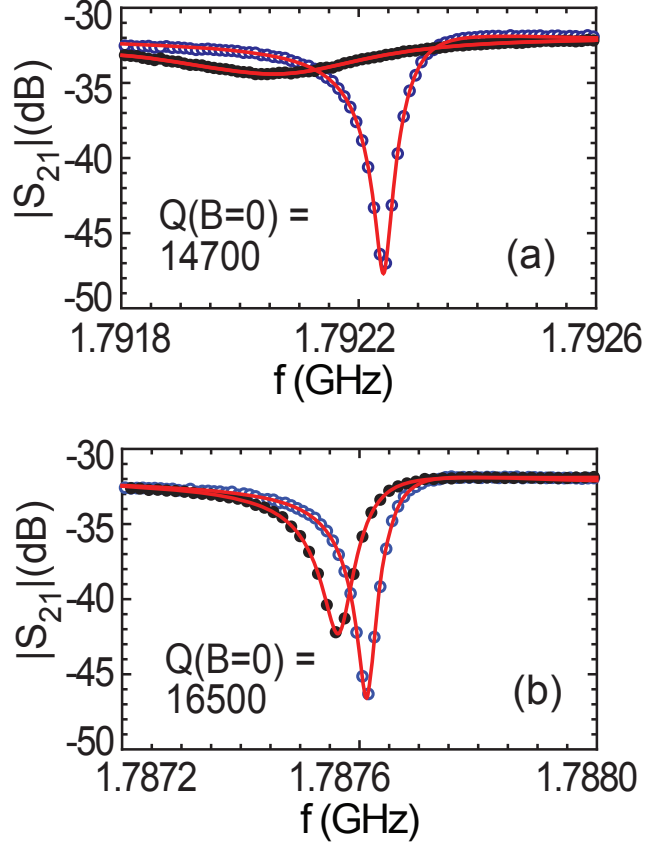
Figure 7.2: $|S_{21}|(f)$ at $B = 0$ (blue, open circles) and $B = 86$ μT (black, closed circles) for resonator with (a) no slot; (b) 200 nm-wide slot. Lines correspond to fits as described in text.

measurement procedure is essentially the same as in section 6.2.2 on Al resonatorshas. We employ a series of cold attenuators on the input side of the feedline and a cryogenic HEMT amplifier (gain ≈ 38 dB between $0.5 - 11$ GHz; $T_N \approx 5$ K) on the output side. A power of about -90 dBm delivered to the feedline keeps the resonators comfortably in the linear regime. We also use a superconducting Helmholtz coil to generate a magnetic field and a μ-metal cylinder attenuates stray fields in the laboratory. For each value of B, we heat the sample above T_c to 1.4 K, adjust the current through our Helmholtz coil to the desired value, then cool down to 310 ± 0.2 mK.

In general, the addition of vortices through field-cooling results in a downward shift in the resonance frequency and a reduction in the quality factor; the same

qualitative behavior as Al resonator in chapter 6. In Figure 7.2 we plot $|S_{21}|(f)$ for the resonators near 1.8 GHz, from a chip with no slot [Fig. 7.2(a)] and from a chip with a slot [Fig. 7.2(b)], where both resonators were measured at $B = 0$ and $B = 86\ \mu$T. The resonator with slot and the one without slot were patterned from the same film, and thus should have the same vortex viscosity and intrinsic pinning strength in the film. For $B = 0$, thus, with no vortices present, both resonators have comparable quality factors, determined primarily by the coupling to the feedline. However, the resonators behave quite differently when cooled in the same magnetic field. For the chip with no slot, this results in a substantial broadening and downward frequency shift. In contrast, the resonator with the slot has only a minimal reduction in its resonance linewidth and a small frequency shift.

7.3 Analysis of influence of nanostructured pinning

We can make a quantitative comparison between the resonators with and without slots by fitting the resonance trajectories in the complex plane to extract the quality factor Q and resonance frequency f_0 for each resonator at the various cooling fields. The fit process was the same as in Ref. [16] which followed a similar 10-parameter fitting procedure to what has been done for MKID measurements [5]. The same fitting process was dicussed in section 4.5 and used in chapter 6, We define the excess loss in each resonator due to the presence of vortices, $1/Q_v(B) = 1/Q(B) - 1/Q(B = 0)$, as in chapter 6, thus removing the loss due to thermal quasiparticles, coupling to the feedline, and any other field-independent loss mechanisms. In a similar manner, we compute the fractional frequency shift of each resonance, $\delta f/f_0(B) = [f_0(B = 0) - f_0(B)]/f_0(B = 0)$.

In Figure 7.3 we plot $1/Q_v(B)$ and $\delta f/f_0(B)$ for the resonators near 1.8 GHz with and without a slot. Error bars from the fitting process are included as chapter 6, but
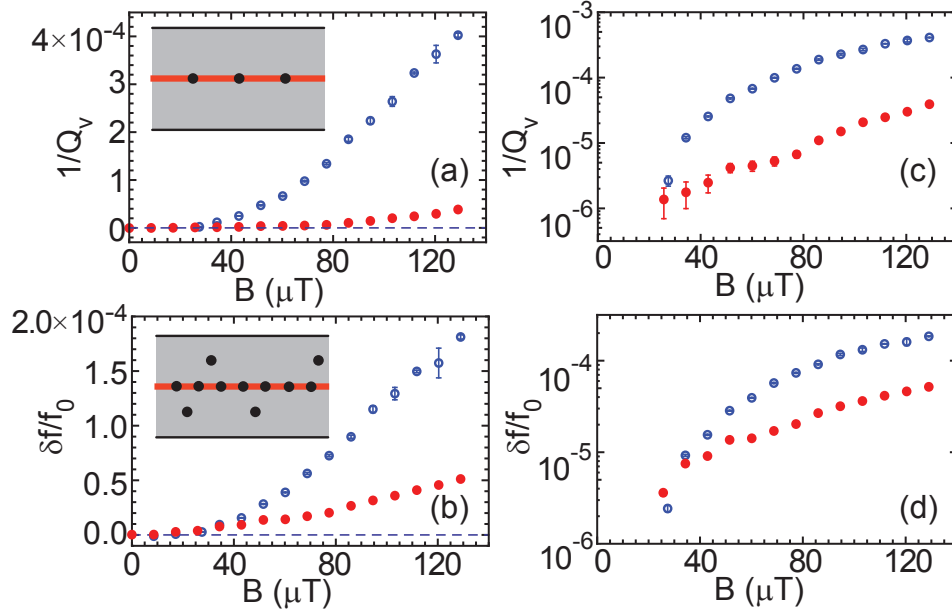
Figure 7.3: Comparison of resonators without (blue, open circles) and with a slot (red, closed circles): (a) $1/Q_v(B)$; (b) $\delta f/f_0(B)$. (c, d) Data from (a, b) plotted on a log scale. Insets show predicted vortex arrangements with a slot for small B (upper) and $B > 80\ \mu$T (lower).

in most cases are too small to be seen. Above a certain onset cooling field of $\sim$25 μT which is consistent with what we discussed in chapter 6, both $1/Q_v$ and $\delta f/f_0$ increase with B for both resonators, however, for the resonator with a slot, these quantities are much lower than in the resonator without a slot. Viewing the data on a logarithmic scale emphasizes the effect of the slot: a reduction in $1/Q_v$ by a factor between 10-20 over almost the entire measured field range relative to the resonator without a slot [Fig. 7.3(c)]. The slot also reduces $\delta f/f_0(B)$, although by a smaller factor [Fig. 7.3(d)].

We note that a comparison of the data in Figure 7.3 for the resonator with no slot with our earlier measurements in Al films from chapter 6 and Ref. [16] indicates a smaller $1/Q_v$ in the more recent resonators without slots by a factor of ~ 0.5. While both resonators had the same layout with a similar fabrication process, the Al film from chapter 6 and Ref. [16] had a RRR of 10, while the Al film in the resonators described in this chapter had a RRR of 19. This turns out to be the two extremes

of RRR that we have observed from a series of deposited Al films on sapphire in our evaporator. It appears that the resulting variation in the mean free path affects the loss contributed by a vortex. Nonetheless, we emphasize that all of the resonators presented in this chapter, both with and without slots, were fabricated simultaneously from a single Al film. Furthermore, in separate cooldowns we have measured two more chips from this wafer, one with a slot and one without, and obtained quite similar results to Figs. 2, 3. Thus, the differences in vortex response that we observe here are due solely to the presence of the slot in the resonator.

Vortex distributions in superconducting strips cooled in perpendicular magnetic fields have been studied theoretically [90–93] using energetic considerations of the interaction between the vortices and screening currents in the strip. According to vortex distributions which have been intensively discussed in the previous chapter, we expect the initial trapped vortices to be located near the centerline of the resonator for our resonators both with and without a slot. On the resonators with a slot, these initial vortices are almost certainly located in the slot [Fig. 7.3(a) inset], where the vortex line energy is reduced, despite the slight misalignment of the slot. At some threshold field, when the vortex density in the slot becomes too large, vortices will begin to get trapped outside of the slot [Fig. 7.3(b) inset], and thus contribute greater loss because of the weaker pinning there. In Fig. 7.3(c), we observe a kink in $1/Q_v$ near 80 μT for the resonator with a slot, above which the loss increases more rapidly. This kink, which would correspond to a vortex spacing of about 2 μm for a single row of vortices in the slot, may indicate such a threshold. Further reduction of $1/Q_v$ at larger B may be possible by patterning multiple parallel slots.

Although we have focused our comparison here on the resonators near 1.8 GHz, we have observed reductions in $1/Q_v$ between the higher frequency resonators with and without slots by factors of $\sim$8, 6, and 3 for the resonators near 3.3, 6.9, and 11.0 GHz, respectively. For a particular level of enhanced pinning, the loss will be larger as the frequency increases towards f_d. With no slot, $1/Q_v$ can actually decrease with
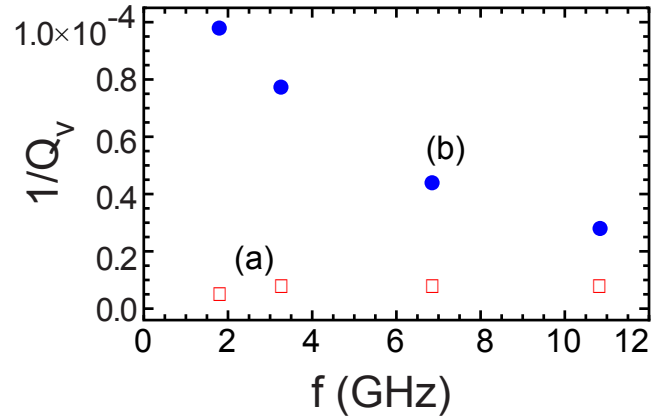
Figure 7.4: (Color online)$1/Q_v(B)$ vs. frequency for resonators with (Red, open square, labeled as a)and without a slot (Blue, closed circle, labeled as b) at a magnetic field 69 μT

frequency [16], such that the reduction of $1/Q_v$ for a resonator with a slot compared to one with no slot will be less substantial at higher frequencies. Figure 7.4 shows the $1/Q_v(B)$ vs. frequency for resonator with and without a slot at one of the magnetic fields 69 μT. From this figure, it can be seen that loss decrease with frequency for resonator without a slot, while loss slightly increases for resonator with a slot. This implies that the magnitude of the depinning frequencies for both films with and without a slot are quite different.

Chapter 6.4.2 has a detailed description for how to determine a depinning frequency, and the same proceture is taken to calcualte the depinning frequency for these two films with and without a lot. Figure 7.5 is the plot for r vs. magnetic field for 1.8GHz with and without a slot, here r is defined by 6.6 from chapter 6.4.2. The r for the film with a slot is way above unity, indicating the dominance of the reactive contribution of the vortex dynamics in the frequency range covered by four resonators on our chip. Meanwhile, the resonator without a slot has r being almost unity, and it means the significant loss related to the vortex motion in this resonators. For the same reason we mentioned in chapter 6.4.2, the data below the threshold field are not included. The other three resonators with center frequencies near 3.3, 6.9, and 11.0
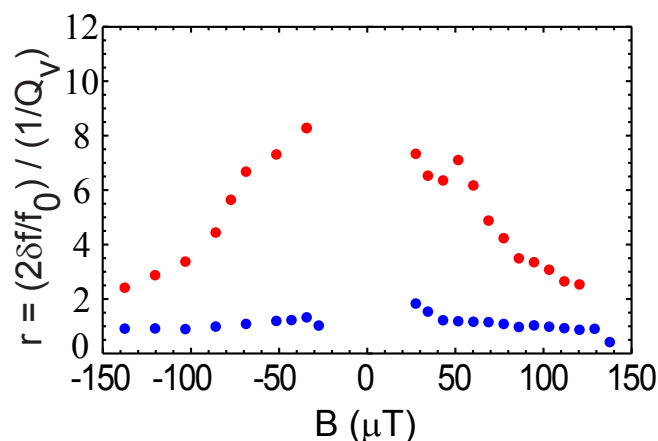
Figure 7.5: r vs. magnetic field for 1.8GHz with and without a slot
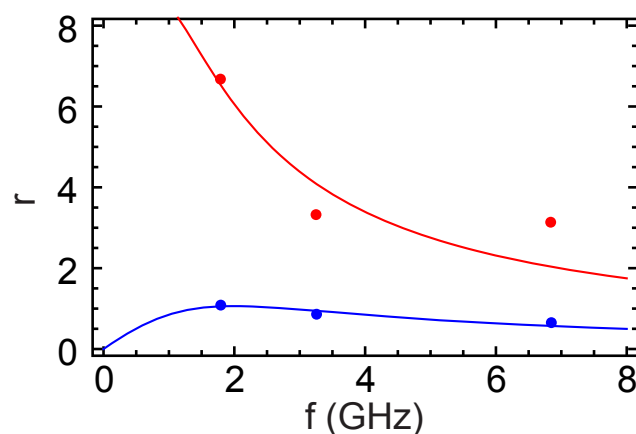
Figure 7.6: $r(f)$ for films with and without a slot with B=-69 μT along with fits as describe in text. Fit parameters are f_d=5 GHz (14GHz) and ϵ=0.16 (0.003) for films without a slot (films with a slot)

GHz have the similar magnitude of r as 1.8GHz resonator.

At a particular magnetic field, such as 69 μT, r vs. frequency can be plotted as Figure 7.6. For both films with and without slot, r decreases with frequency. The solid lines in the Figure are two-parameter fit to the $r(f)$ data with equation 6.6 by varying f_d and ϵ. f_d and ϵ for the film without slots are 5 GHz and 0.16, and with a slot they are 14 GHz and 0.003 respectively. Clearly there is a big difference for films

with and without a slot. The designed center frequencies are all below the f_d for film with a slot; this explains the loss is slightly increase with the frequency in Figure 7.4.

Based on our measurements here and in chapter 6 or Ref. [16], the presence of even a small number of vortices has a significant influence on the resonator quality factor. A single narrow slot along the centerline of an Al CPW resonator provides a straightforward method to increase the pinning and reduce the loss from vortices by over an order of magnitude. In general, purposely putting some nanostructure can control the microwave response of vortices due to the fact that those added nanostructure provides pinning sites for vortices. Then the loss in devices from trapped flux can be reduced. Meanwhile, some fundamental properties of vortices can be probed.

Chapter 8

Ongoing and future measurements

In the previous two chapters, we have studied the magnetic field and frequency dependence of the microwave response of a small density of vortices in resonators fabricated from thin films of Re and Al. We also learned that Al and Re resonators are influenced differently by vortices trapped in the resonator after the threshold cooling field is exceeded. Later we showed that resonators patterned with nanofabricated surface pinning structures exhibited over an order of magnitude reduction in the excess loss due to vortices compared with identical resonators from the same film with no fabricated surface pinning. All of these previous measurements were at relatively weak microwave drive power. We later explored the variation in the resonator behavior for different powers and found that the presence of vortices had a dramatic influence on the power-dependence of the loss and frequency shift of the resonator. Thus, the power dependence measurement could be a useful way to determine if a resonator contains trapped vortices.
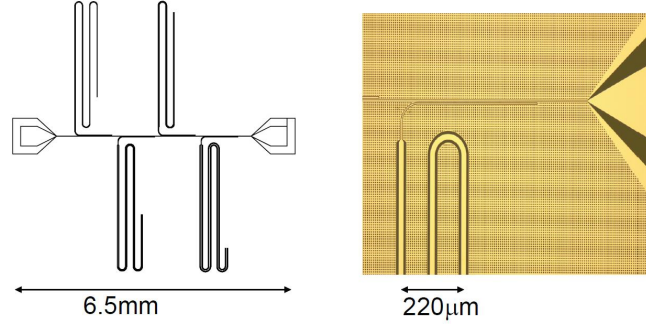
Figure 8.1: (a)The layout of four resonators with different width of 4, 8, 12 and 20 μm capacitively couple to one common feedline, (b) is the image of one 20 μm resonator from a microscope.

8.1 Power-dependence measurements of resonators for different magnetic fields

8.1.1 Resonator layout

In chapter 6.5, threshold cooling field for trapping vortices for different width resonators has been extensivly discussed. Threshold field B_{th} is proportional to Φ_0/w^2 [88]. A resonator layout with four different width of center conductor as Figure 8.1 shows is used. As usual, all the resonators are all capactively couple to one common feedline, the width of elbow parts is 4 μm, and there is 2 μm metal between feedline gap and elbow gap. A taper is used to switch the width of elbow part to the desired width of resonators. The detailed description of the layout can be found in chapter 6.5.4. All the designing parameters are listed in the Table 8.1, and the measured and calculated threshold field of this layout is listed in the Table 6.1.

8.1.2 Power dependence experiment and measurement results

The sample preparation for taking power dependence measurement was the same as the other measurements. The test chip was wire bonded into our standard PC Board,

Table 8.1: Table of designed parameters for the layout 8.1

Num of Resonator	Width(μm)	designed f_0(GHz)	designed Q_c
1	4	3.9485	17752
2	8	4.981	13730
3	12	4.28	15146
4	20	4.63	15726
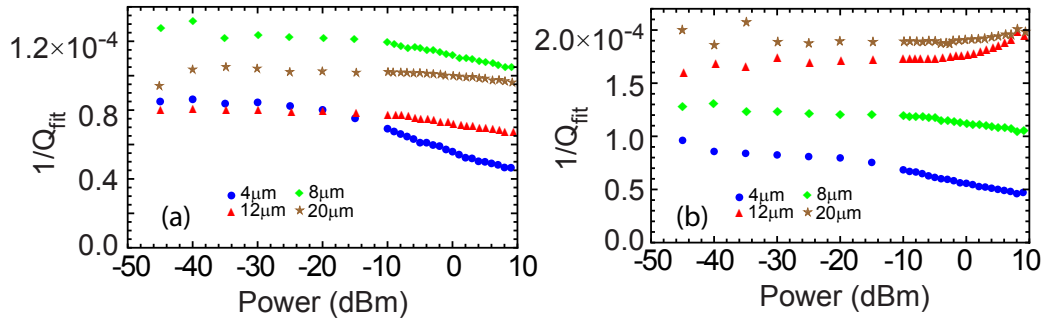
Figure 8.2: Q_{fit}^{-1} of four different width resonators as a function of power at 310mK for cooling in different magnetic fields: (a) 0; (b) 31 μT.

then mounted in the middle of the Helmholtz coil. The measurement configuration was similar to Figure 6.1(C) and described in chapter 6.5.4. Q_{fit} in terms of power for all four different width resonators were measured. Figure 8.2(a) shows Q_{fit}^{-1} of these four resonators as a function of the microwave drive power used to measure the transmission through the feedline at temperature 310 mK upon cooling in zero magnetic field.

There are two regimes in Figure 8.2(a) for the power dependence in zero field. At low microwave drive power, roughly below -20dBm (regime II), the loss is essentially independent of power. In the regime of above -20dBm (regime I), the loss then begins to decrease. This behavior while varying the power can be described in terms of the response of two-level system defects that reside in the surfaces of the resonator and will be discussed further in a subsequent section.

Figure 8.2(b) contains a plot of Q_{fit}^{-1} vs. power with the resonators cooled in a magnetic field of 31 μT. According to the Table 6.1 and Figure 6.14, for this particular cooling field, the 12 and 20 μm resonators will be beyond their threshold cooling fields, and thus will contain trapped vortices. In contrast, the 4 and 8 μm resonators should be below their threshold cooling fields and are therefore likely to be flux free. In the plot Fig. 8.2(b), not only is the overall loss higher for the 12 and 20 μm resonators, consistent with the presence of trapped vortices, but the loss now increases for larger microwave drive powers rather than decreasing in the case of flux-free resonators.

8.1.3 Microwave loss from surface oxides

In recent years, based on the substantial interest in the development of high-Q super-conducting microwave resonators, many groups have explored the role of microwave surface loss in determining the resonator quality factors [13, 15, 69, 73, 77]. Most su-perconducting films and many conventional substrates have native oxides that form on the surfaces. These oxides are generally amorphous and can contribute a substan-tial amount of loss at microwave frequencies due to the dynamics of defects in the oxide layers that can be well described as two-level systems. These same two-level systems were explored in great detail in the 1970s in the context of anomalous ther-mal and dielectric properties of glasses at low temperatures [109, 109, 110]. Much of the same physics from describing the low-temperature behavior of glasses can be ap-plied to explain the microwave loss from surface oxides in superconducting thin-film resonators [12, 69, 77].

In general there will be a broad distribution for the characteristic energies of these TLS defects in a particular amorphous material. In a resonant structure, there will be some fraction of the TLS with energies close to the characteristic energy of the resonator itself, and thus these can resonantly absorb energy from the resonator. According to Ref [73, 77], the loss contributed by surface two-level systems in a

superconducting resonator is:

$$\frac{1}{Q_{TLS}} = F\frac{1}{Q_{TLS}^0}\frac{\tanh(\frac{\hbar\omega}{2k_BT})}{\sqrt{1+(\frac{E}{E_s})^2}}$$ (8.1)

F is the filling factor of the TLS in the resonator structure [73] and E_s is the saturated eletric field. If the driving power is strong enough, the TLS near resonance become saturated, and and therefore, can no longer absorb energy from the resonator. Thus, the loss contributed by the TLS is reduced.

The electric-field dependence equation 8.1 assumes that the side walls of the center conductor provide a uniform electric field $\vec{E}$. For a coplanar waveguide geometry with a non-uniform field distribution, Wang *et. al.* derived an expression for the loss due to TLS in terms of signal power P, which can be expressed as:

$$\frac{1}{Q_{TLS}} = F\frac{1}{Q_{TLS}^0}\frac{\tanh(\frac{\hbar\omega}{2k_BT})}{\sqrt{1+(\frac{P}{P_0'})^{0.8}}}$$ (8.2)

with P_0' to be the saturated power in the unit of dBm.

The zero-field cooled power-dependence data from Fig. 8.2(a) can be fit with Eq. 8.2 by including an extra loss term $1/Q_0$ to account for other sources of loss that are independent of power, such as coupling loss and dissipation from quasiparticles. The term F from Eq. 8.2 is absorbed in term of $1/Q_{TLS}$ which makes it geometry dependent. The term P_0' accounts for the scaling between the input power at the top of the refrigerator and the resonator itself and incorporates the saturation signal power for the TLS in the resonator. The blue data points in Figure 8.3 are the measurements of the loss vs. power from Fig. 8.2(a) for a 4 μm resonator cooled in zero magnetic field. The red line is the fit according to Eq. 8.2 while varying F/Q_{TLS} and P_0' and adding a power-independent loss term $1/Q_0$. These fitting parameters for the four different resonator linewidths are listed in Table 8.2.
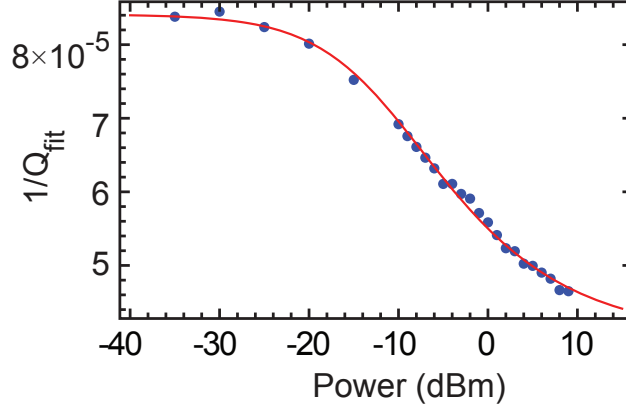
Figure 8.3: The blue data points in Figure 8.3 are the measurements of the loss vs. power from Fig. 8.2(a) for a 4 μm resonator cooled in zero magnetic field. The red line is the fit according to Eq. 8.2 while varying F/Q_{TLS} and P_0' and adding a power-independent loss term $1/Q_0$

Table 8.2: Table of fitting parameters for different width resonators

Width	Q_0	Q_{TLS}/F	P_0'
$4\mu m$	24881.6	22774.1	0.000076875
$8\mu m$	10283.4	40702.5	0.000387364
$12\mu m$	16154.7	57790.4	0.000382914
$20\mu m$	10770.5	100031	0.000568631

8.2 Power-dependence of loss with vortices present

In Fig. 8.4, the loss vs. power is plotted for the 12 μm resonator data from Fig. 8.2 for both zero-field cooling and cooling field of 31 μT. The zero-field cooled data, and thus with no vortices present, is well described by the TLS surface loss model. For the other data points, because the 31 μT cooling field is beyond the threshold field for the 12 μm resonator, vortices are present and they have a clear influence on the power dependence. Besides the overall increase in the loss, due to the physics of the vortex response described in the previous chapters, as the power is increased, rather than a decrease in the loss due to the saturation of the surface TLS as in the zero-field
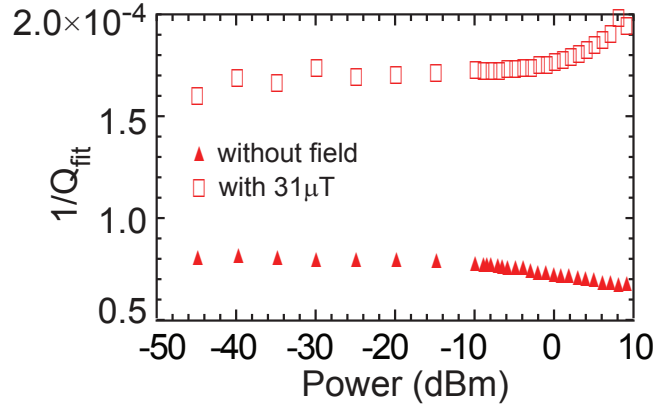
Figure 8.4: Loss versus power for 12 μm resonator with 0 and 31 μT magnetic fields.

cooled data, we observe an increase in the loss when vortices are present.

If the vortex response were linear with the drive strength, one would expect a power-independent loss from the vortices. However, as was first pointed out by Larkin and Ovchinnikov [111], the effective vortex viscosity can be a decreasing function of the vortex velocity. This arises because the electric field that is generated during the vortex motion can shift some of the bound quasiparticles out of the vortex core, thus reducing the viscosity. This can be described in terms of a critical velocity parameter v^* and zero-velocity viscosity $\eta(0)$ as:

$$\eta(v) = \frac{\eta(0)}{1 + \left(\frac{v}{v^*}\right)^2}. \tag{8.3}$$

This velocity dependence has been explored by many groups through low-frequency measurements of the flux-flow dynamics including Klein *et al.* who studied thin films of Al, In, and Sn. For our microwave resonators, larger drive powers correspond to higher vortex velocities. The resulting decreased viscosity expected due to Eq. 8.3 leads to an increase in the loss due to the vortex motion. We are currently working on a more complete theoretical model to incorporate the Larkin-Ovchinnikov velocity-dependent viscosity into our description for the vortex dynamics in the resonators to provide a quantitative fit to our power-dependence data with vortices present. The striking difference in the power-dependence of the loss with and without vortices

present suggests that this type of measurement could be used as a general technique to detect the presence of trapped flux in superconducting resonators.

8.3   Summary and Outlook

In this thesis, we have studied the magnetic field and frequency dependence of the microwave response of a small density of vortices in resonators fabricated from thin films of Re and Al. Despite the similarities of the superconducting thin films of Al and Re, the microwave behavior of trapped vortices was quite different between these two materials. We also learned that Al and Re resonators influent differently by the vortices trapped in resonator after their threshold field. We were able to describe the vortex dynamics in these two materials with a model incorporating the elastic response of the vortex pinning and the viscosity of the vortex cores. Later we showed that resonators with nanofabricated surface pinning structures exhibited over an order of magnitude reduction in the excess loss due to vortices compared with identical resonators from the same film with no patterned surface pinning. Currently, we are working to extend our model to incorporate a nonlinear flux-flow viscosity to account for the power dependence with vortices present. In future experiments with novel layouts, it may be possible to extend the work presented here to detect the presence of a single vortex in a microwave resonator.

Bibliography

[1] J. Clarke and F. K. Wilhelm, Nature **453**, 1031 (2008).

[2] A. Wallraff, D. Schuster, A. Blais, L. Frunzio, R. Huang, J. Majer, S. Kumar, S. Girvin, and R. Schoelkopf, Nature **431**, 162 (2004).

[3] M. Hofheinz, H. Wang, M. Ansmann, R. Bialczak, E. Lucero, M. Neeley, A. O'Connell, D. Sank, J. Wenner, J. Martinis, et al., Nature **459**, 546 (2009).

[4] J. Zmuidzinas, A. Vayonakis, P. K. Day, H. G. LeDuc, and B. A. Mazin, Nature **425**, 817 (2003).

[5] B. A. Mazin, Ph.D. thesis, Caltech (2004).

[6] T. Stevenson, F. Pellerano, C. Stahle, K. Aidala, and R. Schoelkopf, Appl. Phys. Lett. **80**, 3012 (2002).

[7] D. Schmidt, C. Yung, and A. Cleland, Appl. Phys. Lett. **83**, 1002 (2003).

[8] K. Irwin and K. Lehnert, Appl. Phys. Lett. **85**, 2107 (2004).

[9] M. Hofheinz, E. Weig, M. Ansmann, R. Bialczak, E. Lucero, M. Neeley, A. OConnell, H. Wang, J. Martinis, and A. Cleland, Nature **454**, 310 (2008).

[10] H. Wang, M. Hofheinz, M. Ansmann, R. Bialczak, E. Lucero, M. Neeley, A. OConnell, D. Sank, J. Wenner, A. Cleland, et al., Phys. Rev. Lett. **101**, 240401 (2008).

[11] J. M. Martinis, K. B. Cooper, R. McDermott, M. Steffen, M. Ansmann, K. D. Osborn, K. Cicak, S. Oh, D. P. Pappas, R. W. Simmonds, et al., Phys. Rev. Lett. **95**, 210503 (2005).

[12] J. Gao, M. Daal, A. Vayonakis, S. Kumar, J. Zmuidzinas, B. Sadoulet, B. A. Mazin, P. K. Day, and H. G. Leduc, Appl. Phys. Lett. **92**, 152505 (2008).

[13] R. Barends, H. L. Hortensius, T. Zijlstra, J. J. A. Baselmans, S. J. C. Yates, J. R. Gao, and T. M. Klapwijk, Appl. Phys. Lett. **92** (2008).

[14] J. Sage, V. Bolkhovsky, W. Oliver, B. Turek, and P. Welander, J. of Appl. Phys. **109**, 063915 (2011).

[15] J. Wenner, R. Barends, R. Bialczak, Y. Chen, J. Kelly, E. Lucero, M. Mariantoni, A. Megrant, P. OMalley, D. Sank, et al., Appl. Phys. Lett. **99**, 113513 (2011).

[16] C. Song, T. Heitmann, M. DeFeo, K. Yu, R. McDermott, M. Neeley, J. Martinis, and B. Plourde, Phys. Rev. B **79**, 174512 (2009).

[17] J. I. Gittleman and B. Rosenblum, Phys. Rev. Lett. **16**, 734 (1966).

[18] J. I. Gittleman and B. Rosenblum, J. Appl. Phys. **39**, 2617 (1968).

[19] G. E. Possin and K. W. Shepard, Phys. Rev. **171**, 458 (1968).

[20] N. Belk, D. E. Oates, D. A. Feld, G. Dresselhaus, and M. S. Dresselhaus, Phys. Rev. B **53**, 3459 (1996).

[21] S. Revenaz, D. E. Oates, D. Labbé-Lavigne, G. Dresselhaus, and M. S. Dresselhaus, Phys. Rev. B **50**, 1178 (1994).

[22] J. R. Powell, A. Porch, R. G. Humphreys, F. Wellhöfer, M. J. Lancaster, and C. E. Gough, Phys. Rev. B **57**, 5474 (1998).

[23] N. Pompeo and E. Silva, Phys. Rev. B **78**, 094503 (2008).

[24] A. G. Zaitsev, R. Schneider, R. Hott, T. Schwarz, and J. Geerk, Phys. Rev. B **75**, 212505 (2007).

[25] G. Ghigo, F. Laviano, L. Gozzelino, R. Gerbaldo, E. Mezzetti, E. Monticone, and C. Portesi, J. Appl. Phys. **102**, 113901 (2007).

[26] S. Sarti, C. Amabile, E. Silva, M. Giura, R. Fastampa, C. Ferdeghini, V. Ferrando, and C. Tarantini, Phys. Rev. B **72**, 24542 (2005).

[27] D. Janjušević, M. S. Grbić, M. Požek, A. Dulčić, D. Paar, B. Nebendahl, and T. Wagner, Phys. Rev. B **74**, 104501 (2006).

[28] H. McDaniel, Undergraduate thesis, UC Santa Barbara (2006).

[29] H. K. Onnes, Commun. Phys. Lab. Univ. Leiden **12** (1911).

[30] W. Meissner and R. Ochsenfeld, Naturwissenschaften **21**, 787788 (1933).

[31] F. H. L. London, Proc. Roy. Soc **A**, 866 (1935).

[32] V. L. Ginzburg and L. Landau, Zhurnal Eksperimental'noi i Teoreticheskoi Fiziki **20** (1950).

[33] L. N. C. J. Bardeen and J. R. Schrieffer, Phys. Rev. **108**, 11751205 (1957).

[34] M. Tinkham, *Introduction to Superconductivity* (McGraw-Hill, 1996).

[35] R. P. Huebener, *Magnetic Flux Structures in Superconductors* (Springer-Verlag, 1979).

[36] A. Abrikosov, Sov. Phys. JETP **5** (1957).

[37] M. Tinkham, Phys. Rev. **129**, 2413 (1963).

[38] A. L. Fetter and P. C. Hohenberg, Phys. Rev. **159**, 330 (1967).

[39] M. D. Maloney, F. de la Cruz, and M. Cardona, Phys. Rev. B **5**, 3558 (1972).

[40] G. J. Dolan, J. Low Temp. Phys. **15**, 133 (1974).

[41] G. Cody and R. Miller, Phys. Rev. **173**, 481 (1968).

[42] R. Miller and G. Cody, Phys. Rev. **173**, 494 (1968).

[43] G. Cody and R. Miller, Phys. Rev. B **5**, 1834 (1972).

[44] R. Parks and M. Tinkham, Phys. Today **23**, 66 (1970).

[45] P. H. Kes and C. C. Tsuei, Phys. Rev. B **28**, 5126 (1983).

[46] U. Essman and H. TrOuble, Phys. Lett. **24a**, 526 (1967).

[47] J. Bardeen and M. J. Stephen, Phys. Rev. **140**, A1197 (1965).

[48] Y. Kim, C. Hempstead, and A. Strnad, Phys Rev **139**, 1163 (1965).

[49] M. J. Stephen and J. Bardeen, Phys. Rev. Lett. **14**, 112 (1965).

[50] P. Anderson, Phys. Rev. Lett. **9**, 309 (1962).

[51] P. Anderson and Y. Kim, Rev. of Modern Phys. **36** (1964).

[52] Y. Yeshurun, A. Malozemoff, F. Holtzberg, and T. Dinger, Phys Rev. B **38**, 11828 (1988).

[53] R. Labusch, Phys. Stat. Sol **41**, 659 (1969).

[54] E. Kramer, J. of Appl. Phys. **44**, 1360 (1973).

[55] M. Fisher, Phys. Rev. Lett. **62**, 1415 (1989).

[56] B. Dam, J. Huijbregtse, F. Klaassen, R. Van der Geest, G. Doornbos, J. Rector, A. Testa, S. Freisem, J. Martinez, B. Stäauble-Pümpin, et al., Nature **399**, 439 (1999).

[57] M. W. Coffey and J. R. Clem, Phys. Rev. Lett. **67**, 386 (1991).

[58] E. H. Brandt, Phys. Rev. Lett. **67**, 2219 (1991).

[59] H. Suhl, Phys. Rev. Lett. **14**, 226 (1965).

[60] S. B. Cohn, IEEE Trans. **MTT**, 768 (1969).

[61] C. Wen, Microwave Theory and Tech., IEEE Trans. on **17**, 1087 (1969).

[62] D. Pozar, *Microwave engineering* (John Wiley & Sons, 2007).

[63] R. Simons and J. Wiley, *Coplanar waveguide circuits, components, and systems* (John Wiley & Sons, Inc., 2001).

[64] A. Vayonakis and J. Zmuidzinas (2001), unpublished.

[65] D. Mattis and J. Bardeen, Phys. Rev. **111**, 412 (1958).

[66] A. Wallraff, D. Schuster, A. Blais, L. Frunzio, J. Majer, M. Devoret, S. Girvin, and R. Schoelkopf, Phys. Rev. Lett. **95**, 60501 (2005).

[67] J. Schreier, A. Houck, J. Koch, D. Schuster, B. Johnson, J. Chow, J. Gambetta, J. Majer, L. Frunzio, M. Devoret, et al., Phys. Rev. B **77**, 180502 (2008).

[68] A. OConnell, M. Ansmann, R. Bialczak, M. Hofheinz, N. Katz, E. Lucero, C. McKenney, M. Neeley, H. Wang, E. Weig, et al., Appl. Phys. Lett. **92**, 112903 (2008).

[69] H. Wang, M. Hofheinz, J. Wenner, M. Ansmann, R. Bialczak, M. Lenander, E. Lucero, M. Neeley, A. OConnell, D. Sank, et al., Appl. Phys. Lett. **95**, 233508 (2009).

[70] A. Von Hippel, *Dielectric materials and applications: papers by twenty-two contributors* (published jointly by the Tech. Press of MIT and Wiley, 1954).

[71] A. Shnirman, G. Schön, I. Martin, and Y. Makhlin, Phys. Rev. Lett. **94**, 127002 (2005).

[72] SONNET, (Sonnet Software, Inc., Liverpool, NY, 2005).

[73] D. Pappas, M. Vissers, D. Wisbey, J. Kline, and J. Gao, IEEE Trans. on Appl. Supercon. **21**, 871 (2011).

[74] K. Mimura, Y. Ishikawa, M. Isshiki, and M. Kato, Materials Trans. **38**, 714 (1997).

[75] R. Chambers, Proc. of the Royal Soc. of London. Series A **215**, 481 (1952).

[76] L. P. G. A. A. Abrikosov and Khalatnikov, Sov. Phys. JETP **35** (1959).

[77] J. Gao, Ph.D. thesis, Caltech (2008).

[78] R. Glover III and M. Tinkham, Phys. Rev. **108**, 243 (1957).

[79] J. Gao, J. Zmuidzinas, A. Vayonakis, P. Day, B. Mazin, and H. Leduc, J. of Low Temp. Phys. **151**, 557 (2008).

[80] R. Meservey and D. Douglass, Phys. Rev. **135**, A24 (1964).

[81] M. Goppl, A. Fragner, M. Baur, R. Bianchetti, S. Filipp, J. Fink, P. Leek, G. Puebla, L. Steffen, and A. Wallraff, J. of Appl. Phys. **104**, 113904 (2008).

[82] T. Van Duzer and C. Turner, *Principles of superconductive devices and circuits* (1981).

[83] W. Chang, J. of Appl. Phys. **50**, 8129 (1979).

[84] R. Meservey and P. Tedrow, J. of Appl. Phys. **40**, 2028 (1969).

[85] K. Watanabe, K. Yoshida, T. Aoki, and S. Kohjiro, Jpn. J. Appl. Phys. **33**, 5708 (1994).

[86] K. Inomata, T. Yamamoto, M. Watanabe, K. Matsuba, and J. Tsai, J. of Vacuum Sci. & Tech. B **27**, 2286 (2009).

[87] K. Watanabe, K. Yoshida, T. Aoki, and S. Kohjiro, Jpn. J. Appi. Phys. **33**, 5708 (1994).

[88] G. Stan, S. B. Field, and J. M. Martinis, Phys. Rev. Lett. **92**, 97003 (2004).

[89] K. H. Kuit, J. R. Kirtley, W. van der Veur, C. G. Molenaar, F. J. G. Roesthuis, A. G. P. Troeman, J. R. Clem, H. Hilgenkamp, H. Rogalla, and J. Flokstra, Phys. Rev. B **77**, 134504 (2008).

[90] E. Bronson, M. P. Gelfand, and S. B. Field, Phys. Rev. B **73**, 144501 (2006).

[91] J. R. Clem, Bull. Am. Phys. Soc. **43**, 401 (1998).

[92] G. M. Maksimova, Phys. Solid State **40**, 1607 (1998).

[93] K. K. Likharev, Sov. Radiophys. **14**, 722 (1971).

[94] B. Abdo, E. Segev, O. Shtempluck, and E. Buks, J. Appl. Phys. **101**, 083909 (2007).

[95] M. A. Golosovsky, H. J. Snortland, and M. R. Beasley, Phys. Rev. B **51**, 6462 (1995).

[96] C. C. Chin, D. E. Oates, G. Dresselhaus, and M. S. Dresselhaus, Phys. Rev. B **45**, 4788 (1992).

[97] G. Blatter, M. V. Feigel'man, V. B. Geshkenbein, A. I. Larkin, and V. M. Vinokur, Rev. Mod. Phys. **66**, 1125 (1994).

[98] A. G. Zaitsev, R. Schneider, G. Linker, F. Ratzel, R. Smithey, and J. Geerk, Phys. Rev. B **68**, 104502 (2003).

[99] M. Hein, *High-Temperature-Superconductor Thin Films at Microwave Frequencies* (Springer, 1999).

[100] J. Romijn, T. M. Klapwijk, M. J. Renne, and J. E. Mooij, Phys. Rev. B **26**, 3648 (1982).

[101] P. H. Kes and C. C. Tsuei, Phys. Rev. B **28**, 5126 (1983).

[102] W. L. McMillan, Phys. Rev. **167**, 331 (1968).

[103] A. Ul Haq and O. Meyer, Thin Solid Films **94**, 119 (1982).

[104] N. A. Tulina, Solid State Comm. **41**, 313 (1982).

[105] J. R. Clem, unpublished.

[106] D. Sheen, S. Ali, D. Oates, R. Withers, and J. Kong, Appl. Supercon., IEEE Trans. **1**, 108 (1991).

[107] O. Daldini, P. Martinoli, J. Olsen, and G. Berner, Phys. Rev. Lett. **32**, 218 (1974).

[108] B. Plourde, D. Van Harlingen, N. Saha, R. Besseling, M. Hesselberth, and P. Kes, Phys. Rev. B **66**, 054529 (2002).

[109] W. Phillips, Rep. on Prog. in Phys. **50**, 1657 (1987).

[110] P. Anderson, B. Halperin, and C. Varma, Philosophical Magazine **25**, 1 (1972).

[111] A. Larkin and Y. Ovchinnikov, Zh. Eksp. Teor. Fiz **68**, 1915 (1975).

VITA

NAME OF AUTHOR: Chunhua Song

PLACE OF BIRTH: Qidong, Jiangsu, China

DATE OF BIRTH: January, 30, 1977

GRADUATE AND UNDERGRADUATE SCHOOLS ATTENDED:

Syracuse University, Syracuse, New York

Nanjing University, Nanjing, China

DEGREES AWARDED:

Syracuse University

Master in Physics, 2004

Nanjing University

Bachelor in Material Science and Engineering, 1999

Nanjing University

PROFESSIONAL EXPERIENCE:

Research Assistant, Syracuse University, 2011

Teaching Assistant, Syracuse University, 2005

Physics Teacher, Suzhou No.3 High School, 2001